OULUN YLIOPISTO
UNIVERSITY of OULU

OULU MINING SCHOOL

FACULTY OF TECHNOLOGY

Semyon Martynenko

HIGH-RESOLUTION SHORT-WAVE INFRARED HYPERSPECTRAL CHARACTERIZATION OF ALTERATION AT THE SADIOLA HILL GOLD DEPOSIT, MALI, WESTERN AFRICA

MASTER'S THESIS

JUNE 2019

UNIVERSITY OF OULU
Oulu Mining School

Unit
Oulu Mining School (OMS)

Author	Supervisors
Semyon Martynenko	Prof. Pekka Tuisku; Dr. Frank J.A. van Ruitenbeek; Prof. Kim A.A. Hein

Title
High-resolution short-wave infrared hyperspectral characterization of alteration at the Sadiola Hill gold deposit, Mali, Western Africa

Subject	Type of the degree	Time of publication	Number of pages
Economic Geology	Master of Science	20.06.2019	95+8

Abstract

Sadiola Hill is an ~8 Moz gold deposit located in western Mali within a ca. 2200-2050 Ma tectonic window known as Kédougou-Kénieba inlier (KKI), exposing the Western African craton. The deposit is hosted in a metasedimentary package made up of impure carbonate rocks, wackes, and arenites intruded by three distinct igneous phases. A N-S-trending Sadiola shear zone, related to the regional Senegalo-Malian shear zone, and NNE-trending third order fault splays acted as conduits for auriferous hydrothermal fluid flow (Hein and Tshibubudze 2007; Cameron 2010; Masurel et al. 2017). This study determined that gold is associated with ferroan dolomite/dolomite+/-ankerite- muscovite to Al-poor muscovite- phlogopite, cogenetic with sulphide precipitation. The intensity of white mica replacement of biotite, and abundance of Fe-bearing carbonates in association with phlogopite, are good predictors of gold mineralization. Within well-mineralized samples phlogopite occurs as gangue silicate that recrystallized after sulphidation reactions took place. Geochemical data agree with the hyperspectral interpretation of ore-stage alteration assemblages, as K/Al molar, Mg/Al molar, and total C enrichment positively correlated with increasing gold grade.

Differences in spectral expression of carbonate alteration in the greywacke, diorite, and impure marble were well-constrained during this study. Syn-mineralization carbonate is dolomite in the impure marble unit and attains ferroan dolomite-ankerite composition in the greywacke and diorite. The differences in the Fe content between the ore-stage carbonates expressed in different rock types can be explained by progressive rock-buffering with the surrounding Fe-rich minerals within the diorite and greywacke. As the impure carbonate unit is Mg-rich, the ore-stage dolomite consistently shows low Fe-content. Furthermore, Fe in biotite was preferentially consumed by sulphidation reactions, leaving no residual iron for the dolomite.

Muscovite and Al-poor muscovite occur in all host rocks and are associated with gold grade in the impure carbonate and the greywacke. Investigation of protolith control revealed that white mica is consistently more aluminous and attains higher crystallinity values in tonalite, while cogenetic white mica within the greywacke is Al-poor illite. These variational differences are attributed to availability of Al^{3+} and lower Mg^{2+} content in the tonalite to produce muscovite. Phengite (Al-OH at ~2225nm) occurs in the system as a minor post-mineral alteration phase. Finally, Illite crystallinity has a common trend of increasing veinward, which was attributed to lower degree of fluid-rock interaction in the vein centre and higher fluid/rock ratio.

Keywords
Geology, short-wave infrared, SWIR, hyperspectral Imaging, reflectance spectroscopy, decision tree classification, geochemistry, gold, white mica, illite, muscovite, carbonate, ferroan dolomite, ankerite, tourmaline, phlogopite; epidote, west African craton, Senegalo-Malian Shear zone, Sadiola Hill; illite crystallinity; ferrous drop

Additional information
Not applicable

Table of Contents

1   INTRODUCTION

Sadiola Hill gold deposit is a shear-hosted system located in western Mali within ca. 2200-2050 Ma tectonic window known as Kédougou-Kéniéba Inlier (KKI) (Masurel et al, 2017). The deposit is a collaborative partnership between AngloGold Ashanti Ltd. (41%), IAMGOLD Corp. (41%), and government of Mali (18%). Combined proven and probable reserves of December 31, 2017 are 69.35 Mt of ore @ 1.86 g/t Au, amounting for a total of 4142 koz of gold (https://miningdataonline.com).

Current research investigated alteration assemblages at Sadiola Hill with short-wave infrared (SWIR) hyperspectral imaging and conventional petrography. This study established paragenetic sequence of six distinct hydrothermal events within the system. Spatial variation in the chemical composition of alteration minerals, and protolith control on alteration expression were also assessed. The research was carried out on drill core samples from 6 diamond holes capturing the most representative alteration examples and was solely laboratory based. The core samples were scanned at medium (0.2mm pixel size) and high-resolution (26μm pixel size).

Hyperspectral images were classified with decision trees, a set of scripts matching spectral responses of scanned sample surfaces to spectra from USGS spectral library. Position of absorption features and specific calculated parameters, e.g. illite crystallinity, were utilized for the mineral classification. As part of the classification, abundances of spectrally active minerals were calculated based on pixel count within each sample.

Paragenetic context of alteration mineralogy was determined with conventional transmitted light microscopy. Spectral classes of the 26μm-pixel mineral maps were validated with the petrographic observations. Additionally, stoichiometry of white mica, carbonates, biotite, chlorite, and amphibole were determined with electron microprobe analyses to link mineral chemistry to spectral responses.

Finally, geochemical sampling of the Sadiola Hill drill core was conducted to define trace and pathfinder element associated with gold, and to characterize significant host rocks occurring within the Sadiola goldfield. The data were also used to further evaluate systematic changes in hydrothermal alteration proximal and distal to the ore zone.

1.1   Problem Description

Despite several studies undertaken within the last two decades, there was no comprehensive description of alteration variation at a mineral-scale at Sadiola Hill, and current paragenetic model of alteration requires some refining. The footprint of alteration and its cooling trend were also not well-defined. Prior to this study, the alteration assemblages at Sadiola Hill were not analysed with modern SWIR hyperspectral scanning. Given the lack of hyperspectral characterization of alteration mineralogy, a lot of subtle mineralogical variations, that otherwise could indicate changes in pH, fluid chemical parameters, and temperature, likely have been overlooked. Furthermore, protolith control on alteration was not well-understood. Finally, a set of more rigid constraints was required to define the alteration in space and time.

1.2   Research Questions

The main objective of the current study is to characterize the hydrothermal alteration and its footprint throughout the deposit focusing on the number of hydrothermal events and their relation to the ore minerals. Specifically, the following questions are going to be addressed:

- How many hydrothermal events acted in the system and what is their relative timing?
- What alteration assemblages are associated with gold mineralization?
- Is there a spatial variation in the chemical composition of alteration minerals present?
- What is the extent of hydrothermal footprint of the ore system?
- How alteration assemblages change depending on protolith's mineralogical composition?
- Are primary textures recognizable in hydrothermally altered rock?

1.3   Research Approach

The research was carried out at the Faculty of Geo-Information Science and Earth Observation (ITC), University of Twente, Netherlands and Oulu Mining School

(OMS), University of Oulu from September 2018 to May 2019. SWIR hyperspectral imaging was acquired from 79 drill core samples (Figure 1) at 0.2mm pixel-resolution and 34 drill core samples at high-resolution (26µm). Collected hyperspectral data was analysed in conjunction with available drill logs, assays, as well as petrographic observations of thin sections corresponding to the high-resolution scans, allowing for one-to-one comparison. Rock composition as well as pathfinder and trace elements distribution were determined by geochemical analyses. Additionally, electron microprobe studies were undertaken to further validate spectral classification by linking spectral responses to chemical composition of white mica, carbonates, biotite, chlorite, and amphibole.
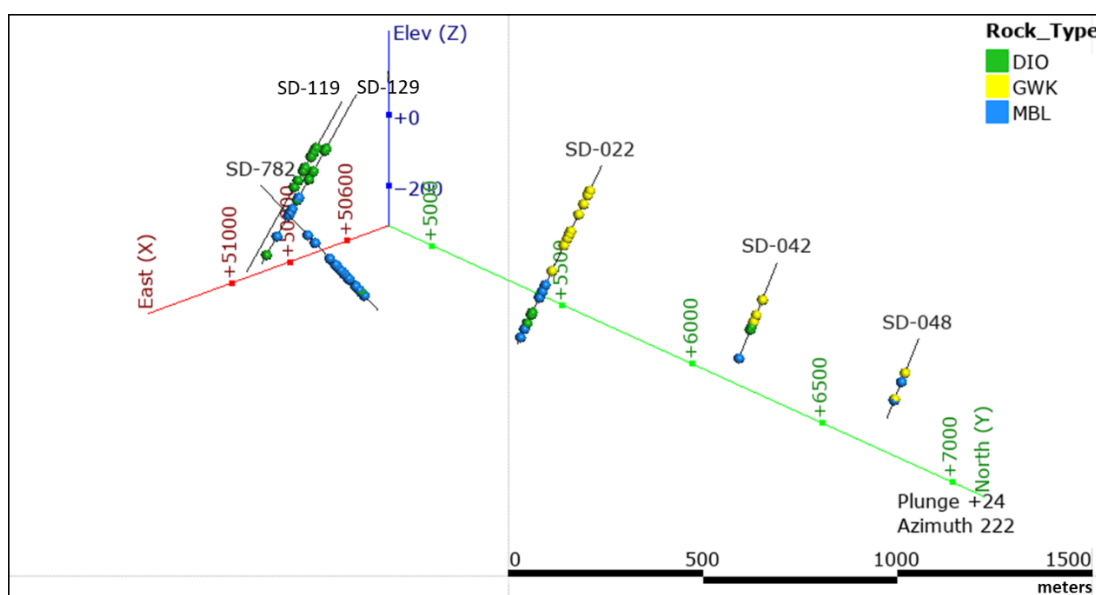
Figure 1. Distribution of representative samples investigated as part of this study within six diamond drill holes at Sadiola Hill. Abbreviations: DIO = diorite; GWK = greywacke; MBL = marble. Figure generated in Leapfrog 3D Geo software.

2   BACKGROUND

2.1   Gold Deposits in Granite-Greenstone Terranes

Gold deposits in metamorphosed granite-greenstone terranes form at various stages of orogenic evolution. The genesis of some of these deposits is rather controversial due to interpretation complications resulting from remobilization and overprinting (Groves et al., 2003). Nonetheless, the orogenic gold deposit class emerged in the late 1990s as an attempt to unify various deposits that often had geographic names attached to them (e.g. Homestake-, Motherlode-type), since it was recognized that these deposits share similarities despite their Precambrian to Phanerozoic age (Groves et al., 1998; Goldfarb et al., 2001, 2005). These similarities include: 1) timing of deposit formation is generally late to post-peak metamorphism, 2) location is restricted to fore-arc and back-arc settings 3) alteration assemblages are indicative of a thermal equilibrium with the country rocks, 4) gold deposition is accompanied by addition of K, S, CO_2, H_2O, and Si, with possible associations with As, B, Bi, Na, Sb, Te, and W. 5) H_2O-CO_2-CH_4-N_2-H_2S auriferous fluids are of low-to-moderate salinity, 6) base-metal contents are low consistent with low fluid salinity values (Goldfarb and Groves, 2015).

Gold concentration in the Earth's crust is estimated at about 1-4 ppb with minor differences between rock types, while enrichment reaches 10,000 times in world-class deposits (Phillips and Powell, 2010). To attain such high enrichment, a series of outstanding processes are required to effectively scavenge gold and transport it to deposition site without loss. Considering this, understanding controls on gold solubility in hydrothermal fluid and its trapping mechanisms are key factors to the accurate interpretation of a gold system genesis. HS^- is an important ligand dictating solubility of gold in orogenic systems, with gold transported as $Au(HS)_2^-$ complexes (Williams-Jones et al., 2009). The significance of the HS^- ligand increases at higher temperatures. In these cases $AuHS^0$ is the predominant compound at acidic to intermediate pH values, with maximum stability at 350^0C, while $Au(HS)_2^-$ occurs at higher pH values and is most stable at 250^0C. At higher temperatures coupled with decreasing dielectric constant of water, Au favours stable bonds with Cl^- and OH^- anions. Destabilization of the bisulphide complexes is promoted by decreases in HS^-

and fO_2 activity and increasing pH, according to Le Châtellier's principle (Williams-Jones et al., 2009).

Destabilization can occur in response to boiling, sulphidation, oxidation, cooling, depressurization, or a combination of these processes. Boiling decreases HS^- activity via fractionation of H_2S into a vapor phase. Boiling also facilitates an increase in pH since acidic components escape into the vapor phase. Additional outcomes of boiling include decrease in temperature coupled with adiabatic expansion of the liquid and increase in fO_2. Sulphidation of Fe-bearing minerals reduces HS^- activity as sulphur is trapped forming iron sulphides, commonly pyrite, but pyrrhotite and arsenopyrite may also occur. At maximum solubility of gold, near the intersection of stabilities of H_2S, HS^-, SO_4^{2-} a small increase in fO_2 will lead to a drastic drop in HS^- resulting in gold precipitation (Williams-Jones et al, 2009).

Orogenic gold deposits can be hosted in various rock types with Archean examples dominated by volcanic sequences and Phanerozoic deposits mostly associated with formation of meta-sedimentary basins. These differences in host rocks are attributed to evolution of the Earth's crust, its thermal state, and tectonic regimes throughout geologic time (Goldfarb and Groves, 2015). Phillips and Powell (2010) pointed out that rock type, e.g. intrusive, extrusive, or clastic is less important than the rock's bulk chemical composition. Host rock composition dictates its ability to provide a source of iron for sulphidation reactions. In this case rocks with high initial ratios of Fe/(Fe+Mg), such as BIF and mafic rocks, make favourable hosts (Goldfarb et al., 2005). Ubiquitous reduced carbon will destabilize gold-thiosulphide complexes; hence black shales make favourable host rocks for gold deposition. Rheological properties of a host-rock have to be accounted for as relative tensile strength and pore fluid pressure will affect vein propagation (Phillips and Powell, 2010).

Orogenic mineralization may occur at various depths and can be subdivided into ductile, brittle-ductile, and brittle regimes that correspond to hypozonal, mesozonal, and epizonal levels. The common feature of deposits at various levels is that they usually form late in the orogenic setting and relate to changes in regional stress resulting in transition from compressional to transpressional or transtensional regimes (Goldfarb and Groves, 2015).

Based on fluid inclusions studies and investigation of alteration assemblages, auriferous fluid has low salinity values and is enriched in H_2O-CO_2-H_2S. Phillips and Powell (2010) suggested that the fluid's redox state is maintained at near-constant levels distal and proximal to ore. Alteration assemblages associated with gold include muscovite, biotite, carbonates, and sulphides resulting from enrichment in K, Rb, S, C, CO_2, and H_2O (Phillips and Powell, 2010), and enrichment in Ag, As, Bi, Sb, Te (Goldfarb and Groves, 2015). Goldfarb et al. (2005) also report enrichment in Na, Sr, Li, Cs, Tl, and Ba. In contrast, Ridley (2013) argues that there is no Ag enrichment in orogenic gold systems and Ag does not exceed background crustal abundances. Ferroan dolomite and ankerite are common ore-stage carbonate alteration minerals in the host-rocks with Fe/Fe+Mg molar > 0.5. In rocks with an initial Fe/Fe+Mg molar < 0.5, Fe is consumed by siderite-magnesite series carbonates and, as a result, Fe-sulphides are uncommon (Goldfarb et al., 2005).

The metamorphic devolatilization model for fluid sources (Phillips and Powell, 2010) is the most accepted model for the origin of fluids in orogenic systems, although a relationship to local magmatism has been a recurring issue because orogenic gold camps worldwide are spatially related to multiple generations of felsic to intermediate intrusions. However, the relationship to gold mineralization based on cross-cutting relationships reveals that intrusions may occur pre- or post-ore, and typically reflect an overall tectonic regime favourable for igneous activity (Goldfarb et al., 2005; Goldfarb and Groves, 2015). The metamorphic devolatilization model proposes that H_2O and CO_2 are released during transition from greenschist to amphibolite facies during dehydration reactions. Gold is extracted from the host-rock and bonds to ligands in solution, with HS^- being the most common ligand at the metamorphic redox and P-T conditions. The CO_2 component of the fluid assures its buffering capacities that maintain the auriferous fluid's redox and pH level relatively constant during hydrothermal transport to trap site (Phillips and Powell, 2010). Fluid movement at shallow crustal levels is facilitated by strain that drastically increases permeability. At this stage fluid movement/migration occurs as a repetitive combination of fracture growth and crack sealing events (Cox, 2005). Phillips and Powell (2010) suggested that at depths exceeding the brittle-ductile transition with zero porosity, fluid ascent occurs as porosity waves. Fluid movement/migration to gold deposition sites occurs along deeply seated faults and shear zones. The channelized nature of transport along

these structures minimizes gold loss prior to reaching a sink site. Gold precipitation occurs in second and third order structures and zones of structural and rheological complexities where fluid-rock interaction is increased and chemical changes to auriferous fluid are promoted (Phillips and Powell, 2010).

2.2   Regional Geology

The West African Craton (WAC) is a well-endowed region hosting a variety of metal commodities. Nearly 200 gold deposits in the WAC occur in metamorphosed volcano-sedimentary packages of Archean and Paleoproterozoic ages, with latter formed during the Eburnean Orogeny (2.5-1.8 Ga). Orogenic gold is the most common deposit type within the WAC, however rare IOCG and skarn deposits also occur in the craton. Gold is hosted in a wide range of rock types including granitoids, mafic rocks, both volcanic and plutonic, sedimentary rocks, carbonates, and BIF. Shear zone orogenic gold is hosted by quartz veins and mostly restricted to greenschist facies metamorphosed terrains with rare instances of lower amphibolite facies regional metamorphism. Disseminated gold-sulphide associations, typically gold-pyrite and gold-arsenopyrite are also common. Gold in shear zones is structurally-controlled and is often occurs at a contact between Birimian metasedimentary and metavolcanic packages. Hydrothermal alteration associated with gold is protolith-controlled and expressed as carbonate-pyrite-chlorite-sericite in metasedimentary packages, actinolite-chlorite-quartz+/-chalcopyrite+/-albite+/-leucoxene in mafic metavolcanic rocks, and quartz-chlorite-sericite-epidote in granitoids (Markwitz et al., 2015; Markwitz et al., 2016).

The West African craton exposed in the Kédougou-Kéniéba Inlier (KKI) is a unique Paleoproterozoic granite-greenstone belt as it contains a package of carbonate rocks of variable thickness uncommon for other granite-greenstone terranes worldwide. The KKI is comprised of several volcano-plutonic belts of the Birimian age, and related sedimentary basins, that formed during a series of accretionary events (Markwitz et al., 2016). The inlier is bound by the Hercynian Mauritanide orogeny on the western flank, and by the Neoproterozoic Taoudenni intracratonic basin. Therefore, the KKI represents the westernmost exposure of the ca. 2200-2050- Ma Birimian Supergroup in the WAC (Villeneuve, 2008; Lawrence et al, 2013).

The Main Transcurrent Zone (MTZ) separates the Mako Series and the Dialé-Daléma Series basement rocks (Figure 2). Tholeiitic basalts and calc-alkaline andesite are interbedded with sedimentary and volcaniclastic rocks and make up the Mako Series. Whole rock Sm-Nd dates obtained from volcanic units range from 2160 +/- 16 Ma for andesite and 2197 +/- 13 Ma for basalt. The Mako Series were intruded by Tinkoto granodiorite at 2074 +/- 9 Ma and by Mamakono granodiorite at 2076 +/- 3 Ma. Geochemical evidence suggests that the Mako Series and granodioritic plutons formed in a volcanic arc setting (Masurel et al., 2017).

The Dialé-Daléma Series are comprised of volcaniclastic sequences, as well as sedimentary sequences composed of arenites, wackes, siltstones, argillites and carbonates. Volcaniclastic and sedimentary rocks of the Dialé-Daléma Series are interbedded with minor lavas and pyroclastites of intermediate to felsic composition. Detrital zircon ages collected from siliciclastic unit within the series, yield ages between 2096 +/- 8 and 2165 +/- 1 Ma, constraining the oldest possible age for deposition (Milési et al., 1989; Hirdes and Davis, 2002). Additional age constraint of 2079 +/- 2 Ma comes from U-Pb zircon collected from the Saraya quartz monzodiorite that intruded the Dialé-Daléma Series (Hirdes and Davis, 2002). Thus Dialé-Daléma basin rocks and the Mako Series are likely to be of a similar age.

The Falémé Series, a calc-alkaline volcano-plutonic belt, is located immediately west of the Senegalo-Malian Shear Zone (SMSZ). Lithologic units comprising the Falémé Series include volcaniclastic rocks of calc-alkaline affinity, carbonate-rich sedimentary rocks, wackes, chert, shale, and minor lava flows of andesitic to rhyolitic composition (Lawrence et al., 2013; Masurel et al., 2017). Scarce geochronological data indicates late Birimian age of Falémé Series formation. U-Pb ages of 2080 +/- 1 Ma and 2082 +/- 1 Ma were attained from Boboti granodiorite and South Falémé pluton (Hirdes and Davis, 2002).

The Kofi Series is the easternmost part of the KKI separated from the Dialé-Daléma Series, and from Falémé Series in the south by SMSZ. The Kofi Series consists of sequences of impure carbonates, wackes, arenites, siltstones, and calcareous clastic rocks. Pb-Pb and U-Pb dating of detrital zircons of Kofi Series sediments from Loulo area indicated ages of 2156 +/- 10 Ma and 2093 +/- 7 Ma respectively (Masurel et al., 2017). The Kofi sediments have been intruded by several generations of igneous rocks consistent with emplacement of I-type calc-alkaline intrusives associated with ca.

2115-2050 Ma Eburnean orogeny (Hein et al., 2015). The Dialé-Daléma and Kofi Series contain the most significant exposures of impure carbonates within the KKI. Both, the Dialé-Daléma and Kofi Series have been interpreted as syn-deformational foreland basin packages (Masurel et al., 2016).

Structural history of the KKI records evidence of four progressive deformation events: thrusting during D_1-D_2 in response to crustal thickening, and D_3-D_4 associated with oblique convergence. The D_1 event is poorly understood due to substantial overprint by the later deformation events. The 2115-2050 Ma Eburnean orogeny is interpreted to correspond with the D_2 and D_3 events. Formation of sinistral transpressional SMSZ occurred during D_2 and in response to NW-SE shortening. D_3 is the main syn-mineralization event during which auriferous hydrothermal fluids ascended along the SMSZ. Dextral reactivation of the early structures occurred during the latest D_4 event. Evidence of the D_4 is not prevalent across the KKI and has only been recorded in some deposits along the SMSZ (Masurel et al., 2017).
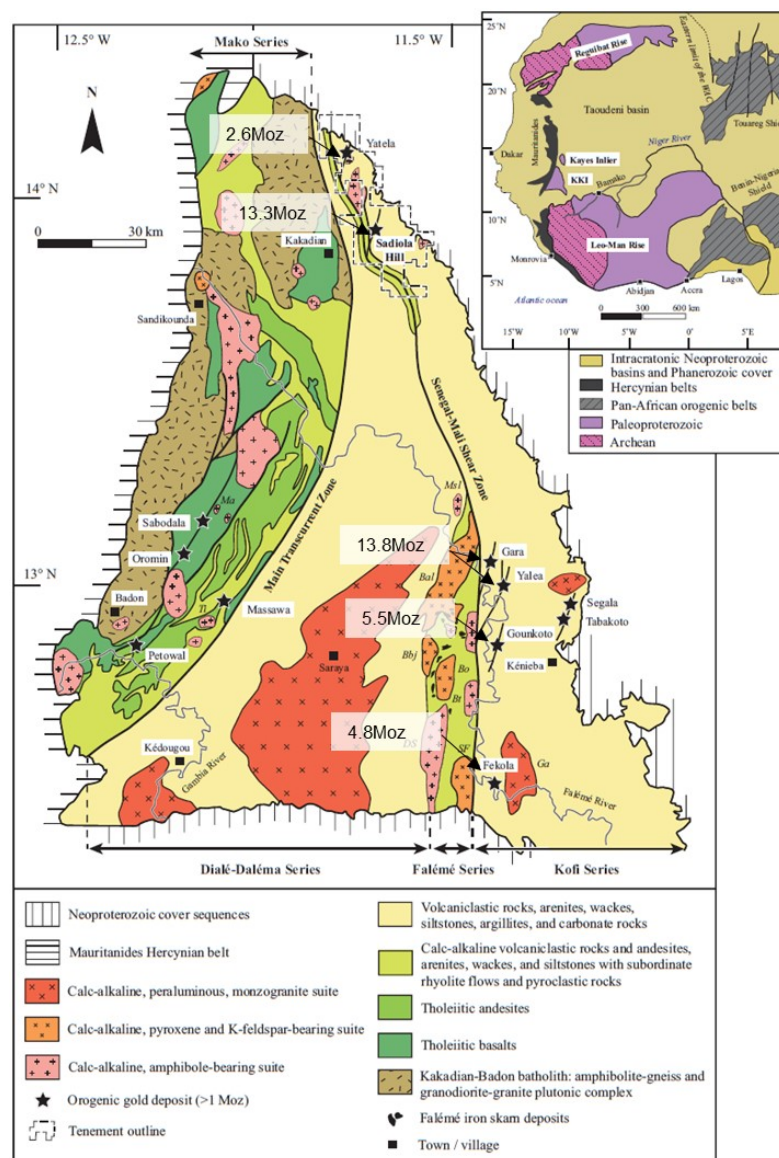
Figure 2. 1:250,000 scale geologic map of the Kédougou-Kéniéba Inlier (KKI) and major gold deposits along Senegalo-Malian shear zone. Inset map shows geologic setting of the West African craton. Contained gold amount shown as total resources since discovery in millions of ounces, (*data sourced from www.avesoro.com*). Abbreviations for plutons: Bal = Balangouma tonalite, Bbj = Bambadji granodiorite, Bo = Boboti granodiorite, Bt = Boto granodiorite, DS = Dar Salam granodiorite, Ga = Gamaye granite, Ma = Mamakono granodiorite, Msl = Moussala granodiorite, SF = South Falémé granodiorite, Ti = Tinkoto granodiorite (*modified after Masurel et al., 2017)*.

Several gold deposits have formed during the D$_3$ event and are genetically linked to the crustal-scale SMSZ, including the world-class Sadiola goldfield and Loulo mining district (Figure 1). The Yatela goldfield consists of in-situ sub-economic gold mineralization hosted in calcitic and dolomitic marbles and meta-sedimentary rocks of the Birimian Supergroup, overlain by enriched saprolite residual (Hein et al., 2015).

The Sadiola Hill deposit is hosted in impure limestone, and to lesser extent a greywacke, with ore geometry controlled by Sadiola Fracture Zone and related NNE-trending fault splays. Polyphase hydrothermal alteration assemblages include calc-silicate phase actinolite-tremolite, followed by syn-mineral potassic assemblages of biotite-carbonate-K-feldspar. Gold mineralization at Sadiola Hill is accompanied by As and Sb (Hein et al., 2015; Masurel et al., 2017).

The Loulo mining district consists of two significant deposits - Gara and Yalea, both hosted in calcareous greywackes and calcitic-dolomitic marbles, as well as the Gounkoto deposit. Mineralization at Gara occurs as stratabound disseminated sulphides or gold-bearing ankerite-rich stockwork veins. Pre-, syn-, and post-ore pervasive albite and tourmaline alteration is specific to Gara-type deposits in the mining camp. The Yalea deposit is associated with quartz +/- ankerite lodes and sulphide stringer zones. In contrast to Gara, Yalea alteration assemblages lack tourmaline and consist of chlorite-sericite-carbonate +/- albite. Mineralization at Gounkoto is structurally-controlled and hosted in shear-zones parallel to the SMSZ, and associated sinistral NNW-trending dilational jogs. Alteration assemblages at Gounkoto are similar to those of Gara with poly-phase albite-tourmaline and iron-rich ore stage minerals (Lawrence et al., 2013).

Fekola is the southern-most deposit in the KKI along the Senegalo-Malian Shear Zone. The deposit is hosted by metasedimentary rocks of the Kofi Series that are locally represented by argillites and pelites, fine-grained turbidites, as well as polymictic conglomerates. Fine-grained impure limestone occurs only as a minor lithologic unit. Gold mineralization at Fekola is associated with in-situ pyrite stringers concordant to foliations. Alteration assemblages consist of dolomite-albite with minor quartz component (Garagan et al., 2015).

2.3   Deposit Geology

2.3.1   Stratigraphy and Lithologic Units

The Sadiola goldfield is hosted in metasedimentary rocks of the Kofi Series (Figure 3). The Kofi Series of the goldfield include impure carbonate rocks, greywacke, shale, and arenites that grade to siltstones and argillites toward the east

(Hein and Tshibubudze, 2007; Masurel et al., 2017). The rocks of the Sadiola goldfield have undergone regional mid-greenschist facies metamorphism and a polyphase brittle-ductile deformation history (Hein and Tshibubudze, 2007).

The greywacke grades upwards into finer clasts/matrix material and may have all parts of Bouma sequence present. Slump folding occurs in the greywacke-siltstone units at all scales (Hein and Tshibubudze, 2007). The siltstone is a volumetrically minor unit occurring as fine to massive beds of several millimetres to over a meter in thickness. Shale units at Sadiola are interbedded with greywacke and siltstones, or comprise a subdivision of Bouma sequences in graded greywacke or siltstone. Graphite-rich and Fe-rich varieties of the shale units have also been reported at Sadiola (Hein and Tshibubudze, 2007).

The greywacke is underlain by a package of impure carbonate of dolomitic-calcitic composition. The stratigraphic contact between the two units is marked by a N-S-trending Sadiola shear zone with the impure carbonate occurring in the footwall to the east (Hein and Tshibubudze, 2007; Cameron, 2010). The impure carbonate records ductile shearing ranging from strongly foliated marly schist and fault gouge, carbonate breccia, to transposed bedded carbonate and folded carbonate (Cameron, 2010).

Sedimentary structures documented within the Sadiola goldfield indicate dominance of deltaic and turbiditic syn-depositional processes. Depositional environment of the sediments was thus interpreted as the margin of an ocean basin in a delta slope to prodeltaic environment of a river-dominant delta system (Hein and Tshibubudze, 2007). Additionally, based on a few preserved way-up indicators, the metasedimentary packages stratigraphically face to the west (Masurel et al., 2017).

The impure carbonate and the greywacke have been intruded by three distinct generations of intrusions: early diorite, quartz feldspar porphyry, and late diorite. The earliest generation of intrusions include diorite stocks, discontinuous dykes, and sills that have been generally emplaced concordant to the contact between carbonate and sandstone units. Garnet-pyroxene exoskarn assemblages are common and form a 2-5 m metasomatic zone along the contact of the diorite with the carbonate unit. The NNE-trending quartz-feldspar porphyry dykes and stocks represent the second generation of intrusions. The dykes crosscut the first generation of dioritic intrusions, as well as the

carbonate and detrital sedimentary units. Quartz-feldspar porphyries are spatially associated with the NNE-trending shear zones and often form approximately 1.5 m-wide silicification zones caused by syn-emplacement hydraulic fracturing. The final stage of igneous intrusions consists of NNE- to NE-trending 2 m-wide diorite dykes (Masurel et al., 2017).
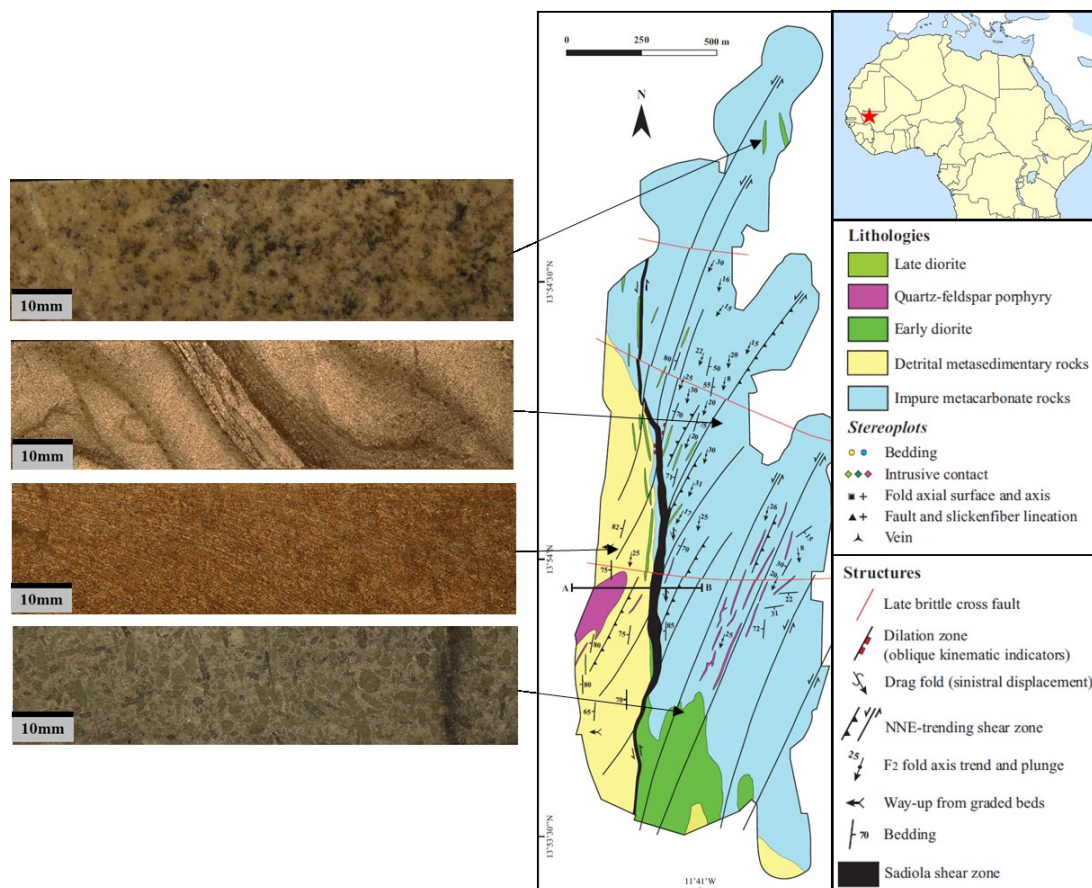
Figure 3. Geological map of the Sadiola Hill main pit and drill core photographs of the main host rocks. Inset map shows the deposit location in the West Africa (*modified after Masurel et al., 2017*).

2.3.2 Structural Framework

Sadiola Hill deposit records a complex brittle-ductile history evident from 3 distinct pre- and syn-mineralization deformation events, as well as two smaller scale brittle events postdating gold deposition (Masurel et al., 2017). The main structural features of the Sadiola Hill deposit include the N-S-trending subvertical to vertical Sadiola fracture zone (SFZ), also referred to Sadiola shear zone, and associated NNE-trending fault splays. The SFZ marks the major structural break at Sadiola separating

hanging wall greywackes on the western side of the pit from the footwall marbles on the eastern side (Hein and Tshibubudze, 2007; Cameron, 2010). The SFZ has been interpreted as a second order structure related to the regional Senegalo-Malian shear zone based on a regional magnetic low signature. It has been interpreted that the SFZ and the NNE-trending fault splays acted as conduits for auriferous hydrothermal fluid flow largely controlling existing geometry of the ore body (Hein and Tshibubudze, 2007; Cameron, 2010; Masurel et al., 2017). The high-grade ore shoots at Sadiola Hill correspond to intersections of the SFZ and the NNE-trending faults resulting in their southerly plunging orientation. A wider zone of high-grade mineralization is also associated with an anticlockwise flexure in the strike of the SFZ (Cameron, 2010).

2.3.3 Hydrothermal Alteration

Calc-silicate or skarn alteration (diopside, actinolite, chlorite, epidote, dravitic tourmaline, scapolite, vesuvianite, and fluorite) corresponds to a release of metasomatic hydrothermal fluids during contact metamorphism associated with emplacement of diorite intrusions (Hein and Tshibubudze, 2007). Masurel et al. (2017) constrained calc-silicate alteration to actinolite-tremolite assemblages. This assemblage is suggested to be the earliest in the deposit and is associated with emplacement of Eburnean intrusive suite at 2060-2040 Ma pre-dating gold mineralization.

Previous studies suggest that potassic alteration occurs as biotite, calcite-dolomite, and quartz with minor component of tourmaline, muscovite, and K-feldspar (Hein and Tshibubudze, 2007; Masurel et al., 2017). The potassic assemblages are focused along the SFZ and the NNE-trending second order structures related to the SFZ. Biotite forms an alteration halo around the deposit and in places defines F_2 foliation fabric (Cameron, 2010). Tourmaline preferentially occurs in impure carbonates parallel to the shear fabric and in halos of quartz-calcite-biotite veins. Overall the potassic alteration assemblages were interpreted as syn-mineralization based on textural association with sulphides and gold as well as spatial associating with economic gold grade (Masurel et al., 2017).

Calcite-dolomite occurs as veins, clots, and bands preferentially in the hanging wall greywacke. Calcite intensifies to strong pervasive flooding approaching the

Sadiola shear zone. Masurel et al. (2017) suggest that both pervasive and vein-controlled assemblages are syn-genetic to gold mineralization. Chlorite-calcite alteration is related to post-mineral normal offset and reactivation of existing structures. It is manifested as vein-controlled chlorite-calcite hosting non-auriferous pyrite (Hein and Tshibubudze, 2007). Weathering and laterite development processes resulted in alunite-jarosite assemblages formed in response to an onset of deep weathering of primary alteration minerals and sulphides. Decomposition of plagioclase resulted in abundant smectite within the developed saprolite zone (Hein and Tshibubudze, 2007).

2.3.4   Mineralization

Previous studies indicated that sulphides and gold at Sadiola occur in two stages (Masurel et al, 2017). The As-rich stage I precipitated arsenopyrite-pyrrhotite+/-pyrite, and native gold with minor component of scheelite, chalcopyrite, and molybdenite. The Au-Sb-dominant stage II is characterized by antimony, sulfosalts, and pyrrhotite-berthierite-tetrahedrite-stibnite-native gold and aurostibite assemblages. Overall, the two stages account for 20% and 80% of gold endowment at Sadiola deposit respectively (Masurel et al., 2017).

2.4   Hyperspectral Methods for Mineral Identification

Short-wave infrared spectroscopy is an application of vibrational infrared absorption spectroscopy, a technique based on the interaction of electromagnetic radiation with the vibration state of molecules (functional groups with covalent bonding) in matter, compounds and crystalline solids. The absorption is related to specific functional group and their orientation in the matter as well as electronic environment in ordered substances (Rossman, 1988). Short-wave infrared (SWIR) hyperspectral imaging has become a reliable technique for identification of hydrothermal alteration minerals such as phyllosilicates and carbonates, accurately defining footprints of hydrothermal alteration and tracing fluid pathways (van Ruitenbeek et al., 2005; Wang et al., 2017; Lampinen et al., 2018). Hyperspectral imaging is a non-destructive diagnostic technique that utilizes interaction of electromagnetic light in the SWIR range and surface minerals comprising a rock.

Spectrally active minerals absorb electromagnetic energy at specific wavelength intervals producing diagnostic mineral-specific absorption features (Hunt, 1977) Diagnostic absorption features are an outcome of array of a mineral's chemical composition, its crystal structure, and molecular bonds. To be precise, the absorption bands derive from vibrational overtones, electronic transitions, charge transfer, and conduction (Clark et al., 1990). Majority of minerals characteristic of hydrothermal alteration in orogenic gold systems, namely carbonates, white mica, and chlorite (Groves et al., 2003), contain atomic bonds and functional groups detectable within SWIR range of 1000nm-2500nm of the electromagnetic spectrum.

White mica (i.e. muscovite, paragonite and phengite) and Al-bearing clayss, are characterized by absorption features positioned at 2200nm related to Al-OH bond, and 1900nm absorption feature corresponding to H-OH bond (Figure 4, A). White mica is a particularly important alteration mineral in hyperspectral classification as it is sensitive to pH, temperature, and chemical changes of hydrothermal fluid (Duke, 1994; Dalm et al, 2017). Tschermak substitution of Al^{3+} by Fe^{2+} and Mg^{2+} in muscovite crystal structure shifts position of Al-OH bond at ~2200nm to longer wavelengths. This change occurs in response to increase in pH as acidity of hydrothermal fluids decreases away from its source. Substitution of Na^+ for K^+ results in formation of paragonite (Deer et al., 1992), and is often indicative of Na-rich protolith influence. Illite crystallinity is an important parameter for classification of white mica and clays. Illite crystallinity is a ratio of the depth of Al-OH absorption at 2200nm to a sum of depth of OH and H-OH absorption at 1900nm (Agus, 2011). Sharpness of Al-OH feature is deeper and more pronounced in highly crystalline white mica in comparison to illites where Al-OH feature is shallower, but water absorption feature is more pronounced. Increasing illite crystallinity indicates higher temperatures at which white mica crystallized. Therefore, illite crystallinity combined with shifts of Al-OH feature are utilized as vectoring tools in hydrothermal systems (Harraden et al, 2013).
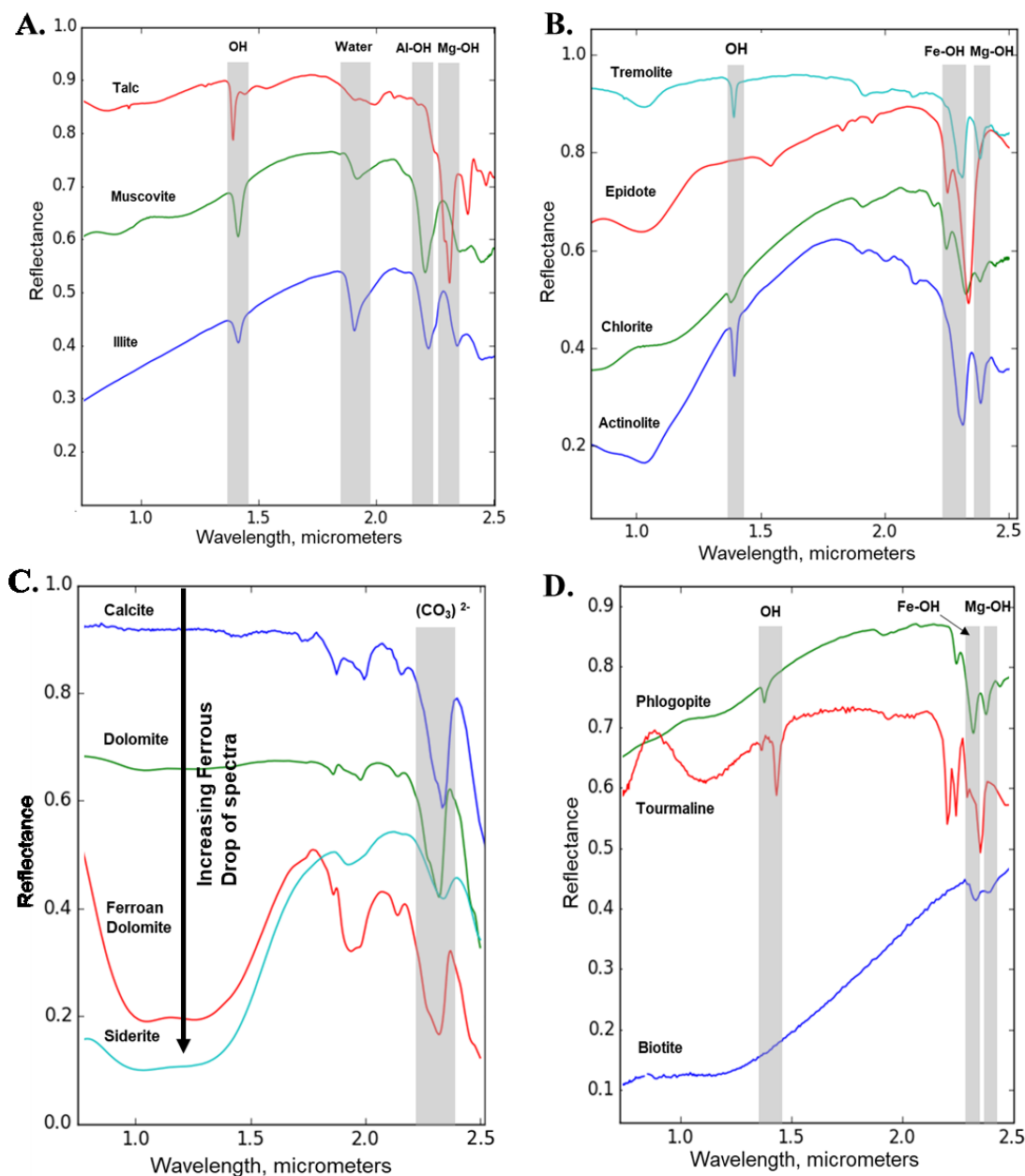
Figure 4. Spectral responses of key alteration and metamorphic minerals of an orogenic setting. **A.** Muscovite, illite, and talc. Note differences in depth of water features in illite vs. muscovite and presence of diagnostic Mg-OH feature in talc. **B.** Actinolite series calcic amphiboles, Mg-chlorite, and epidote. Note epidote absorption feature at ~1550nm and absence of this feature in chlorite, as well as position and depth of Fe-OH absorption feature influenced by Fe-content in mineral's crystal structure. Actinolite spectrum steepening in 1300-1600nm range resulting from Fe^{2+} substitution. **C.** Calcite group minerals showing overlap of the CO_3^{2-} feature and increasing ferrous drop of spectra moving towards siderite. **D.** Depth of Fe-OH and Mg-OH features in phlogopite vs. biotite; tourmaline showing pronounced "W-shaped" diagnostic feature. The figure created in hyperspectral python software with the following spectra from USGS spectral library version 7: actinolite_HS116.3B; biotite_HS28.3B; calcite_CO2004_BECKb; chlorite_HS1179.2B; dolomite_HS102.3B_ASDNGb; dolomite_ML97-3_ferroan; epidote_GDS26.b_it75um; illite_GDS4.2; muscovite_HS146.1B; phlogopite_HS23.1B; siderite_HS271.3b; talc_HS21.1B; tourmaline_HS282.2B; tremolite_HS18.1B (after Kokaly et al. 2017).

Carbonate group minerals are identified by absorption band between 2300 and 2360nm caused by CO_3^{2-} group (Figure 4, C). With position of the carbonate absorption feature centered between ~2335-2345nm in calcite, ~2320-2328nm in dolomite, ~2330-2340 in ankerite, and ~2320-2350nm in siderite (Gaffey, 1987). With Mg^{2+} and Fe^{2+} substituting for Ca^{2+} the position of CO_3^{2-} absorption feature shifts to shorter wavelengths (Thompson et al., 1999; Mathieu et al., 2017). When characterizing unimodal carbonate mineralogy, estimation of relative abundances of carbonate species from hyperspectral imaging is not problematic. Classification of bimodal carbonate mixtures is achievable given that endmember CO_3^{2-} absorption features do not overlap. Previous studies have shown that absorption wavelength positions in calcite-dolomite mixtures is centered at ~2324-2327nm for 25% calcite-75% dolomite, ~2328-2333nm for 50% calcite-50% dolomite, and 2334-2337nm for 75% calcite-25% dolomite (Zaini et al., 2015). Precise carbonate differentiation becomes challenging with CO_3^{2-} feature alone when several carbonates are present in a sample due to significant overlaps in CO_3^{2-} absorption feature (Munro et al., 2018). However, when carbonate group classification is carried out with position of carbonate feature combined with ferrous drop data, a depression or steepening of spectra slope caused by Fe^{2+} incorporation into carbonate crystal structure, carbonate identification with hyperspectral spectroscopy becomes reliable. Additionally, Lampinen et al., 2018 pointed out that, carbonate feature overlaps with ~2350nm absorption feature of chlorite and white mica, as such shape of the carbonate feature and its depth have to be considered for accurate mineral identification.

Biotite is distinguished from phlogopite by second deepest feature caused by Fe-OH at ~2252nm. While Mg-OH absorption feature at ~2330nm is shifted slightly to longer wavelength values (Figure 4, D). Also, in contrast to phlogopite, and Mg-bearing chlorites, biotite spectra are steepened in 1310-1600nm range by Fe^{2+} present in the crystal structure. Spectral responses of chlorite are attributed Fe-OH and Mg-OH bonds, with characteristic absorption bands of Mg-chlorite endmember at ~2250nm and ~2330nm. With Fe^{2+} substituting for Mg^{2+}, both Fe-OH and Mg-OH absorption bands shift to longer wavelengths, attaining values of ~2260nm and ~2358nm in Fe-chlorite endmember (Bishop et al., 2008; Lampinen et al., 2018).

Compositional changes in epidote-clinozoisite series track variations in fluid flux and are sensitive to redox conditions, temperature, permeability, CO_2

concentration, fluid pH, and aqueous speciation of Al^{3+} and Fe^{3+} complexes (Roach et al., 2011). Diagnostic features in epidote are similar to those of chlorite, with the deepest feature at ~2335nm and the 2nd deepest feature at ~2256nm, which makes classification of chlorite-epidote mixtures challenging (Figure x, B). However, with application of ~1550nm feature only present in epidote, differentiation is possible. Both major absorption features in the 2100-2400nm range, and the ~1550nm feature shift to longer wavelengths with increasing Fe content (Roach et al., 2011).

Calcic amphiboles occur in orogenic gold systems and in some case studies distinguishing pre-mineralization from hydrothermal amphiboles has important exploration implications (Laukamp et al., 2012). Calcic amphiboles applicable to current research belong to tremolite series. Tremolite is a Mg-rich endmember in the series, while ferro-actinolite is a Fe-rich counterpart. However, it is possible for the tremolite series amphiboles to deviate towards hornblende series when Al is substituted for Si, moving towards tschermekite, or by Na in the first cation site, moving towards pargasite composition. These substitutions are balanced by Al for Mg and Fe in mineral's crystal structure (Deer et al., 1992). Diagnostic features for amphibole classification in the SWIR range are related to hydroxyl stretching and bending vibrations located near ~2320nm and ~2390nm (Figure 4, B). These features are sensitive to chemical composition in amphiboles and shift to lower wavelength with Fe^{2+} substitution. Absorption features in the 2200-2400nm range by previous studies (Swayze et al., 2009; Laukamp et al., 2011) showed it was difficult for separation of amphibole species in mineral mixtures. Classification becomes challenging when structurally similar minerals, such as talc, are present, or in mineral mixtures with carbonates and Mg-OH/Fe-OH-bearing silicates (Laukamp et al., 2012).

Although tourmaline is a minor alteration component at Sadiola Hill, its presence is well-documented and has to be accounted for. Microprobe analyses of Masurel et al., 2017 indicated that tourmaline at Sadiola belongs to schrol-dravite series alkali group. Diagnostic of this group (Figure 4, D) are absorption features near 2200nm, 2245nm, 2300nm, and 2360nm related to Al-OH, Mg-OH, Fe-OH, and B-OH stretching vibrations (Clarke et al., 1990)

Finally, several limitations to identification of alteration minerals with SWIR hyperspectral imaging have been noted from former studies (summarized after Mathieu et al., 2017):

1) Identification is limited to minerals containing OH or H-OH bond in their crystal lattices.

2) Estimation of mineral abundances can be subjective due to lack of response from quartz and feldspars.

3) Classification of phyllosilicates, namely muscovite and illite, is often challenging due to their similarities in their spectral signatures.

4) Alteration mineral coatings over primary minerals, for instance white mica coating on plagioclase, will result in overestimation of alteration mineral intensities.

5) White mica-clay mineral mixtures have to be excluded from crystallinity calculations due to interference of clays with 1900nm H-OH feature.

Most of the outlined limitations can be resolved with conventional transmitted light microscopy of rock intervals that underwent hyperspectral imaging, allowing for one-to-one comparison of petrographic observations and SWIR hyperspectral mineral maps. Moreover, in current study exact mineral chemistry of carbonates, white mica, biotite, chlorite, and amphiboles is determined with electron microprobe to refine endmember selection and verify spectral interpretation.

3 METHODOLOGY

3.1 Petrography

Samples selected for petrographic analysis were prepared from drill core sections scanned at 26μm resolution for one to one comparison. A total of 36 polished thin sections were prepared at the Oulu Mining School laboratory, university of Oulu. Each thin section was scanned under polarizing films to aid visualization of coarser features and studied using conventional transmitted and reflected light microscopy at multiple magnifications. Mineral contents reported in this manuscript are expressed as modal percentages. Grain sizes are reported as very-fine-grained (< 20μm), fine-grained (20-100μm), medium-grained (100-600μm), and coarse-grained (> 600 μm).

3.2 Electron Microprobe

Electron microprobe analyses were carried out at the Department of Microscopy and Nanotechnology, University of Oulu. Sampling was carried out with electron-probe microanalyzer (EPMA) JEOL Superprobe model JXA-8200. Total number of thin sections analyzed XX. The acceleration voltage of the instrument was 15kV and the beam current was 15nA with spot size for analysis set to10μm. Counting times were set to XX. The following elements were analyzed for silicates and carbonates: Na, S, P, Mn, Cl, Mg, K, Si, Co, As, Ca, Zn, Hg, Al, Fe, Sn, Sb, Ag, Ti, Te. Standards of biotite and plagioclase were inserted in the beginning and at the end of each session to ensure sum of all element concentrations is ~100%. Detailed information about the standards can be found in the Appendix B

3.3 SWIR Hyperspectral

Hyperspectral scanning of 79 drill core samples from 6 diamond holes was conducted at the ITC Geoscience Laboratory, University of Twente. A Specim SWIR Hyperspectral camera was used for image acquisition at two scales- medium resolution (0.2 x 0.2 mm pixel size) with lab stage, and high-resolution (26 x 26μm pixel size) SisuCHEMA setup (Figure 5). After examination of wavelength features at 0.2mm pixel resolution, combined with visual observations of drill core, a total of 37 samples

were selected for high-resolution scanning. The samples were carefully chosen to encompass every alteration type, to ensure various alteration intensities were captured, and each lithologic unit of the deposit was not underrepresented. Samples were placed horizontally in trays filled with silica sand to ensure scanned surfaces were in focus. The samples analyzed at 26 µm resolution were aligned with a laser level installed in the SisuCHEMA stage. Data for each pixel was collected in x-, y-, and z-direction with x- and y-values of the pixel cube corresponding to length and width of a pixel within a horizontally stationed sample. Z-values represent a stack of bands in the SWIR range 1000-2500nm with 12nm spectral resolution, amounting for the total of 288 bands.
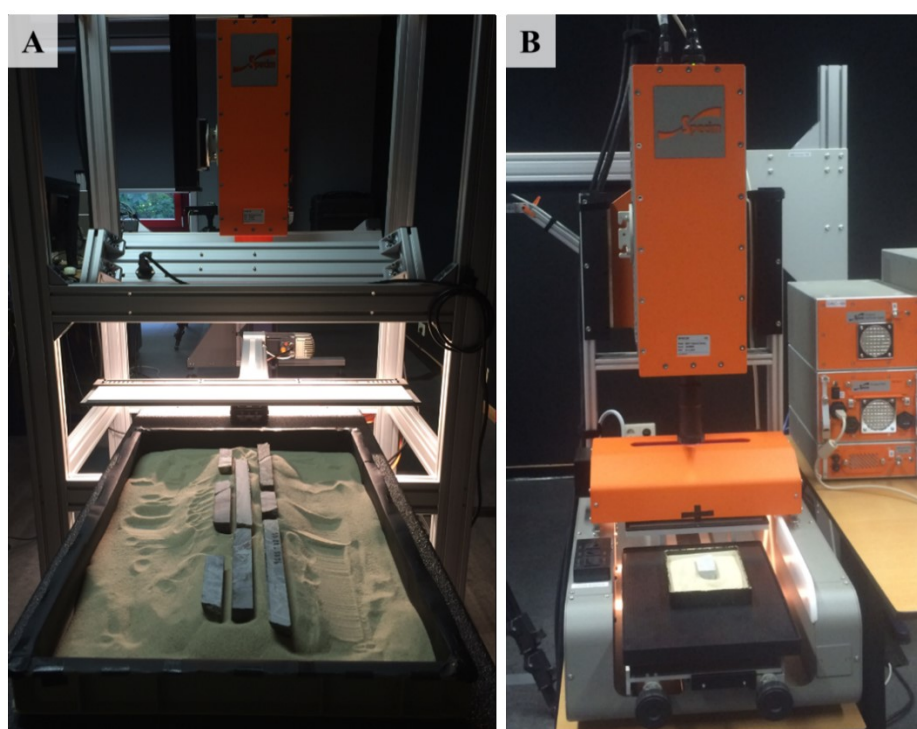
Figure 5. ITC Hyperspectral Lab image acquisition setups **A.** Lab stage with SPECIM hyperspectral camera for scanning at 0.2mm pixel size. **B.** SisuCHEMA setup with SPECIM camera mounted for 26µm pixel scanning.

Conversion of raw image files into calibrated hyperspectral images was done with hyperspectral python ("HypPy"), an in-house software developed in ITC, and Environment for Visualizing Images (ENVI) Classic 5.5 commercially available software package. The main processing steps include image conversion to reflectance via calibration with a dark and white reference, spectral and spatial subsiding, followed by spectra smoothing based on 7 neighboring values (Bakker et al., 2014). In the next step, albedo image or a total reflectance of each pixel was calculated. Wavelength

maps were generated in two steps starting from definition of a deepest absorption feature in a particular wavelength interval. At this stage a continuum removal was performed to highlight spectral absorptions. A second order polynomial fit was modeled to three data points of minimum reflectance in the continuum-removed spectra. The wavelength position of the minimum and depth of the deepest absorption feature was determined through fitting of the polynomial curve or as interpolated parabolic fit. The resulting image contained two bands for each pixel, specifically, position of the deepest absorption feature, and depth of this feature relative to continuum. In the next step a three-band colour image was created from combination of the wavelength position and its depth. In the image, the position of the wavelength controls the hue while the depth of this feature controls colour intensity (Figure 6). The wavelength positions were calculated for 4 different wavelength intervals with the last three maps were created from the same wavelength interval but with different wavelength stretches (2100-2400nm, 2185-2225nm, and 2300-2360nm) (van Ruitenbeek et al., 2014).

Image processing into mineral maps began with project-specific endmember selection. Endmembers were chosen based on manual examination of the drill core samples, petrographic observations and prior knowledge of Sadiola alteration assemblages, namely from Hein and Tshibubudze (2008), Cameron (2010), and Masurel et al. (2017). Mineral classification was conducted in ENVI Classic 5.5 software with decision trees developed for project-specific mineralogy as matching algorithms between endmember spectral expression to spectra from USGS spectral library. A combination of positions and depths of 1st and 2nd deepest diagnostic absorption features were the most common bands utilized in scriptwriting for mineral classification. In addition, mineral properties were assessed with features such as illite crystallinity, in case of white mica classification, or ferrous drop for carbonates. Fundamentally, each decision tree consisted of band output of "0" and "1" correspond to "No" and "Yes" results within the decision tree. Band output of "1" is assigned to a mineral class, while band output of "0" passes through the "NO" branch of the decision tree with additional diagnostic features applied until each pixel is assigned to a specific class.
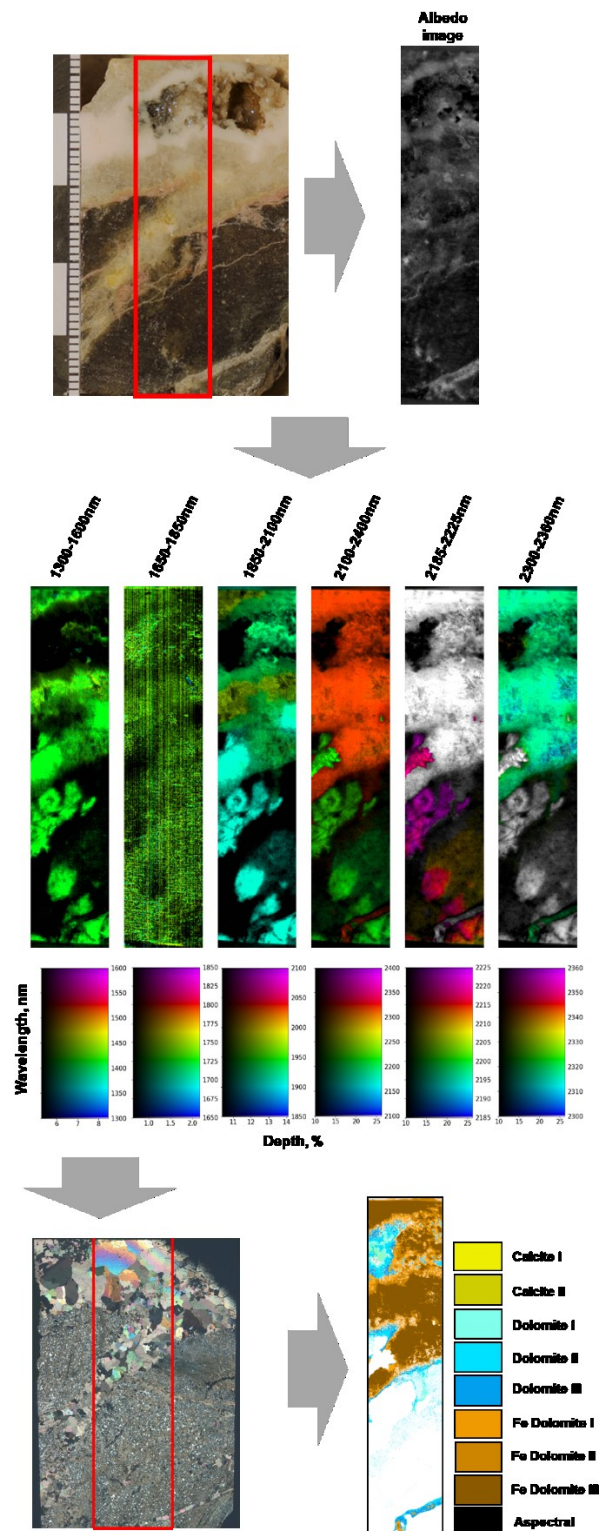
Figure 6. Workflow summary for hyperspectral image acquisition and mineral map generation. Sample scanning at 26µm-pixel resolution followed by calibration and conversion of raw data into hyperspectral data cube and calculation of total reflectance (albedo) image. The next step consists of generation of wavelength maps over 6 intervals in the SWIR range and development of project-specific decision trees. After data validation with transmitted light microscopy and electron microprobe, mineral maps are generated.

Decision Tree for White Mica Minerals Classification

A decision tree for white mica was constructed from combination of illite crystallinity, a ratio of continuum removed depths of Al-OH absorption feature to the depth of water feature at ~1900nm, as well as the position of Al-OH bond (refer to Appendix C.1 for white mica decision tree structure). Crystallinity was divided into 4 classes (>1, >2, >3, >4) based on observed variability in the samples. Two lower crystallinity values corresponded to illite and two upper ones to muscovite. The position of Al-OH bond was assessed with 5nm breaks within the Al-OH feature range, below 2200 nm, 2200-2205 nm, 2205-2210 nm, 2210-2215 nm, 2215-2220 nm, and 2220-2225 nm. Minerals assigned according to the shift of Al-OH absorption feature to longer wavelength included paragonite, muscovite, Al-poor muscovite I, Al-poor muscovite II, phengitic muscovite, and phengite. The following input bands were used for illite/white mica classification decision tree:

- **B1** Illite crystallinity
- **B2** Wavelength position of the deepest feature in 2100-2400nm range
- **B3** Depth of the deepest absorption feature in 2100-2400nm range

Decision Tree for Carbonate Group Minerals Classification

Decision tree for carbonate group minerals was developed based on ferrous drop values- steepening of spectra based on reflectance bands R1600/R1310 ratio (van Ruitenbeen et al., 2018), and position of $(CO_3)^{2-}$ absorption feature (refer to Appendix C.2 for carbonate group minerals decision tree structure). Five breaks with 0.1 increments in ferrous drop ratio ranging from < 1.1 (low) to > 1.5 (very high) were utilized to assess the degree of Fe^{2+} substitution into the carbonate crystal structure. A secondary Fe-OH feature near 2250nm was applied to filter-out Fe-bearing phyllosilicates and epidote from the carbonate classification. The position and expected shifts in carbonate feature for ankerite, dolomite, and calcite were taken from the USGS spectral library and related studies (Kokaly et al., 2017). The following input bands were applied for the carbonate group classification decision tree:

- **B1** Ferrous drop (R1600/R1310)
- **B2** Wavelength position of the deepest feature in 2100-2400nm range

- **B3** Depth of the deepest absorption feature in 2100-2400nm range
- **B4** Wavelength position of the 2nd deepest absorption feature in 2100-2400nm range

Decision Tree for Classification of Chlorite, Epidote, Amphibole, and Tourmaline

Decision tree for classification of chlorites, calcic amphiboles, epidote and tourmaline was developed from combination of wavelength positions and depths of the 1st and 2nd deepest absorption features in the 2100-2400nm range and ferrous drop ratios (refer to Appendix C.3 for decision tree on complete mineralogical classification). Tourmaline was classified by doublet at ~2200 nm and ~2245 nm, and absorption feature at ~2350 nm. Combination of these parameters reliably separated tourmaline from white mica. Diagnosing absorption features combined with ferrous drop were utilized to distinguish tremolite-actinolite amphiboles from carbonate and chlorite. The presence of talc in samples was assessed in the early stages of this study. It has been confirmed with both hyperspectral classification and microprobe tests that talc is absent at Sadiola, as such it has been removed from the final version of current decision tree. Chlorite-epidote mixtures were separated by depth of the 2nd deepest feature around ~2250 nm, as it has been more effective than absorption feature around ~1550nm. Overall, a combination of the following input bands was sufficient for construction of the decision tree for complete mineralogical classification:

- **B1** Ferrous drop (R1600/R1310)
- **B2** Wavelength position of the deepest feature in 2100-2400nm range
- **B3** Depth of the deepest absorption feature in 2100-2400nm range
- **B4** Wavelength position of the 2nd deepest absorption feature in 2100-2400nm range
- **B5** Depth of the 2nd deepest absorption feature in 2100-2400nm range

Each mineral map was verified and refined with petrographic observations and mean spectra for each mineral class generated in ENVI. The latter option assessed shapes and symmetry of absorption features for comparison with examples described in literature. A systematic qualitative comparison of spectrally active features, e.g. carbonate veins or white mica altered argillite laminae, in thin section scans and mineral maps was conducted to determine accuracy of mineral classification. Discrepancies between petrographic observations and the hyperspectral mineral maps

were negligible if the minerals were coarse-grained and a gap between scanned rock surface and the surface from which a thin section was made did not exceed 1mm. However, when the spectrally responsive minerals were sub-pixel in size, accurate estimation of percentages of spectral classes became problematic. This issue will be addressed in detail in the discussion chapter of this manuscript. Finally, the mineral stoichiometry of phyllosilicates, carbonates, and amphiboles was determined with electron microprobe to further verify specific changes in spectral expression, such as shifts of Al-OH feature to longer wavelength in white mica, and relation of ferrous drop to weight percent of FeO in carbonates.

3.4   Geochemistry

A total of 23 samples of diamond drill core were selected for geochemical characterization, including 3 quality assurance/ quality control (QA/QC) samples- one pulp duplicate, one standard, and one blank. Each of the submitted samples has undergone high-resolution hyperspectral imaging. The submitted samples included 9 impure marble samples, 6 greywacke samples, 5 granodiorite samples, and 1 tonalite sample.

Each sample was analysed for major element oxides and trace elements at ALS Global, Sodankylä branch, Finland with ME-ICP81x and ME-MS89L packages. ME-ICP81x method utilizes fusion of 0.2g of a sample fused with sodium peroxide at 700^0C. The melt is diluted with hydrochloric acid after cooling and analysed by inductively coupled plasma- atomic emission spectroscopy (ICP-AES). Lower detection limit for SiO_2 was 0.2%; 0.02% for TiO_2 and Al_2O_3; 0.01% for CaO, Fe_2O_3, K_2O, MgO, and S. Analysed elements were converted to oxide form and reported as weight per cent (www.alsglobal/geochemistry).

Trace elements were analysed by ME-MS89L package: lowest detection limit super trace multi-element analysis by sodium peroxide fusion and induced coupled plasma- mass spectroscopy (ICP-MS). Prepared sample of 0.2g is fused with sodium peroxide at 670^0C and mixed with 30% hydrochloric acid after cooling. The solution is analysed by ICP-MS with results corrected for spectral inter-element interferences.

Analysed elements and their lower and upper detection limits are listed in Appendix A (www.alsglobal/geochemistry).

Total carbon was analyzed with C-IR07 package, by Leco furnace combustion analysis with detection limit range of 0.01-50%. Gold content was determined with Au-ICP21 package, with 30g sample analyzed by fire assay with ICP-AES finish. Au-ICP21 upper and lower detection limit ranges from 0.001-10 ppm. Au-GRA21 package was applied for over limit analyses. To fully eliminate contamination between samples WSH-22, a pulveriser cleaning package, was applied after each sample.

Standard analysed as part of QA/QC was a United States Geological Survey (USGS) disseminated gold ore standard (DGPM-1). Material for the standard comes from Pinson Mine, Nevada. Gold in the reference material occurs as fine particles (<0.5 micron) and association with pyrite and iron oxides. In addition to gold, recommended values for Sb, As, W, Al_2O_3, Fe_2O_3, K_2O, SiO_2, CaO, and MgO are also reported for the standard (Grimes et al., 1996).

4   RESULTS

4.1   Petrography of Country Rocks

4.1.1   Impure Carbonate

The impure carbonate unit is the most volumetrically abundant lithology within the Sadiola Hill deposit. Mineralogically the unit is dolomitic-calcitic marble and is restricted to the footwall of the Sadiola Shear zone. The unit underwent significant folding and recrystallization during the D_3 event (Cameron, 2010; Masurel et al., 2017) syn-depositional folding and slumping has also been reported in previous studies (Hein and Tshibubudze, 2008). Deformation is evident from recrystallization of dolomite-calcite dominant layers (Figure 7, B), as well as from folding and shearing of argillaceous laminae. Increasing strain and recrystallization is expressed in grain-size reduction and development of triple junctions among crystals in the dolomite-calcite layers and alignment of biotite crystals. Greenschist facies peak metamorphic mineral assemblages are normally difficult to recognize due to strong hydrothermal alteration overprint. However, porphyroblastic biotite was recognized within argillaceous laminae of one of the least altered samples (SD28) (Figure 7, A). It has been confirmed with electron microprobe that metamorphic biotite is intermediate Fe-Mg-member of the phlogopite-annite series. The biotite occurs as porphyroblasts up to 4mm long with quartz inclusions and well-developed pleochroic halos around monazite inclusions. Some of the porphyroblasts develop subgrain boundaries evident from kinks in cleave pattern.

Detrital quartz content and abundance of the argillite layers varies within the marble intersected in different drill holes. Hydrothermal minerals are generally restricted to the argillaceous laminae and are represented by fine-grained dolomite-white mica mixtures amounting for up to 20% of the unit's volume.

Sulphides amounting to 5% consist of euhedral arsenopyrite, anhedral pyrite, often replaced by marcasite, pyrrhotite, sphalerite, chalcopyrite, and trace amounts of galena and molybdenite are restricted to argillite bands. Disseminated aurostibite and traces of very fine-grained native gold are found exsolved and replacing arsenopyrite as well as rare individual crystals within hydrothermally altered matrix.

4.1.2 Greywacke

The greywacke is a fine-grained fully recrystallized unit with matrix consisting of 40-50% of fine-grained mosaic of quartz and feldspars, often too difficult to tell the two apart (Figure 7, C). Dolomite comprises 5-20% of the volume and occurrs as fine- to medium grained patches. Well-aligned biotite comprises 20-35% of the unit's volume and occurs fine-grained flaky crystals defining foliation fabric. Biotite is intermediate Fe-Mg in composition based on microprobe studies.

Very fine-grained white mica is a common alteration product are evenly distributed within the matrix, probably replacing pre-existing recrystallized feldspars with quartz remaining unaltered (Figure 7, D). Accessory minerals include apatite and rutile. Traces of rutile are spatially associated with biotite replacement by very fine-grained white mica, with Ti liberated as a result of the replacement and precipitated in the oxide form.

Sulphide morphology and species within the greywacke differ from those within the impure carbonate unit. The greywacke unit generally hosts more pyrrhotite and pyrite in medium-grained blebs or semi-massive lenses. Sulphides related to gold mineralization are less abundant and occur as disseminations associated with biotite and ferroan dolomite

4.1.3 Diorite

Igneous protolith of Sadiola meta-diorite unit was coarse-grained quartz diorite. Feldspars (40- 45%) and quartz (5%) have undergone grain size reduction forming a fine-grained mosaic interconnected with triple junctions. The degree of recrystallization varies among examined samples reaching complete recrystallization in sample SD75 with fine-grained matrix reaching ~70% of the unit's volume. Primary igneous plagioclase was interpreted as anorthite-rich in composition with possible zoning between core and rim. Composition zoning of plagioclase crystals was interpreted as cores being more anorthite-rich. Under greenschist facies metamorphic conditions primary plagioclase was recrystallized to more albitic endmember intergrown with epidote (Figure 7, E). Subhedral medium-grained flaky biotite shows no preferential orientation was likely introduced by K-bearing fluids (Figure 7, F).

Subhedral short stubby hornblende poikiloblasts are zoned with cores containing biotite and apatite and very fine-grained inclusions of biotite oriented parallel to cleavage planes. Rims of hornblende are free of fine-grained biotite inclusions and are intergrown with and enveloping epidote, biotite, and quartz. Some biotite crystals seem to replace hornblende, as such presence of two generations of biotite is possible within the Sadiola ore field.

Epidote occurs as fine-grained euhedral equigranular crystals forming clusters resembling outlines of consumed plagioclase. Clinozoisite end-member occurrences are rare but have been identified in several instances based on anomalous blue interference colour.

Sulphides hosted by the meta-diorite are dominantly pyrite, pyrrhotite, and arsenopyrite typically occurring as medium-grained blebs and disseminations. Accessory mineral phases include apatite and rutile.

4.1.4 Tonalite

Tonalite was recorded in one sample where the unit was in contact with the greywacke. Tonalite shows strong evidence of progressive shearing and grain size reduction. Equigranular quartz porphyroclasts, amounting for ~5% of tonalite's volume, exhibit progressive deformation features ranging from low strain evident from onset of undulatory extinction to high strain with porphyroclasts undergoing partial recrystallization and forming σ-grains with finer quartz recrystallizing in the pressure shadows (Figure 7, J).

Fine-grained recrystallized quartz-feldspars matrix comprises ~80% of the sample. White mica occurs as very fine-grained flakes, preferentially oriented in the direction of shearing, and replaces up to 35% of feldspars within the matrix. Felspar porphyroclasts comprise 5% of tonalite's volume. Feldspars that have not undergone complete recrystallization occur as coarse-grained short prismatic crystals with well-developed sutured boundaries and are heavily replaced by fine- to medium-grained accumulations of white mica (Figure 7, I). Biotite (~5%) occurs as fine-grained anhedral flakes, pleochroic from light to dark brown, and is oriented subparallel to the shearing fabric. Overall, the tonalite is not well-mineralized with only traces of pyrrhotite and pyrite recognized.
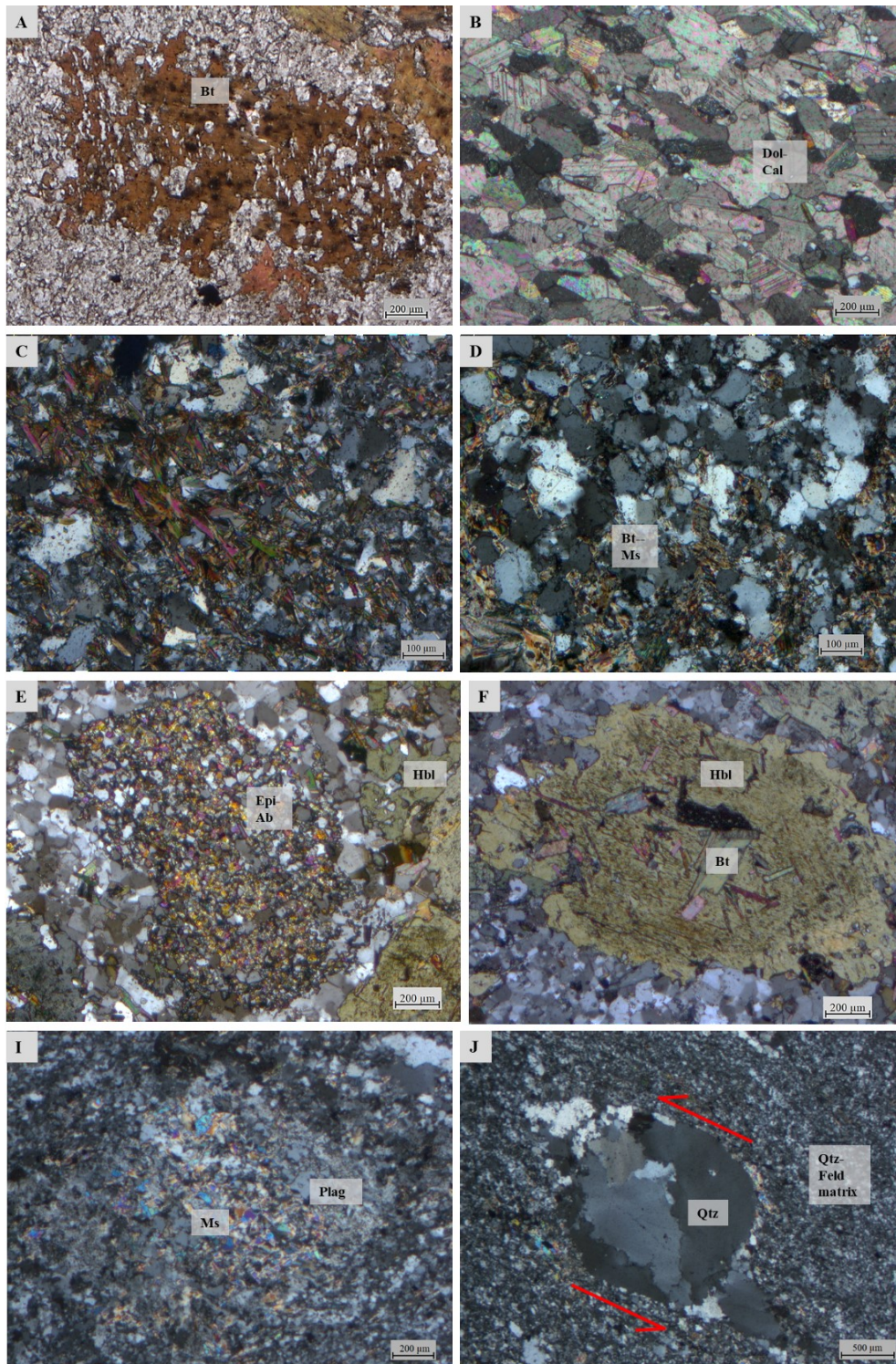
Figure 7. A. and **B.** Photomicrographs of least altered impure carbonate sample (SD28) showing biotite porphyroblasts (A), and recrystallized dolomite-calcite matrix (B). **C.** and **D.** Photomicrographs of a typical greywacke showing variable degree of K-metasomatism **E.** Epidote-albite metamorphic replacement of plagioclase phenocryst in diorite. **F.** Hornblende intergrown with biotite in hornfelsed part of diorite. **I.** Muscovite replacement and partial recrystallization of relict feldspar phenocryst in tonalite unit. **J.** Quartz porphyroclasts within tonalite showing signs of sinistral shearing and development of subgrains (Abbreviations: Ab = albite, Bt = biotite, Cal = calcite, Dol = dolomite, Epi = epidote, Feld = feldspar, Hbl = hornblende, Ms = muscovite, Plag = plagioclase, Qtz = quartz).

4.1.5 Alteration

Vein-controlled quartz is the earliest hydrothermal phase recognized petrographically. Its relative timing is constrained by cross-cutting relationships with carbonate-white mica veins and inferred from greater strain in comparison to later alteration facies. Most of the early quartz is restricted to greywacke and early diorite lithologic units.

Albite occurs as widespread pervasive alteration phase in greywacke and diorite either as partially recrystallized medium-grained elongate crystals with well-developed sutured boundaries (Figure 8, A) or as completely recrystallized fine-grained mats mixed with primary quartz and feldspars. A clear evidence of albite timing was constrained in sample SD92_01 where ore-stage Fe-carbonates brecciate strongly albitized diorite. Marble is albitized to a lesser degree reflecting lower abundance of Al, however it does occur as a minor pre-mineral phase in samples SD30 and SD69.

Main stage K-metasomatism is represented by pervasive biotite within the greywacke and the diorite and white mica with lesser biotite in marble. Although white mica also occurs in greywacke and diorite it appears as a later phase in timing relative to biotite (Figure 8, B and C). Within well-mineralized argillite laminae in marble phlogopite endmember appears to coexist with Al-poor muscovite (Figure 8, D). Conflicting timing relationship between muscovite and biotite is interpreted as recrystallization of phlogopite as a later phase relative to main phase hydrothermal biotite. This interpretation is consistent with phlogopite introduction after sulphidation reactions have taken place and iron from intermediate member biotite was consumed by formation of arsenopyrite-pyrrhotite-pyrite assemblage co-genetic with gold.

Within marble metamorphic biotite is variably replaced by white mica reflecting intensity of hydrothermal alteration. Intensity of replacement ranges from traces of Al-poor muscovite replacing edges of biotite (sample SD28), incomplete replacement of 40-50% of biotite crystal volume in moderately altered sample (SD69), or almost complete replacement when 70-80% of biotite is consumed (Figure 8, D). White mica compositionally ranges from Al-poor muscovite to more phengitic, although not reaching ideal phengite composition. Variation in white mica chemistry is discussed in detail in sub-chapter on electron microprobe results.
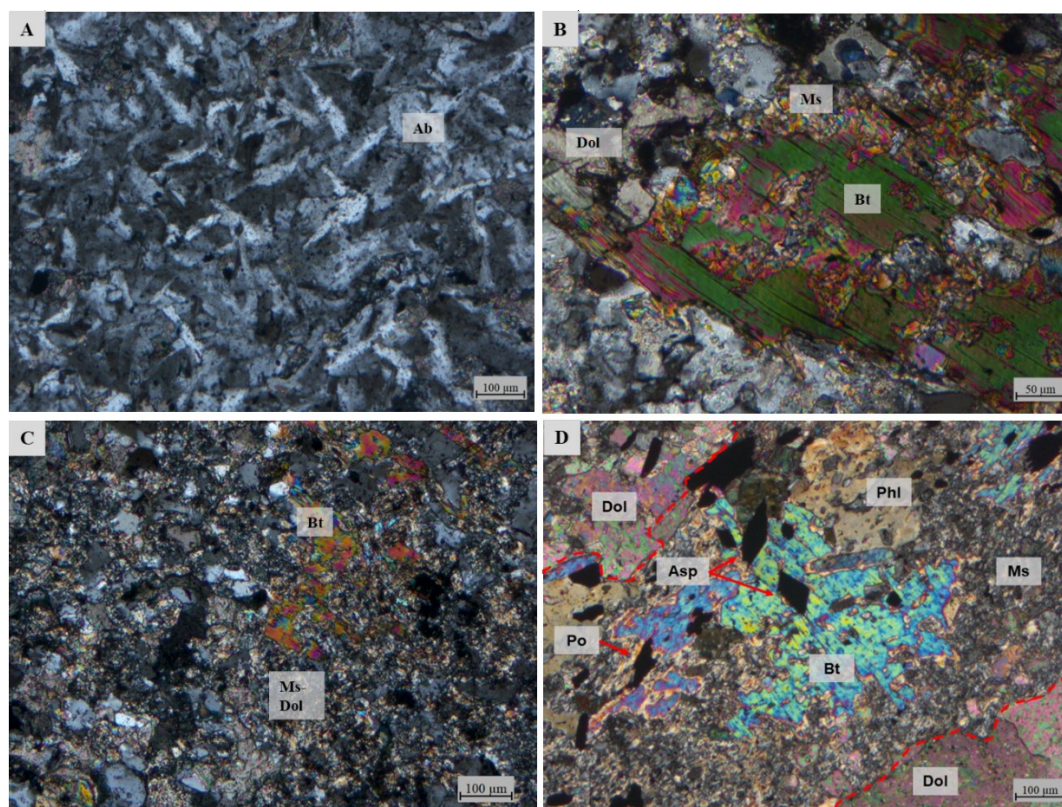
Figure 8. Photomicrographs under crossed nicols of **A.** Pervasive albitization of greywacke by lath shaped albite with sutured boundaries. **B.** incomplete replacement and **C.** strong replacement of biotite by muscovite-dolomite. **D.** Muscovite-dolomite alteration within argillaceous lamellae in carbonate rock (outlined in dashed red line), co-genetic to introduction of arsenopyrite-pyrrhotite and recrystallization of phlogopite. Abbreviations: Ab = albite; Asp = arsenopyrite; Bt = biotite; Dol = dolomite; Ms = muscovite; Phl = phlogopite; Po = pyrrhotite; Qtz = phengite.

Introduction of white mica is cogenetic to pervasive and vein-controlled Fe-bearing carbonate alteration. Hydrothermal dolomite is visually distinguishable from primary host-rock carbonate assemblages by patchy appearance and coarser crystals with irregular boundaries lacking triple junctions. Similar pervasive carbonate alteration signature is observed in the greywacke and diorite units, although dolomite within the greywacke is more Fe-rich and approaches ferroan dolomite composition. Ore-stage vein-controlled ankerite-ferroan dolomite assemblages are exclusive to greywacke and diorite units, consistent with higher iron availability of these units. Vein-controlled dolomite-ankerite assemblages are coarse-grained and typically have exsolution lamellae and zoning patterns indicative of a complex growth history (Figure 9, A and B). Some ankerite-ferroan dolomite crystals adjacent to vein walls contain fluid inclusions concordant to crystal growth pattern (Figure 9, B). Inclusions of very fine-grained sericite are also common.

Calcite is present in the Sadiola ore system as the latest stage barren alteration mineral. Its emplacement timing is well-constrained by cross-cutting and offsetting of muscovite veins and reopening and microbrecciation of ore-stage ankerite-Fe-dolomite veins in greywacke and diorite.

Chlorite occurs as minor alteration mineral as rare hairline veinlets and replacement product of biotite (Figure 9, C), with complete chloritization of biotite being uncommon. Intergrowths with acicular radiating actinolite where the two minerals alter clasts within a coarser-grained part of the greywacke were also reported. Actinolite is also found without chlorite associations forming euhedral elongate tabular crystals arranged in radiating pattern with dolomite occupying interstices between the crystals (Figure 9, D).
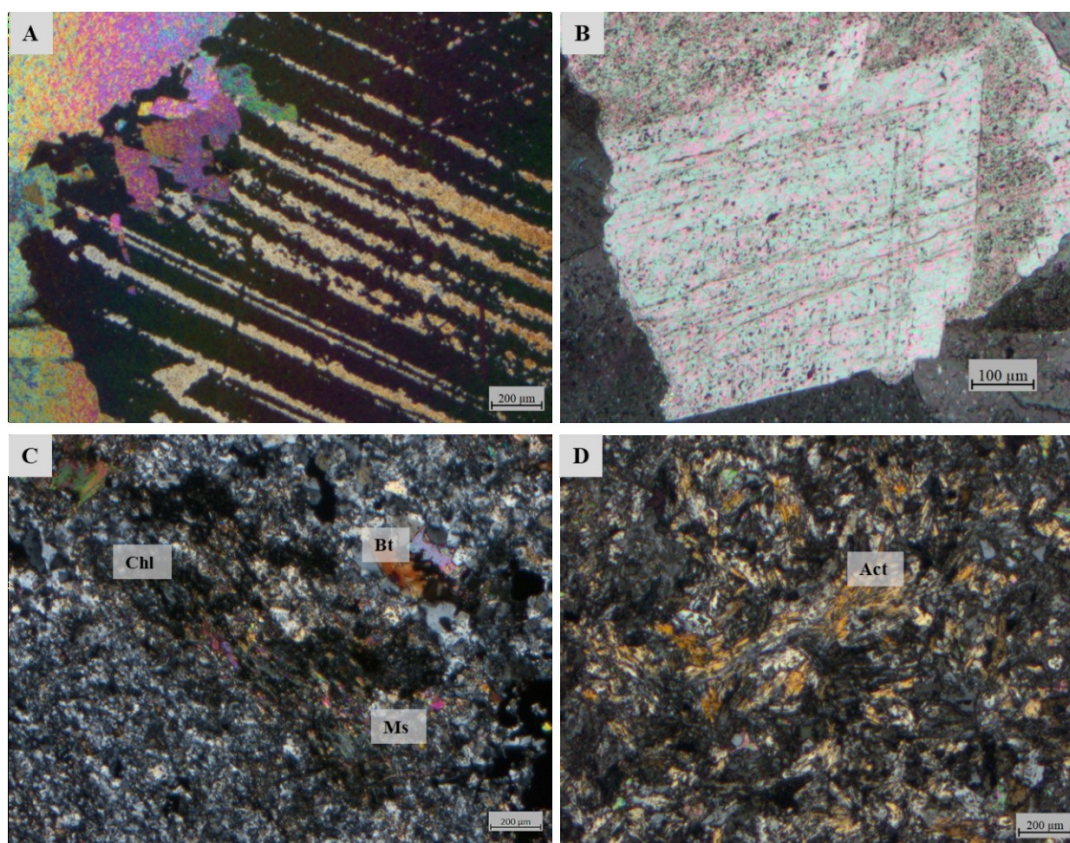
Figure 9. Photomicrographs under crossed nicols of **A.** Complex exsolution lamellae in dolomite-ankerite vein within greywacke. **B.** Fluid inclusions trails parallel to ferroan dolomite crystal growth pattern in syn-mineral vein cutting greywacke **C.** Strong replacement of biotite porphyroblasts by chlorite-muscovite aggregates. **D.** Actinolite mats preferentially replacing coarse sand sized clast within greywacke. Abbreviations: Act = actinolite; Bt = biotite; Chl = chlorite; Ms = muscovite; Phg = phengite.

Miscellaneous minor hydrothermal phases include tourmaline and scapolite. Tourmaline is a relatively minor alteration phase occurring in two forms: either as coarse-grained euhedral crystals intergrown with or replacing quartz (Figure 10, A) or as fine-grained euhedral mats and patches often adjacent to biotite accumulations. Its emplacement timing has not been well-constrained and was interpreted as early syn-mineral. Scapolite is a rare alteration mineral occurring as patches overgrowing hydrothermal albite (Figure 10. B). Dominance of meionite endmember has been interpreted from interference colours.

Apatite and epidote are mineral phases related to metamorphism and skarnification. Apatite occurs in the marble, greywacke, and diorite units as accessory fine-grained elongate prismatic crystals or as subrounded grains when cut perpendicular to C-axis (Figure 10, D). Overall, no preferential orientation has been observed in apatite. Epidote is restricted to diorite and narrow zone at diorite - marble contact. Origin of epidote within diorite is consistent with metamorphic decomposition of anorthite rich plagioclase into epidote-quartz-albite. In rare instances epidote is intergrown with an amphibole of intermediate hornblende-hastingsite composition, which has been confirmed with microprobe. (Figure 10, C). Epidote at a contact of diorite and impure carbonate represents exoskarn assemblages and originated from emplacement of igneous units into the impure carbonate unit. Abundance of amphibole is most likely related to hornblende hornfels contact metamorphism consistent with multiple generations of intrusive emplaced in the basinal metasedimentary package.
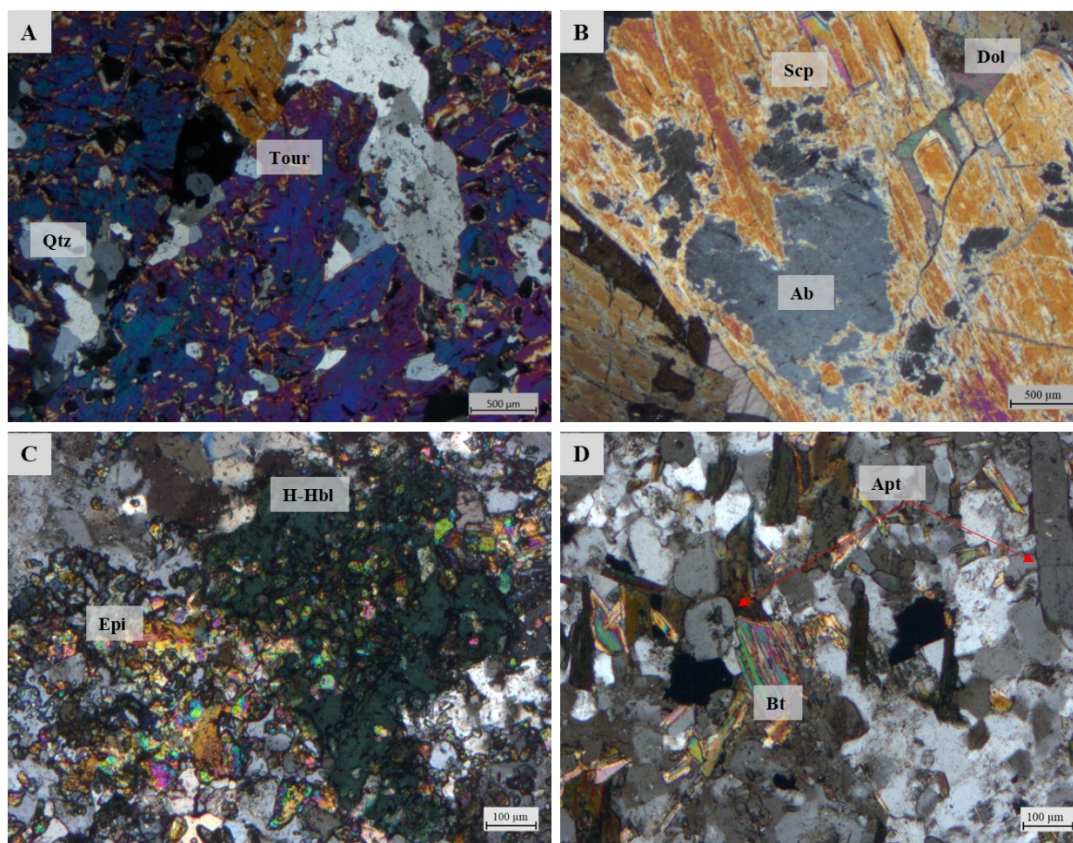
Figure 10. Photomicrographs under crossed nicols of **A.** Tourmaline intergrown with quartz **B.** Scapolite-quartz-albite vein with interstitial dolomite **C.** Epidote-aegirine aggregates in recrystallized quartz-feldspar matrix. **D.** Apatite crystals cut parallel and perpendicular to C-axis. Abbreviations: Ab = albite; Apt = apatite; Bt = biotite; Dol = dolomite; Epi = epidote; H-Hbl = hastingsitic hornblende; Scp = scapolite; Tour = tourmaline; Qtz = quartz

4.1.6 Mineralization

The sulphide species of Sadiola Hill previously documented by Masurel et al. (2017) have been confirmed with reflected light studies in this project. Sphalerite was recorded in sample SD119-SD64 as coarse (~ 4 mm) crystals with compositional zoning between Zn-rich and Fe-rich layers (Figure 11, A) or as blebby crystals ~0.1mm in size. In both cases sphalerite is associated with pyrite-marcasite mineralization. Arsenopyrite occurs in euhedral rhomb-shaped or prismatic crystals ranging in size from 20-100μm, and often forming accumulations, or distributed as sporadic disseminations in argillite laminae. Arsenopyrite crystallized earlier than pyrite and after pyrrhotite based on replacement relationships. (Figure 11, C and E).

Traces of chalcopyrite typically replace the margins of pyrite and sphalerite (Figure 11, B) or form intergrowths with the latter (Figure 11, D). These observations

suggest a cogenetic crystallization of pyrite-sphalerite-chalcopyrite. Molybdenite is uncommon and was observed once as independent needle-like crystals ~3μm long in proximity with other sulphides.

Free gold was recognized by internal reflections and deep yellow colour in samples SD782-SD30 and SD782-SD32. In these samples gold occurs as subrounded grains 3-7μm in diameter either in associations with sulphides (Figure 11, B) or as individual crystals with Fe-dolomite-white mica-phlogopite gang alteration minerals.

Iron sulphides are present as three mineral species: pyrrhotite, pyrite, and marcasite. Pyrrhotite is the most volumetrically abundant iron sulphide typically occurring as coarse blebs and or semi-massive lodes reaching several centimetres in width. Pyrite is the second most iron abundant sulphide introduced after pyrrhotite (Figure 11, E). In general pyrite is heavily replaced by marcasite that forms characteristic lamellar mats that sometimes pseudomorph pyrite crystals. The remnant pyrite makes up only 10-20% of the original pyrite volume (Figure 11, B, D, and E).
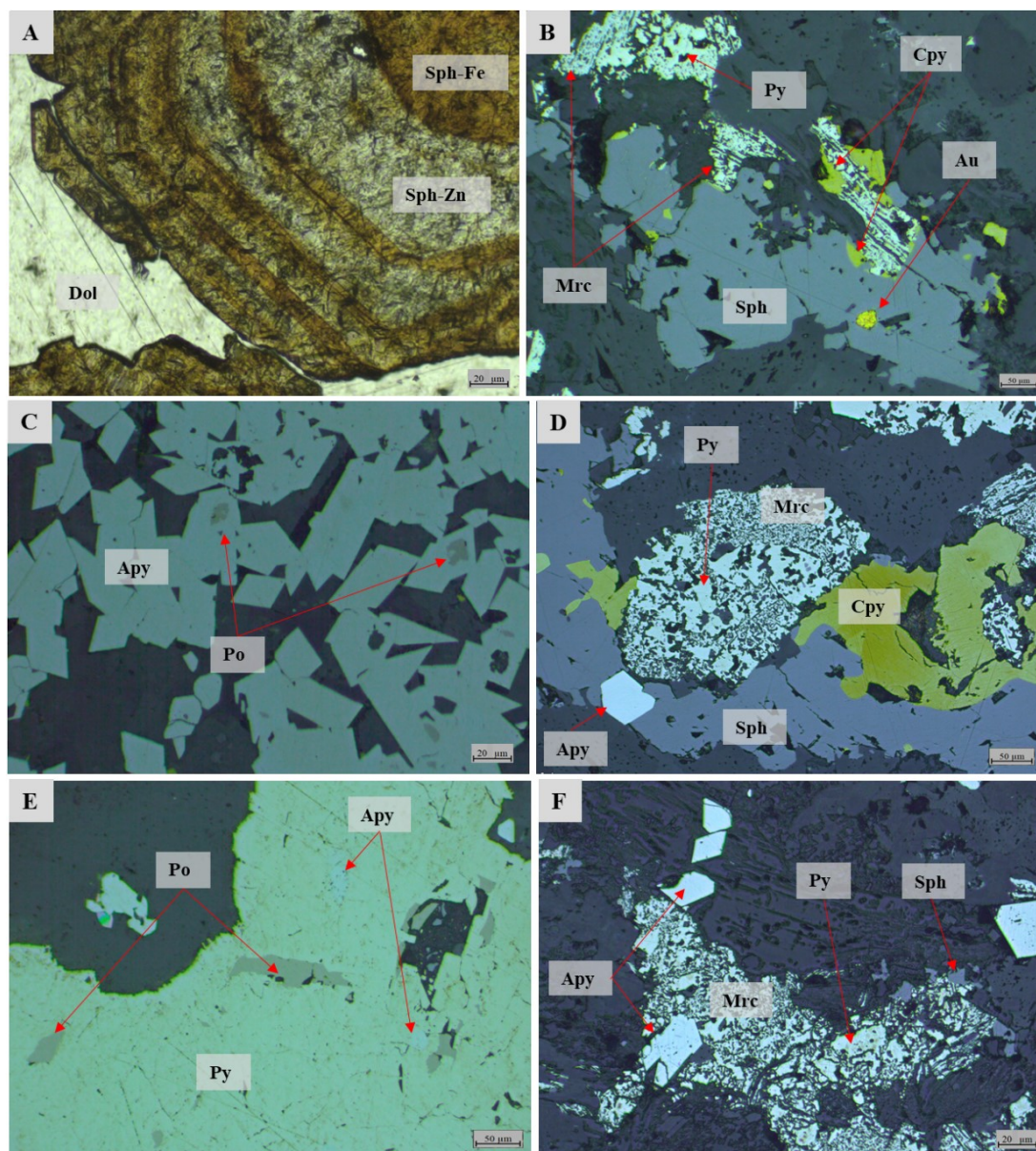
Figure 11. Photomicrographs taken in transmitted plain polarized light (A) and reflected light (B - E) showing relationships among sulphides and gold at Sadiola Hill. **A.** Zoned sphalerite on vein wall of a dolomite vein (sample SD119-SD64). **B.** Sphalerite-chalcopyrite-pyrite-marcasite- free gold assemblage. Note: the image was taken at higher saturation (1.4) to distinguish gold from chalcopyrite (sample SD782-SD30) **C.** Arsenopyrite with pyrrhotite cores (sample SD782-SD32). **D.** Arsenopyrite enveloped by sphalerite-chalcopyrite intergrowths cogenetic with pyrite replaced by marcasite at a later stage (sample SD782-SD30). **E.** Pyrite crystal with pyrrhotite-arsenopyrite inclusions (sample SD782-SD32). **F.** Heavy replacement of pyrite by marcasite with arsenopyrite and sphalerite unaffected by the replacement (sample SD782-SD30). Abbreviations: Au = gold; Apy = arsenopyrite; Cpy = chalcopyrite; Mrc = marcasite; Py = pyrite; Po = pyrrhotite; Sph = sphalerite.

4.2 Electron Microprobe

Chemical composition of white mica, carbonates, chlorite, and biotite was tested with electron microprobe to validate hyperspectral signatures of these minerals. EPMA analyses were carried out with paragenetic context of the minerals. Specifically, it has been noted if a mineral's alteration style is vein-controlled or pervasive in character, or whether a mineral is part of metamorphosed wall rock assemblage. All electron microprobe analyses taken as part of this study are reported in Appendix D.

4.2.1 Carbonate Group

During the current microprobe study, all major elements were measured in the oxide form and reported as weight percent. In case of carbonates, total was in the range of 54-57%, since CO_2 content is not measured by the instrument. Molar proportions of cations and carbonate group anion were calculated based on stoichiometric properties of carbonates defined by Deer et al. (1992). Carbonate minerals evaluated in this study were calcite ($CaCO_3$,) dolomite ($CaMg(CO_3)_2$), ferroan dolomite ($Ca(Mg,Fe)(CO_3)_2$), and ankerite ($Ca(Fe,Mg,Mn)(CO_3)_2$), and siderite ($FeCO_3$). Cation occupancy within carbonate crystal structure was also taken into account during these calculations. Total percentage of carbonate was determined based on recalculated CO_2 content. Several samples had total values slightly over and below 100%, which has been attributed to analytical errors related to crystallographic properties of carbonates and size of incident beam of the instrument ($1\mu m$). Analyses where the error exceeded 7% were excluded from interpretation, for the rest of the analyses the total percentage was corrected to 100%. The results presented herein show carbonate mineralogical composition based on stoichiometric molar cation and anion proportions within carbonate crystal structure, or atoms per formula units (apfu).

Dolomite, Fe-dolomite, and ankerite were classified with Mg/(Mg+Fe) apfu ratio, with values approaching 1 representing dolomite. Analyses with Mg/(Mg+Fe) ranging from 0.63-0.80 were classified as Fe-dolomite. Differentiation of ankerite from Fe-dolomite was challenging due to similarities in the mineral's empirical

formulae. In this study, ankerite was assigned to carbonate measurements with Mg/(Mg+Fe) < 0.63, that also contained minor Mn in crystal structure.

Fracture-fill calcite veins, representing the latest stage carbonate event, occur in all major lithologic units. Chemically calcite was separated from dolomite and ankerite based on Ca apfu approaching 2. Ratio of Ca/(Mg+Fe+Mn) in these analyses was > 10, and approaching 200 in most pure calcite samples, indicating that minor substitutions of Mg, Fe, and to lesser degree Mn, occurred in the calcite.

Overall, Fe content in carbonates shows a continuous range of values from 0 in pure dolomite and calcite to the highest value of 0.46 apfu in ankerite corresponding to FeO 16.7 weight %. Ferrous drop values utilized as one of the main features for carbonate classification with decision trees, have been verified with current electron microprobe study (Figure 12). In general, ferrous drop, representing steepening of carbonate spectra, correlates well with measured amount of Fe in crystal structure, with Fe ≥ 0.35 apfu (≥ 13 FeO weight %) corresponding to very-high Fe drop > 1.5. A slight overlap in Fe content of high and very-high Fe drop amount is attributed to compositional zoning and inhomogeneous nature of carbonates tested in this study.
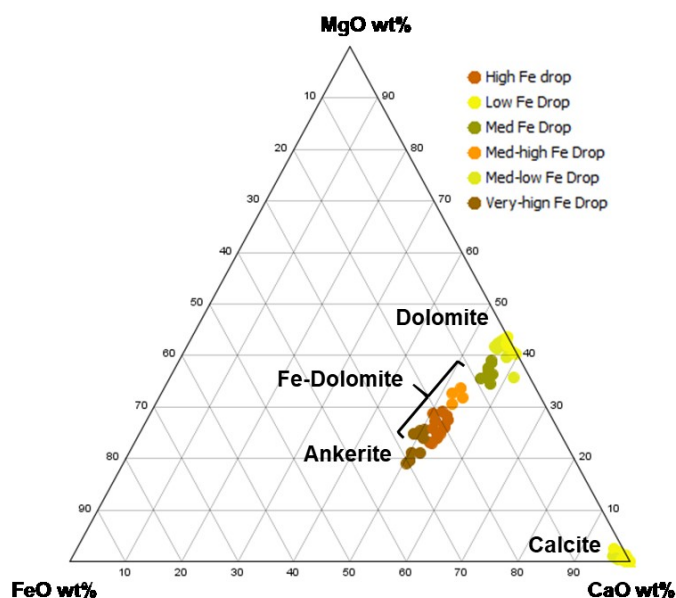
Figure 12. Ternary diagram showing relationship between ferrous drop in carbonate spectra and amount of iron substituted in carbonate crystal structure based on electron microprobe measurements.

Carbonate comprising primary wall-rock marble of the least altered samples (e.g. SD28) is of dolomitic-calcitic composition. Dolomite veins cutting the marble are

slightly enriched in Fe, in comparison to the least altered wall-rock dolomite, attaining Fe content of ~0.08 apfu (Figure 13, A). Two types of carbonate veins cut diorite: dolomite with Fe ~ 0.11 apfu, and calcite (Figure 13, B). Dolomite in pervasive alteration patches in the diorite has the same magnitude of Fe substitution as the dolomite veins. The greywacke shows the most diverse range of carbonate composition. The most Fe-rich dolomite and ankerite are restricted to greywacke as both vein-controlled (Figure 13, D) and pervasive alteration (Figure 13, C). Calcite veins, although not as abundant as dolomite-ankerite veins, also cut the greywacke.
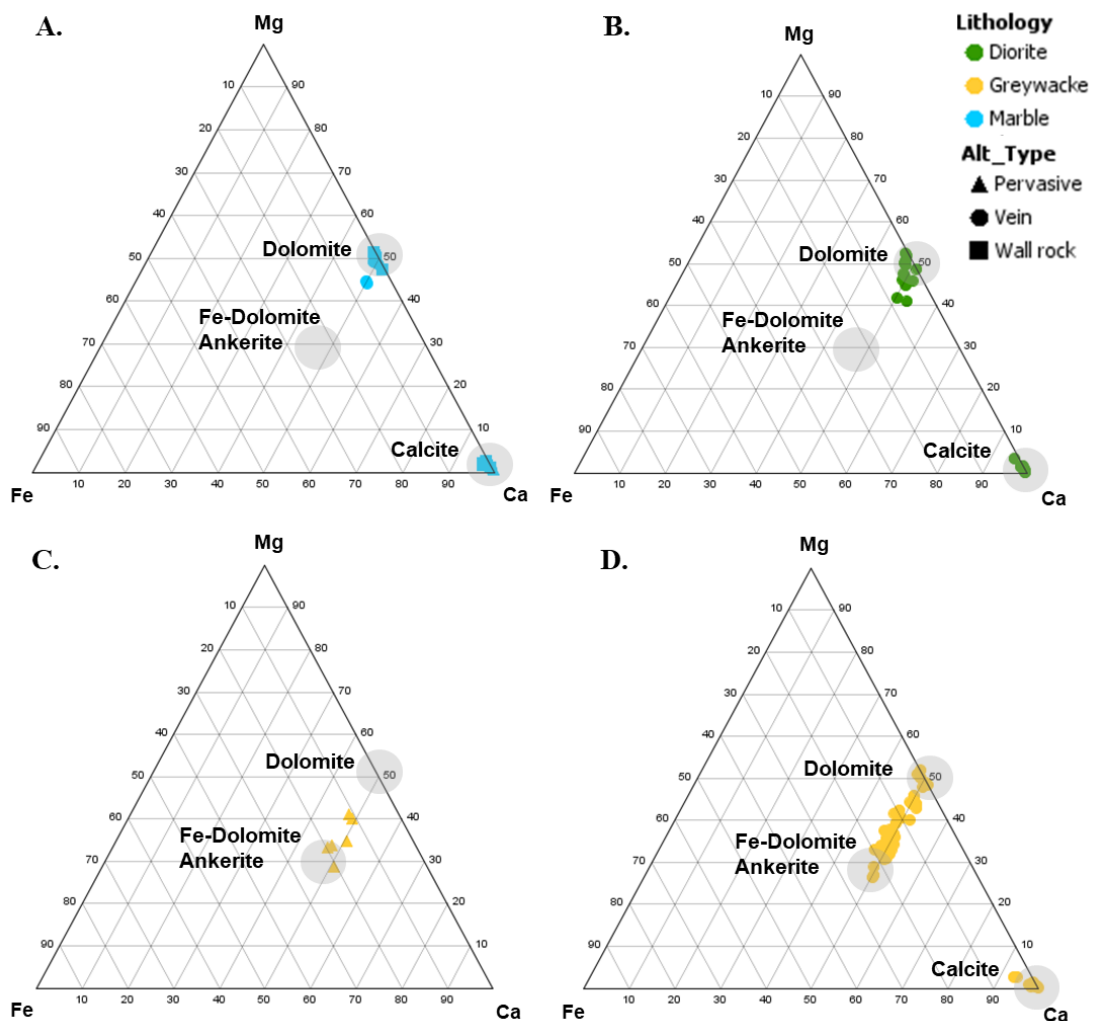
Figure 13. Ternary diagram showing variation of carbonate mineralogy in marble, greywacke, and diorite at Sadiola Hill. **A.** Composition of primary and vein-controlled carbonate in the dolomitic-calcitic marble. **B.** Vein-controlled dolomite in diorite. **C.** Pervasive Fe-dolomite alteration of the greywacke. **D.** Vein-controlled carbonate ranging from dolomite to Fe-dolomite/ankerite, as well as late calcite within the greywacke. Elements in the diagram are plotted as molar values.

Finally, compositional zoning of carbonates was also investigated with the electron microprobe studies. Zonation characterizes late stages of dolomite crystal growth, likely reflecting access of Fe and Mg cations in residual hydrothermal fluid. The cations are then incorporated into the crystal structure resulting in a growth of Fe-rich/Mg-depleted bands that alternate with Mg-rich/Fe-depleted bands. This process continues until the fluid attains composition closer to the initial composition at the start of crystallization (Figure 14).
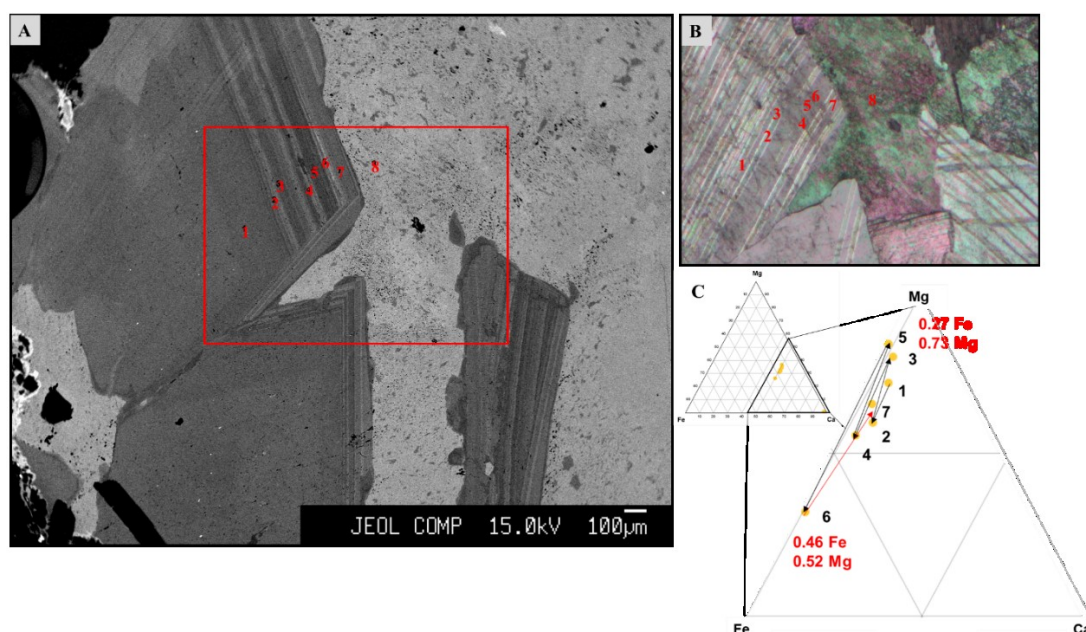
Figure 14. A. Back-scattered electron image of euhedral Fe-dolomite with complex compositional zoning near the vein-wall and interstitial calcite, numbers represent order and locations at which electron microprobe measurements were taken. **B.** Photomicrograph taken under crossed polars corresponding to the area outlined by red rectangle in A. **C.** Ternary diagram illustrating fluctuations in Fe and Mg content in apfu during late stages of Fe-dolomite crystal growth.

4.2.2 Phyllosilicates

Endmember calculations for phyllosilicates were based on empirical mineral formulae from Deer et al. (1992). Summary tables showing individual analyses of phyllosilicates are listed in Appendix B. White mica includes muscovite $(K_2Al_4[Si_6Al_2O_{20}](OH,F)_4)$, with paragonite representing Na substitutions of the K, and phengite in which octahedral Al is substituted by Mg. In the analyzed samples, chemical compositions of white mica ranges from Al-poor muscovite closely approaching ideal muscovite composition (Figure 15). This group of muscovite was

classified by Al number in the chemical formula in a range of 5.15 - 5.25, and lower Mg/(Mg+Fe) ratios of ~ 0.71. Whereas, the white mica approaching phengitic composition shows continuous decrease in Al content to 4.15 - 4.20 apfu, and significant increase in Mg/(Mg+Fe) molar ratios to 0.84 – 0.87. Pure paragonite endmember was not verified in these EPMA studies. The maximum Na content in the first cation position reaches 0.12-0.18 apfu, compared to an average K content of ~1.16 apfu. White mica occurs in every examined rock type of the Sadiola Hill. Analyses conducted on white micas from the greywacke and the marble show the most diverse range in chemical compositions (Figure 15, A and B). However, fewer samples of the diorite and tonalite were available for the EPMA studies of phyllosilicates. As such both diorite and tonalite are underrepresented in this study.

Biotite chemical composition $(K_2(Mg,Fe^{2+})_{6-4}(Fe^{3+},Al,Ti)_{0-2}[Si_{6-5}Al_{2-3}O_{20}](OH,F)_4)$ was assessed for Mg content in the phlogopite - annite series, representing Mg and Fe endmembers, with the aim of establishing chemical differences between metamorphic and hydrothermal biotite. In general, biotite shows a continuous range in Mg-Fe content that falls between the intermediate and the phlogopite endmember compositions. Measurements taken on biotite porphyroblasts in the marble unit and unmineralized greywacke samples indicated intermediate composition of biotite. Hydrothermal biotite composition showed continuous transition to phlogopite endmember in all four lithologic units, attaining the highest Mg content in marble consistent with greater alteration intensities (Figure 15, B). The phlogopite is characterized by high Mg/(Mg+Fe) numbers of 0.84 - 0.86, comparing to 0.62 - 0.70 in biotite. K content in the studied biotite - phlogopite samples ranges from 1.42-1.72 apfu with no correlation to Mg/(Mg+Fe) ratios. Within well-mineralized samples phlogopite occurs as gangue silicate adjacent to or spatially related to sulphides and the ore-stage Fe-bearing carbonates.

The chlorite group $(Mg,Fe^{2+},Fe^{3+},Mn,Al)_{12}[(Si,Al)_8O_{20}](OH)_{16})$ is assessed within the Mg-rich clinochlore and Fe-rich chamosite series framework. Since chlorite at Sadiola is hydrothermal in origin and occurs mainly as replacement product of biotite, classification with clinochlore /chamosite ratios and Mg/(Mg+Fe) content in the crystal structure was sufficient. It has been determined that the intermediate Fe-Mg chlorites contain Mg/(Mg+Fe) ranging from 0.50 to 0.60 and represented by low clinochlore abundances of ~ 0.30. Mg-rich chlorites are characterized by Mg/(Mg+Fe)

in a range of 0.70 - 0.75 with corresponding clinochlore content of ~0.6 - 0.7. These data suggest that the chlorite chemical composition at Sadiola Hill was largely controlled by the Mg-Fe content in biotite, with the Mg-Fe being incorporated into the chlorite crystal structure during hydrothermal replacement without major losses.
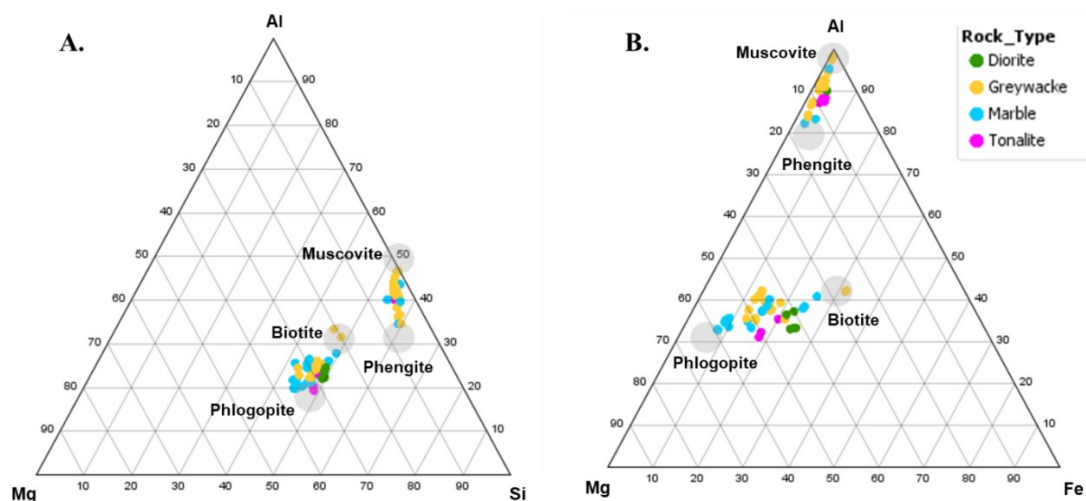
Figure 15. A. Ternary diagram showing variations in Sadiola Hill mica compositions. **B.** Ternary diagram highlighting Tschermak substitutions in muscovite-phengite and transition of intermediate biotite to phlogopite endmember. Figures generated in ioGAS. Element abundances reported in atoms per formula units (apfu).

4.2.3 Amphiboles

Amphiboles were assessed according to a general formula $A_{0-1}B_2C_5T_8O_{22}(OH,F,Cl)_2$ outlined by Deer et al. (1992). Only nine reliable readings were obtained from the amphiboles. Two types of amphiboles were identified with EPMA:

1) $(Na,K)_{0.27}(Ca_{1.9}Fe^{2+}_{0.3})_{2.2}(Mg_{3.0}Fe^{2+}_{1.58}Al^{VI}_{0.34})_5(Si_{7.6}Al^{IV})_8O_{22.7}(OH,Cl)_{1.3}$

2) $(Na,K)_{0.7}(Ca_{1.9}Fe^{2+}_{0.3})_{2.2}(Mg_{2.0}Fe^{2+}_{2.0}Al^{VI}_{0.85})_5(Si_{6.5}Al^{IV})_8O_{22.6}(OH,Cl)_{1.3}$

The first amphiboles were collected from the early diorite (samples SD119-SD55 and SD129-SD75). Based on stoichiometric recalculations the first amphibole was classified as hornblende with minor hastingsite component. Chlorine content of 0.016 weight % is consistent with this interpretation. The second, which is a volumetrically more abundant amphibole, approached hornblende *sensu stricto* composition (Deer et al., 1992). The spatial context of the hornblende-bearing diorite samples and chemical

composition of these amphiboles indicate a hornblende hornfels contact metamorphism origin of the hornblende.

Finally, the intermediate composition of tremolite-ferro-actinolite series calcic-amphiboles, approaching Mg-rich composition, was verified. Actinolite-tremolite, occurring in sample SD048-SD88 as patches up to 15mm in diameter, represents the mineral assemblages interpreted by Masurel et al. (2017) as an early high temperature calc-silicate phase. Substitutions of Al in the C cation site reaching 0.5 apfu further support the high temperature origin of these amphiboles (Deer et al., 1992; Leake et al., 1997).

4.3   SWIR Hyperspectral Imaging

4.3.1   White Mica

White mica at Sadiola occurs over a wide range of spectral classes, reflecting variations in chemical composition. Five spectral classes have been identified based on Al-OH position in 2190-2225nm range. These five classes occur over four ranges of illite crystallinities subdividing white mica into illite and muscovite.

Illite occurs as fine-grained flakes in the argillite laminae of the marble and the greywacke. Composition of the illite varies significantly corresponding to Mg number in the crystal structure. Position of the Al-OH feature in illite is typically centered at 2203nm, 2208nm, or 2214nm (Figure 16, D). At microscale position of the Al-OH bond often shifts to the longer wavelength when illite is replacing biotite, e.g. SD782-SD28, consistent with $Mg2+$ cation transfer into white mica crystal structure. Vein-controlled illite is also affected by the cation exchange with the host rock, leading to Tschermak substitution in illite crystal structure. Position of Al-OH in sample SD042-SD83 ranges from 2214nm in the vein halo where pre-existing biotite was replaced to 2208nm in the vein centreline. Similar pattern was observed with crystallinity in sample SD048-SD93 where Al-poor muscovite with Al-OH at 2208nm transitioned to highly crystalline muscovite into the vein (Figure 16, B).

Phengitic white mica is less common than the Al-poor and muscovite species. Phengites typically occur as fine-grained pervasive patches, or as aggregates reopening ore-stage Fe-bearing carbonate veins. Al-OH absorption feature in phengites is

positioned at 2225nm (Figure 16, A). Illite and muscovite also occurs with Al-OH at 2219nm, prefix "phengitic" is added to the mineral in these instances.

Paragonitic illite altering sample SD042-SD86 has Al-OH absorption feature centred at 2197nm (Figure 16, C). Paragonite is uncommon and was confirmed with electron microprobe studies. Lack of microprobe data for paragonite was attributed to sampling bias and difficulty in locating suspect paragonite crystals suitable for analyses. The highest Na content in the first cation site in muscovite crystal structure amounts for 0.18 apfu in the current EPMA dataset. As such, white micas with Al-OH < 2200nm are referred to as "paragonitic".
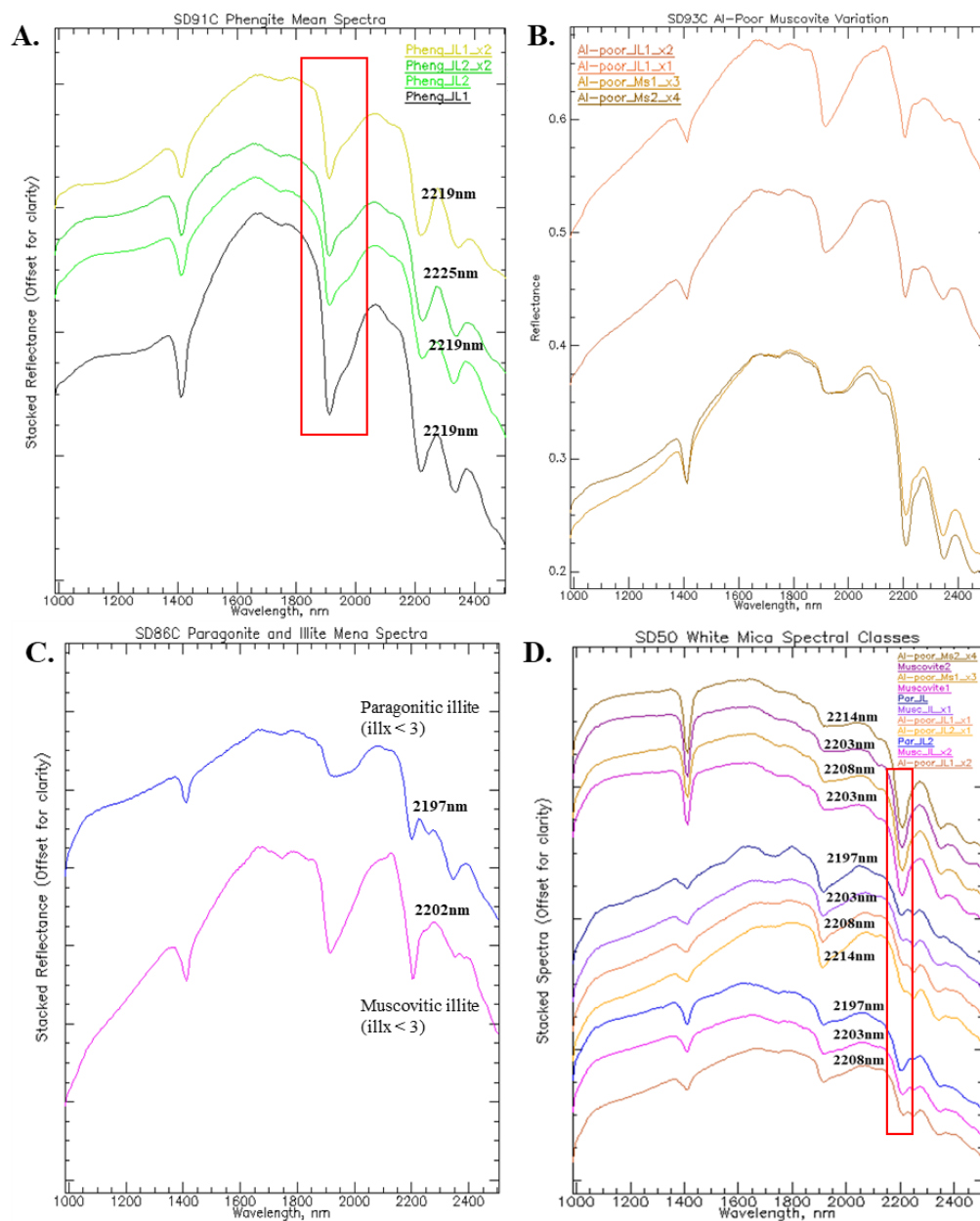
Figure 16. Spectral variation of Sadiola Hill white mica. **A**. Stacked reflectance of phengite and phengitic illites, note depths of OH and water feature at 1411nm and 1917nm (sample SD91). **B**. Vein-controlled Al-poor muscovite and illites assemblages with Al-OH feature at 2208nm, crystallinity increases veinward (sample SD93). **C**. Stacked spectra of paragonitic illite (2197nm) and muscovitic illite (2202nm) (sample SD86). **D**. Spectral variation of muscovite and illite at tonalite (top 4 spectra) greywacke contact (bottom 7 spectra). Note interference of biotite Fe-OH feature at 2247nm (sample SD50).

4.3.2   Carbonate Group

Carbonate group minerals were classified as calcite, dolomite, ferroan dolomite, and ankerite. Each mineral was separated into three sub-classes by Fe-drop values to assess for subtle mineralogical changes and possible mineral zonation (Figure 17, A). Calcites occurs within 1.0 - 1.3 range in Fe-drop. In the studied samples calcite carbonate feature shifted to shorter wavelength at 2337nm compared to calcite samples described in literature. This shift is consistent with minor Fe and substituting for Ca in calcite crystal structure (Mathieu et al., 2017). Ferrous drop of spectra, approaching medium values (> 1.3) in some vein-controlled calcite was also in agreement with observed spectral expression. Furthermore, presence of Fe in calcite was verified by the microprobe studies. Some calcite veins, for instance in sample SD048-SD93, contain water absorption feature at ~1900nm. This feature was explained by sub-micron fluid inclusions within calcite was verified with microscopy.

Dolomites show minor addition of Fe to the second cation site and occur over Fe-drop range of 1.0 - 1.3. The Fe proportion in dolomites was calculated in a range of 0.01-0.15 apfu based on electron microprobe results. Dolomite is distinguished from calcite by the position of the carbonate absorption feature. In the examined samples (e.g. SD048-SD90, SD129-SD68, SD22-SD45) carbonate feature was positioned at 2320nm. Dolomite in sample SD22-SD36 contains OH and water absorption features around 1400nm and 1900nm. These features were attributed to fine-grained white mica and fluid inclusions in coarse dolomite crystals.

Ferroan dolomites are characterized by medium-high to very-high Fe-drop values in carbonate spectra (1.3 - 1.5) corresponding to Fe content of 0.3-0.35 apfu in the second cation site. Position of carbonate feature in the examined ferroan dolomites dominantly occurs at 2320nm and shifts to 2326nm in rare instances (Figure 17, A and B).

Ankerite is a less abundant Fe-bearing carbonate in comparison to ferroan dolomite. The ankerite attains the highest Fe content in the crystal structure reaching 0.46 apfu. The mineral occurs over the Fe-drop range of 1.3 to $\geq$ 1.5 and is spectrally differentiated from ferroan dolomites by the carbonate absorption feature position. In the studied samples, e.g. SD048-92_02, CO_3^{2-} feature is centered at 2331nm (Figure 17, B).
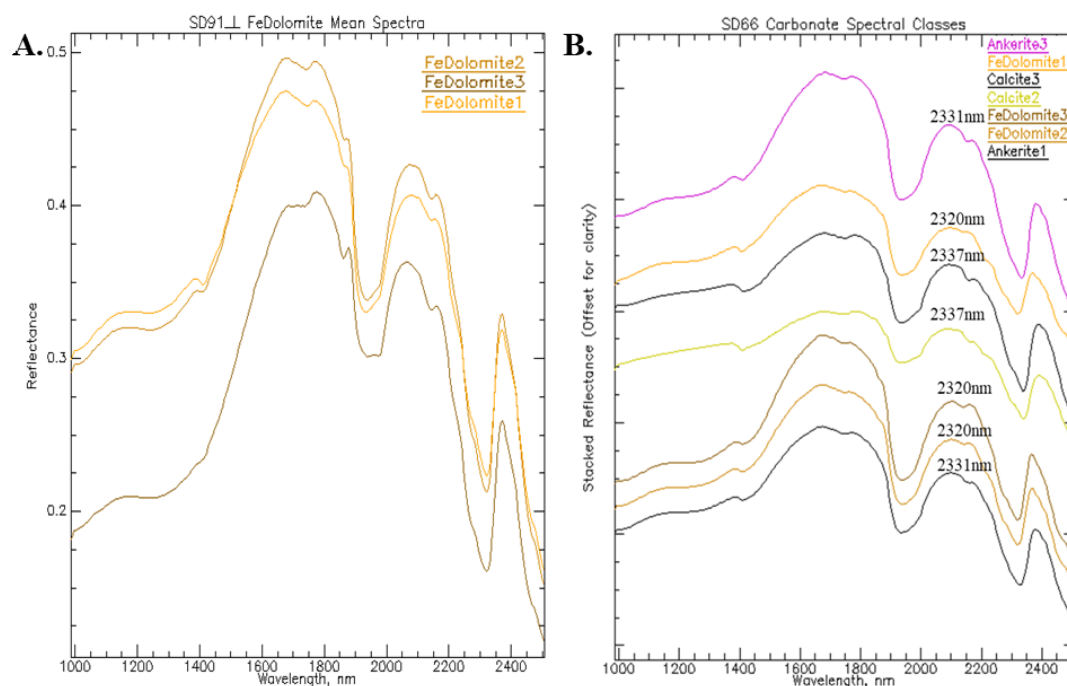
Figure 17. Spectral variation of Sadiola Hill carbonate group minerals. **A.** Ferroan dolomite subclasses separated by Fe drop. Note steepening of spectra in 1425-1600nm range (sample SD91). **B.** Stacked spectra of a complex vein of ferroan dolomite-ankerite transitioning into calcite (sample SD66).

4.3.3 Calcic Amphiboles

Actinolite-tremolite calcic amphiboles were examined in samples SD129-SD70 and SD042-SD88. Both amphiboles are characterized by the deepest absorption feature at 2314nm and the 2nd deepest feature at ~2388nm. The hydroxyl bond in the calcic amphibole samples is positioned at 1394nm. Intermediate Fe-Mg actinolite was separated from the Mg-endmember tremolite by a ferrous drop value of 1.1 (Figure 18, A).

4.3.4   Epidote

Two samples containing epidote (SD129-SD74 and SD129-SD75) were investigated during this project. Epidote in both samples is characterized by the diagnostic absorption feature at 2337nm and 2nd deepest absorption feature at 2253nm (Figure 18, A). A shallow feature diagnostic of epidote is centered at 1546nm. Additionally, an asymmetric water absorption feature is well-developed at 1905nm.

4.3.5   Chlorite

Two types of chlorite were recognized in the examined samples, both spectrally and with electron microprobe. The types are classified as Mg-rich chlorite approaching clinochlore composition, and an intermediate Mg-Fe chlorite. The Mg-rich chlorite is characterized by Mg-OH absorption feature positioned at 2332nm and the 2nd deepest Fe-OH feature at 2247nm (Figure 18, A). In the chlorite of intermediate composition these absorption features shift to 2337nm and 2253nm. The Fe-OH feature in both types of chlorite is deeper and more prominent than this feature in epidote, exceeding the depth value of 0.25.

4.3.6   Tourmaline

Tourmaline was encountered in two samples (SD119-SD57, and SD129-SD71). In both samples the doublet diagnostic of tourmaline is centered as 2208nm and 2242nm. An additional characteristic absorption feature, related to the B-OH bonds, is centred at 2354nm (Figure 18, B). Two other spectra shown in the Figure x demonstrate illite interferences with the tourmaline spectra, evident from development of OH feature at 1411nm and a wide water feature around ~ 1900nm. The tourmaline doublet is progressively muted as illite abundance increases.
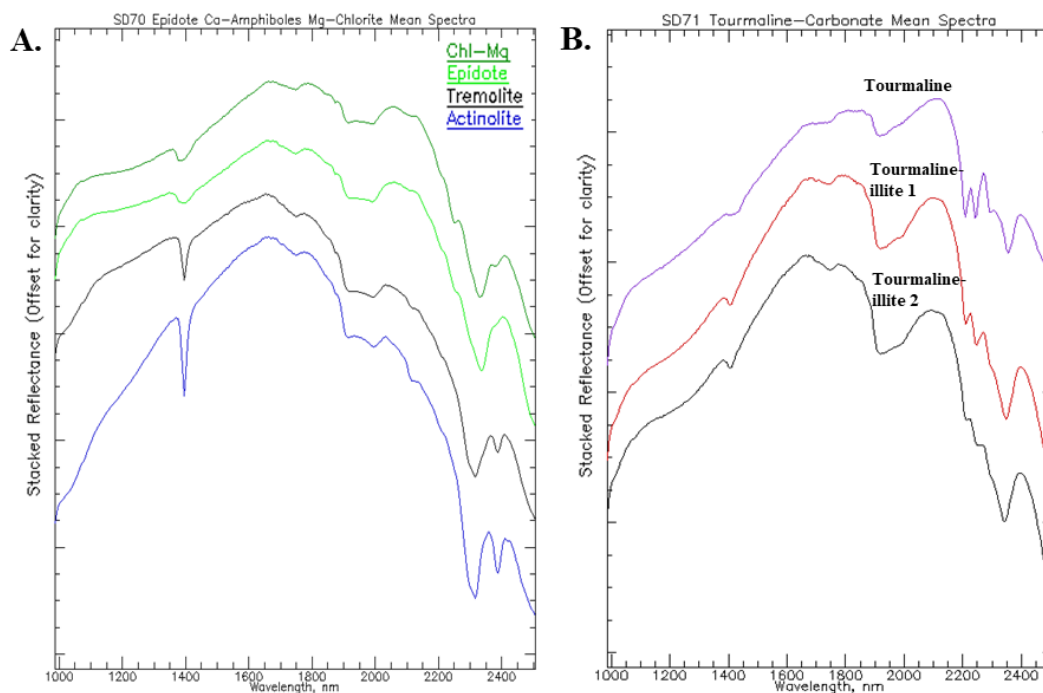
Figure 18. Spectral expression of Sadiola Hill chlorite, epidote, calcic amphiboles, and tourmaline. **A.** Stacked reflectance of Mg-rich chlorite, epidote, tremolite, and actinolite. Note steepening of the actinolite spectrum caused by Fe in the crystal structure (sample SD129-SD70). **B.** Stacked reflectance of tourmaline and unresolved tourmaline-illite mixtures (sample SD129-SD71).

4.3.7 Drill Hole SD782

SD782-SD33 Marble (223.5m)

SD33 represents a homogeneous fine-grained matrix of dolomite-calcite-quartz-feldspar-biotite crosscut by a 2cm wide carbonate-quartz vein. The carbonate within the matrix occurs in subhedral recrystallized crystals elongated in the direction of foliation. The dolomite within the vein is coarse-grained showing characteristic exsolution textures and sharp sutured boundaries. The carbonates have been classified as dolomite I, dolomite II, and calcite I amounting for 17%, 1.5%, and 14% respectively (Figure 19, A). Coarse-grained subhedral biotite occurs as accumulations and laminations sub-parallel to the vein and the overall texture. Quartz-feldspar fine-grained mosaic within the matrix is visually estimated at ~20%. This modal abundance is consistent with the percentage of unclassified pixels. Argillite laminae are absent in the sample, thus white mica is also absent. Finally, both the abundance (17%) and spatial distribution of aspectral pixels are consistent with the visual estimation of unaltered biotite abundance.

SD782-SD32A Marble (284.4m)

The sample consists of a network of recrystallized calcite-dolomite interbedded with thin biotite-carbonate-quartz laminae representing metamorphosed marl or carbonate bearing shale. Crystal edges of some biotite grains are partially replaced by traces of chlorite. Unclassified pixels (30%) are consistent with unaltered phlogopite and biotite abundances. Vein-controlled carbonate is medium-grained and do not show significant signs of deformation compared to the wall rock carbonate. The vein fill was classified as calcite I (14%), calcite II (5%), and dolomite I (10%) (Figure 19, B). Argillite laminae are difficult to recognize in the sample due to intense sulphidation that resulted in arsenopyrite-pyrrhotite-pyrite-chalcopyrite-gold mineralization (Figure 20, A). Within scarce laminae white mica occurs as Al-poor muscovitic illite. The sulphides represent 28% of the rock's volume based on visual estimates verified by aspectral pixel count.

SD782-SD30A Marble (308.2m)

This sample of marble contains abundant folded argillite layers interbedded with carbonate-dominant bands. The sample is strongly altered and well-mineralized in comparison to SD33 or SD28. The argillite consists of ~55% of fine-grained white mica-dolomite, ~30% of fine-grained recrystallized quartz and minor albite, ~10% relict medium-grained biotite, and ~5% sulphides represented by pyrite replaced by marcasite, arsenopyrite-pyrrhotite-sphalerite-chalcopyrite. Two fine-grained rounded free gold crystals were also identified in the argillite. White mica in the argillite consists of muscovitic illite (18%) and Al-poor illite 2205-2210nm (10.5%) with crystallinity values < 3. Lower crystallinity illite (<1) accounts for 7% of the sample (Figure 20, B). Metamorphosed carbonate-dominant layers consist of a recrystallized network of ~85% dolomite; 9% quartz; 5% biotite; and >1% of sulphides, occurring as discrete pyrite and pyrrhotite grains. Dolomite veins composed of medium- to coarse-grained dolomite I and II intergrowths crosscut the sample. The vein is folded and boudinaged with coarser sulphide blebs concentrated at intersections of boudins and with the argillite laminae. Overall, dolomite I and II make up 45% and 16% of the sample based on pixel count, with spectral signature of the carbonate vein-fill indistinguishable from the matrix carbonate (Figure 19, C).

SD782-SD28 Marble (315.1m)

SD28 is one of the least altered dolomitic-calcitic marble samples showing strong mineralogical band segregation between carbonate-dominant and argillite layers. Coarse-grained biotite porphyroblasts with quartz inclusions, attaining 4mm in length, are restricted to the argillaceous layers. The biotite is altered by traces of white mica on crystal boundaries and is relatively fresh otherwise. The white mica is restricted to the argillite laminae and is aligned with foliation in the sample. Traces of accessory apatite and rare arsenopyrite-pyrite-chalcopyrite also occur in the argillite. White mica in SD28 is spectrally variable and includes Al-poor illite I (14%), low crystallinity (< 3) muscovitic illite (13%), as well as Al-poor and muscovitic illites with the lowest crystallinity (< 1) representing 15% and 4% respectively (Figure 20, C). Carbonate-rich layers are composed of dolomite I, calcite I, and calcite II accounting for 20%, 23%, and 3% respectively (Figure 19, D). Fine-grained quartz and flaky biotite hin the carbonate layers account for ~5% in total based on visual estimates.

SD782-SD23 Tonalite (365.9m)

The meta-igneous matrix (75%) of sample SD782-SD23 consists of a fine-grained recrystallized quartz-feldspar. Equant quartz phenocrysts (~3%) up to 1mm in diameter show signs of low strain, as evident from onset of undulatory extinction, and minor recrystallization on grain boundaries. Plagioclase phenocrysts (~10%) have undergone partial recrystallization at crystal boundaries and are not sericitized. Biotite is nearly absent in the matrix and only occurs in reopened albite vein crosscutting the sample. Dolomite I and calcite I (2.8% and 1.5% respectively) occur as rare patches in the matrix, and as single hair-line veinlet.

One early quartz veinlet was observed in the sample. Although the vein has been folded and recrystallized, it is distinguishable from the quartz-feldspar matrix based on coarser crystal sizes. With exception of carbonate pixels, the sample is aspectral; as such its mineral map is not presented in this manuscript.

SD782-SD21 Tonalite - Marble Contact (407.0m)

Sample SD782-SD21 captures a contact of meta-igneous tonalite with the carbonate-rich component of the marble. Fine-grained recrystallized quartz-feldspar make up ~40% of the sample. Biotite (~15%) is strongly replaced by white mica and

dolomite II (2.5%) and III (1.5%) in irregular patches. Several biotite crystals are also replaced by Mg-Fe chlorite that was introduced later than the white mica. In this instance, biotite is completely consumed and is recognized as pseudomorphs. Accessory minerals include rutile, consistent with Ti liberated from replacement of biotite, and apatite. Very fine-grained white mica disseminated within recrystallized matrix, also occurs in clusters parallel to the foliation, probably in places where biotite was completely replaced. White mica in these clusters is Al-poor illite II (9%) with Al-OH shifted to 2210-2215nm. Other white mica assemblages in the sample include Al-poor illite I (38.8%) and muscovitic illite I (13.6%) with crystallinities < 3 (Figure 20, D). The marble consists of calcite I (31%), calcite II (59%), and dolomite I (7%) (Figure 19, E). Unclassified minerals in marble include 3% of fine-grained quartz, and up to 1% of fine-grained apatite Aspectral pixel count of 3% is consistent with coarse pyrrhotite-pyrite bleb and minor sulphide disseminations within the tonalite.

Drill Hole ID:
SD782

A. SD782-SD33

B. SD782-SD32

C. SD782-SD30

D. SD782-SD28

Carbonate Spectral Classes

Unclassified		Calcite I	
Dolomite I		Calcite II	
Dolomite II		Calcite III	
Dolomite III		Ankerite I	
Fe Dolomite I		Ankerite II	
Fe Dolomite II		Ankerite III	
Fe Dolomite III		Aspectral	

10mm

10mm

E. SD782-SD21
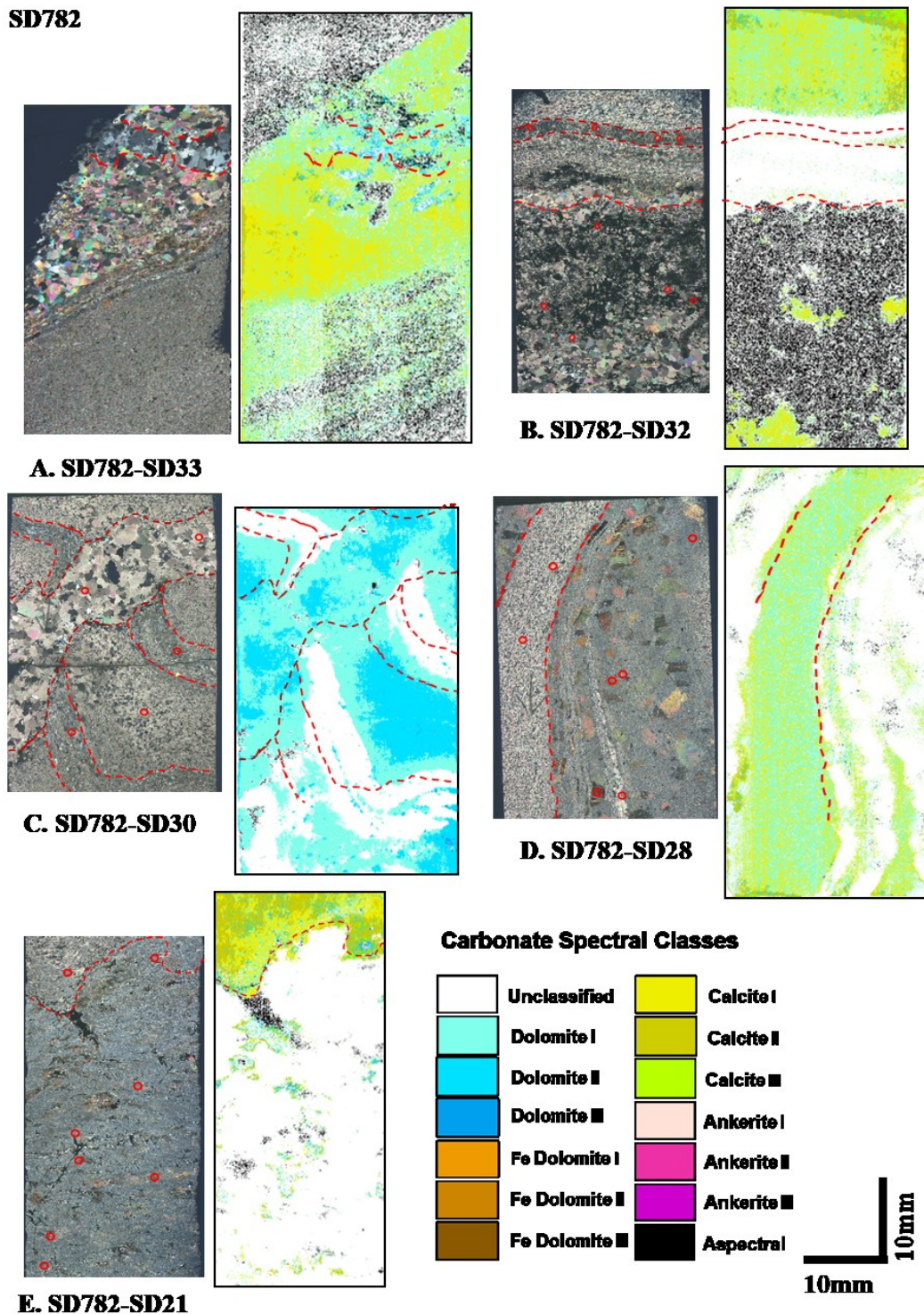
Figure 19. Drill hole SD782. Carbonate mineral maps at 26μm resolution with corresponding thin section scans under crossed polars. Red circles indicate locations of electron microprobe measurements. Dashed lines outline major landmarks used for qualitative analysis of thin section scans with corresponding mineral maps.
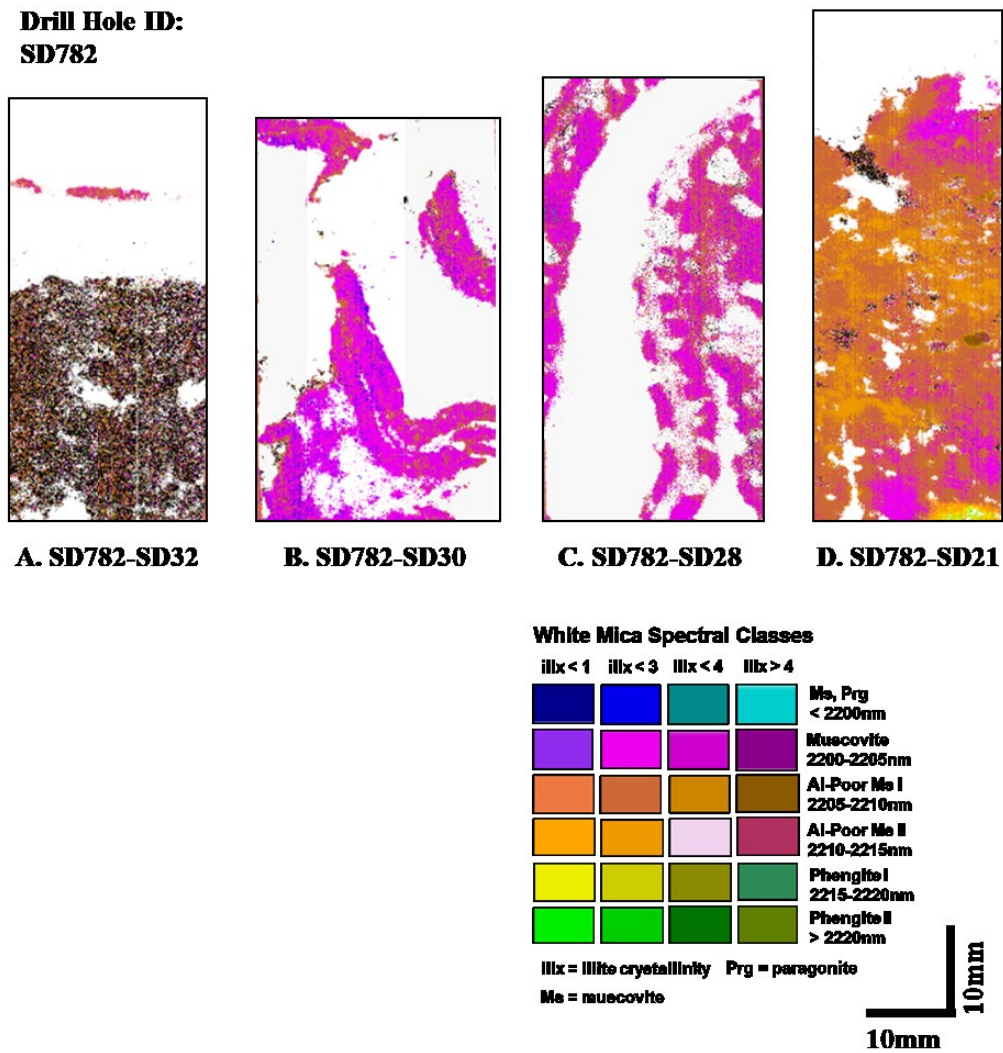
Figure 20. Drill hole SD782. White mica mineral maps at 26μm resolution.

4.3.8   Drill Hole SD22

SD22-SD50 Greywacke - Tonalite (185.7m)

Sample SD50 was collected at the tonalite-greywacke contact. The tonalite contains ~8% of equant quartz, and ~5% of relict feldspar porphyroclasts. Biotite (~5%) occurs as fine-grained flakes parallel to shear fabric. The quartz-feldspar matrix makes up ~80% of the sample. White mica in the sample is very fine-grained, oriented in the direction of shearing and replaces fine-grained feldspars within the matrix. The white mica was classified as muscovite II (10.6%), muscovite I (3.5%) with the highest

crystallinity indexes (> 4), and Al-poor muscovite I with crystallinity < 4 (4.7%). Tonalite is not well-mineralized with only traces of pyrrhotite and pyrite recognized.

The greywacke has a notably higher biotite content (~25%) and is less sheared than the tonalite. Quartz-feldspar matrix mosaic constitutes ~60% of the sample. Feldspars within the matrix are strongly sericitized. White mica in the greywacke occurs as illites, specifically muscovitic illite (5%), Al-poor illite I (26%), and Al-poor illite II (1.5%) with crystallinity values < 3. Illites I and II of the lowest crystallinity (< 1) also occur in the greywacke with calculated abundances of 5.7% and 1.4% respectively (Figure 22, A)

SD22-SD48 Greywacke (207.1m)

Sample SD22-SD48 consists of fine-grained quartz-feldspars mats (~40%), and ~35% of fine-grained foliation-parallel biotite flakes. Carbonate is a rare alteration phase occurring as hairline veinlets associated with 9% of low crystallinity Al-poor illite II, with Al-OH feature shifted to 2210-2215nm range (Figure 22, B). Biotite is completely replaced by the illite in wide halos of the white-mica-carbonate veins. The sample is sulphide-poor with only few fine grains of pyrite located within sericite-carbonate stringers and several grains grown over biotite in the matrix.

SD22-SD47 Greywacke (226.5m)

Biotite that is typical of the Sadiola greywacke is almost completely replaced by white mica in sample SD22-SD47. Carbonate was not recorded in the sample. Fine-grained white mica accounts for ~30% of the sample and is evenly distributed within the matrix. White mica occurs as four types of illite species Al-poor illite I (~20%) and muscovitic illite (~6%) of the second branch of illites, as well as Al-poor illite I (~3%) and Al-poor illite II of the first, lowest crystallinity, illite branch. Unclassified (13%) and aspectral pixels (6%) correspond to quartz vein and arsenopyrite-pyrite assemblages respectively (Figure 22, C).

SD22-SD46 Greywacke (300.0m)

Sample SD22-SD46 represents a typical greywacke unit crosscut by an early quartz vein. White mica in the metasedimentary matrix is intergrown with and replaces biotite, and defines a foliation that is often kink banded. Al-poor illite I (2205-2210nm) of both crystallinities is the dominant white mica species accounting for 4.8% of the first branch of illites, and 4.5% of the second branch of illites. Phengitic illites are not

as common and occur as accessory minerals (Figure 22, D). Phlogopite occurs as accumulations that are intergrown with pyrrhotite-pyrite-arsenopyrite. Carbonate alteration occurs as patches and disseminations of dolomite I (8.7%) and dolomite II (6.6%), often associated with phlogopite and the sulphides (Figure 21, A).

SD22-SD45 Marble (340.0m)

Sample SD22-SD45 is an argillite-rich impure marble unit. Argillite laminae are enriched in quartz-feldspar in comparison to other samples of the marble. The laminae consist of 35% of fine-grained recrystallized quartz-feldspar and 4% of white mica represented by equal amounts of phengitic illites of two lower crystallinities (Al-OH shifted to 2219nm) (Figure 22, E). Phlogopite accounts for 15% and is spatially associated with arsenopyrite-pyrrhotite-pyrite. Primary dolomitic matrix and carbonate alteration are difficult to distinguish in this sample. The overall carbonate abundance is estimated at 58% consisting solely of dolomite I (Figure 21, B). Dolomite crystals are medium-grained and often have irregular boundaries, indicating the prevalence of hydrothermal carbonate.

SD22-SD43 GWK (359.1m)

Sample SD22-SD43 was reclassified from marble to greywacke based on the high quartz-feldspar content (~40%) and textural features. A total of ~15% carbonate occurring as fine- to medium grained patches within the matrix is classified as dolomite II (7.3%), dolomite III (1.6%), ankerite I (1.5%), and calcite III (2.3%) (Figure 21, C). Medium-grained subhedral biotite (~20%), approaching phlogopite composition, is well-aligned defining the sample's foliation fabric. Sulphides (pyrrhotite-pyrite-arsenopyrite and minor chalcopyrite) are generally constrained to patches of carbonate-biotite in the matrix.

Very fine-grained white mica aggregates, classified as Al-poor illite II (2210-2215nm) crystallinity < 3 (11.5%) and Al-poor illite I (2205-2210nm) crystallinity < 1 (2%), are evenly distributed within the matrix, replacing pre-existing recrystallized feldspars with quartz remaining unaltered. Within the narrow halo of the vein biotite is replaced by fine-grained sericite, coarser than white mica in the matrix, with traces of rutile precipitated in response to the replacement. Vein-controlled white mica (8%) is a more aluminous (2200-2205nm) muscovitic illite with crystallinity < 3 (Figure 22, F).

SD22-SD42 GWK (374.75m)

Sample SD22-SD42 represents a semi-massive load of sulphides (~60% total) composed of 50% of pyrrhotite, 5% pyrite, 3% arenopyrite, and 2% chalcopyrite. All sulphides with exception of chalcopyrite are very course-grained and blebby in character. Gangue mineralogy includes quartz (~10%) either in fine-grained recrystallized masses or as coarse-grained equant strained grains. Biotite (~6%) in medium to coarse-grained subhedral crystals is closely associated with and replaced by sulphides. Chlorite (~2%) forms fine acicular crystal intergrowths with and replacing biotite. Carbonate (~22%) occurs as both vein-controlled and pervasive alteration products. Pervasive carbonate alteration was classified as dolomites I and II accounting for 4.8% and 4.5% respectively. Vein-hosted carbonate is more Fe-rich and occurrs as ferroan dolomite I (2%), ferroan dolomite II (2.5%), and ferroan dolomite III (2%) in the centre of the vein, and transitions to 1.5% of dolomite III in the vein margin (Figure 21, D).

SD22-SD41 GWK (375.9m)

Sample SD22-SD41 is a typical greywacke with quartz-feldspar-biotite matrix. Pervasive dolomite alteration occurs as fine- to medium grained patches and was classified as dolomite I (2.8%) and dolomite II (6.3%). The sample is also altered by peculiar coarse dolomite patches with quartz inclusions, resembling porphyroblasts, accounting for ~15% of the volume (Figure 21, E). This mode of dolomite occurrence was not seen elsewhere in the studied samples. It has been interpreted that the dolomite replaced plagioclase porphyroclasts with quartz emerging as replacement reaction product. Dolomite occurring as replacement patches is more Fe-rich than the pervasive dolomite, showing compositional ranges of dolomite II (4%) dolomite III (5.6%), ferroan dolomite I (2%), and ferroan dolomite II (1%) (Figure 21, E).

SD22-SD36 Dolomite Breccia (449.2m)

Sample SD22-SD36 represents a strongly carbonate-altered early diorite, evident from several 1-2mm completely recrystallized clasts, that underwent brecciation by a carbonic fluid. The matrix consists of dolomite I (62%) and dolomite II (10%) occurring as subhedral medium-grained patchy-interlocking crystals. Quartz-feldspar mats account for ~15%. Biotite is absent in this sample. Breccia fill is

composed of coarse-grained dolomite II (8%), dolomite III (3%), and ferroan dolomite I (2%). with fluid inclusion trails concordant to crystal growth patterns (Figure 21, F).
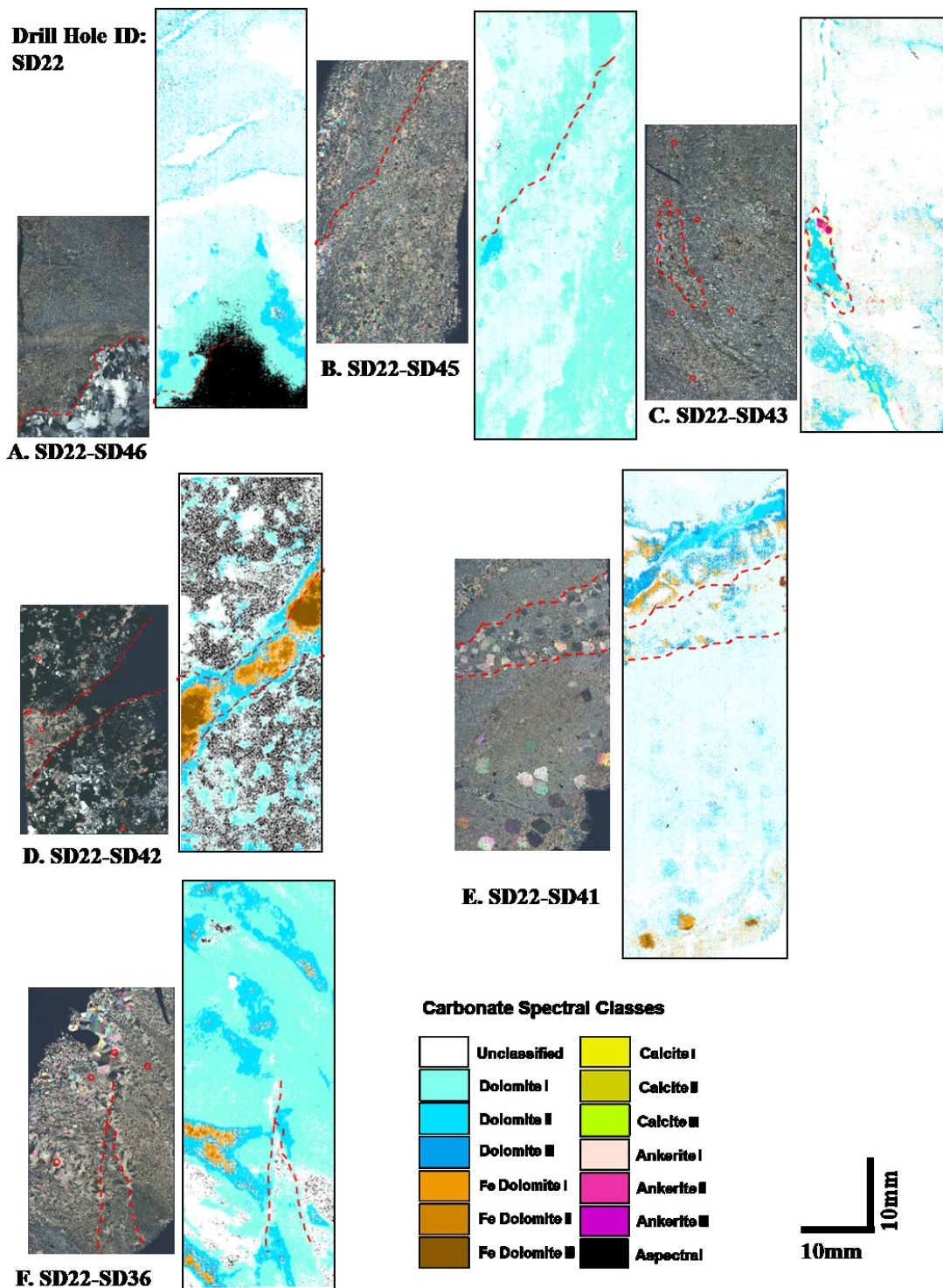
Figure 21. Drill hole SD22. Carbonate mineral maps at 26μm resolution with corresponding thin section scans under crossed polars. Red circles indicate locations of electron microprobe measurements. Dashed lines outline major landmarks used for qualitative analysis of thin section scans with corresponding mineral maps.
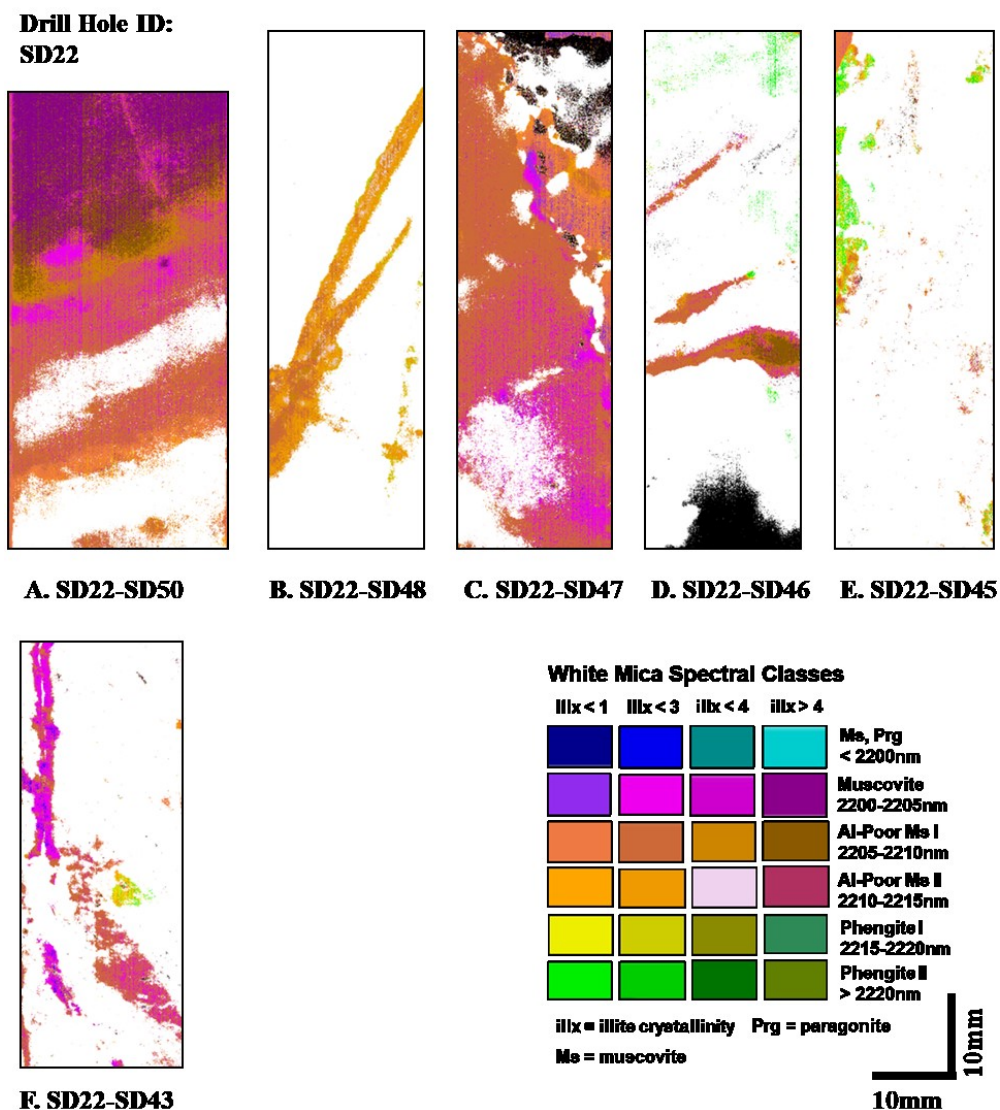
Figure 22. Drill hole SD22. White mica mineral maps at 26µm resolution.

4.3.9 Drill Hole SD119

SD119-SD57 Diorite (146.2m)

Sample SD57 represents a completely recrystallized diorite with only ~1% of relict plagioclase crystals remaining. The matrix consists of a very fine-grained recrystallized quartz-feldspar mosaic (~65%) with plagioclase crystals still showing polysynthetic twinning. Carbonate occurs as a pervasive alteration product in medium-grained irregular dolomite II (17%) and dolomite III (1%) that are evenly distributed within the matrix (Figure 23, A). Biotite (~15%) as medium-grained phase defines a weak foliation. Some accumulations of biotite are strongly replaced by Mg-rich

chlorite (7%). Tourmaline (8%) is present as fine-grained euhedral elongate prismatic crystals that are often intergrown with biotite (Figure 25, E).

SD119-SD62 Diorite (203.2m)

This sample of diorite has undergone almost complete recrystallization and grain size reduction. Relict medium-grained plagioclase accounts for < 5% of the sample with crystals undergoing development of subgrains and dolomite replacement. This sample is crosscut by a ~12mm thick Fe-dolomite vein consisting of very coarse-grained Fe-dolomite crystals with complex exsolution features. The vein fill is classified as ferroan dolomite II (28%), ferroan dolomite III (14%), and ferroan dolomite I (10%). Dolomite III (7.5%) and dolomite II (6.2%) occur as pervasive alteration within the matrix (Figure 23, B). Biotite is relatively rare in this sample, comprising 1-2% of its volume, and occurring as clusters with pyrrhotite-pyrite and dolomite. Mg-rich chlorite (~5%) occurs as a replacement product of biotite.

SD119-SD63 Diorite (231.3m)

The SD119-SD63 diorite has undergone partial recrystallization with ~15% of primary plagioclase still recognizable in the matrix. Sulphide makes up ~30% of the sample and is represented by pyrite>pyrrhotite>arsenopyrite. The associated alteration consists of dolomite II (12%), dolomite III (3%), and dolomite I (2.5%) and phlogopite (~20%) (Figure 23, D). Phlogopite is replaced by Mg-rich chlorite that represents 4% based on pixel count.

SD119-SD64 Diorite (250.7m)

Sample SD64 is a diorite with ~60% quartz-feldspar matrix that is altered by dolomite I (10.5%). Coarse-grained vein-controlled carbonate is classified as dolomite I (7%) transitioning veinward into dolomite II (5%). At a ~10^0 flexure in the vein, the dolomite infill changes to calcite I (9%) and calcite II (1.5%) (Figure 23, C). Coarse sphalerite and pyrite, partially replaced by marcasite, occur at the dolomite-calcite interface. Some of the dolomite-calcite crystals exhibit complex exsolution patterns or contain fluid inclusions. Examination of the wavelength maps confirmed that the vein-fill dolomites contain a water absorption feature at ~1900nm that gradually disappears as the vein fill changes to calcite. Biotite (~15%) occurs in subhedral medium to fine-grained bands and veinlets parallel to foliation. Traces of chloritized biotite also occur in the sample.

Drill Hole ID: SD119

A. SD119-SD57

B. SD119-SD62

C. SD119-SD64

D. SD119-SD63

Carbonate Spectral Classes

☐ Unclassified		☐ Calcite I	
☐ Dolomite I		☐ Calcite II	
☐ Dolomite II		☐ Calcite III	
☐ Dolomite III		☐ Ankerite I	
☐ Fe Dolomite I		☐ Ankerite II	
☐ Fe Dolomite II		☐ Ankerite III	
☐ Fe Dolomite III		☐ Aspectral	

10mm
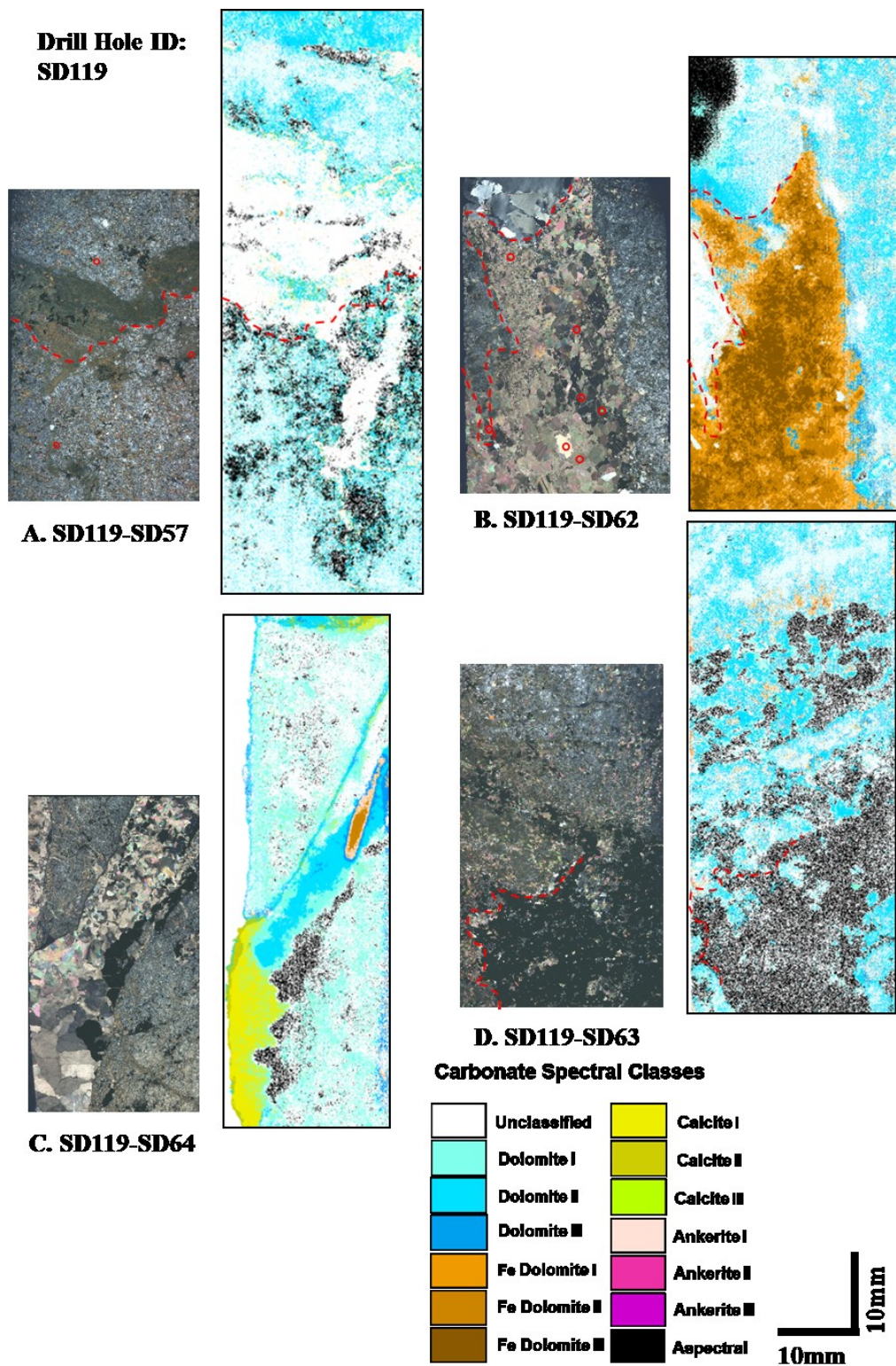
Figure 23. Drill hole SD119. Carbonate mineral maps at 26μm resolution with corresponding thin section scans under crossed polars. Red circles indicate locations of electron microprobe measurements. Dashed lines outline major landmarks used for qualitative analysis of thin section scans with corresponding mineral maps.

4.3.10 Drill Hole SD129

SD129-SD75 Diorite (251.5m)

Sample SD75 is a fine-grained recrystallized diorite with relict feldspars (~5%) partially recrystallized and altered to epidote. Epidote (15%) in fine-grained clusters is uniformly distributed throughout the rock. The sample is crosscut by a 1cm-wide carbonate vein classified as dolomite I (8.4%) and dolomite II (2.5%) (Figure 24, A). The vein-fill is deformed, as evidenced from deformation of the exsolution lamellae. Intermediate Mg-Fe chlorite comprising 5% of the volume and originates as a replacement product of biotite (Figure 25, A).

SD129-SD74 Marble (304.3m)

Sample SD74 is marble collected near a contact with the early diorite intrusion. Primary mineralogy of the marble is almost completely replaced by skarn assemblages. Relict dolomite-quartz amount for 15% and 5% respectively, occur in clusters with epidote. The dolomite was classified as dolomite I. Epidote (72%) and minor clinozoisite (1%) occur in medium-grained subhedral crystal clusters that are heavily stained by iron oxide (Figure 25, B). Minor actinolite amounts for 6% of the sample. Sparse chlorite occurring in the sample is classified as Mg-rich chlorite (1.3%).

SD129-SD71 Greywacke (312.9m)

Sample SD71 is a quartz-tourmaline-carbonate vein crosscutting greywacke. The vein infill is estimated at 20% quartz, 18% tourmaline (Figure 25, C). Carbonate is a minor alteration phase occurring interstitially to tourmaline. A fine-grained quartz-feldspar-biotite matrix represents ~30% of the sample. White mica altering fine-grained metasedimentary matrix is classified as phengitic illite II (19.5%) and phengitic illite I (1.6%). Intermediate chlorite replacing biotite accounts for 4% of the volume.

SD129-SD70A Marble (339.1m)

SD70 is a marble crosscut by a ~3cm wide quartz vein that underwent subsequent deformation. The quartz vein is crosscut and by dolomite-biotite-white mica vein. Arsenopyrite is associated with the latter assemblage. Matrix of the marble consists of dolomite I (38.5%) and dolomite II (6.5%) occurring as medium-grained recrystallized carbonate mixture (Figure 6, B). Actinolite (3%), tremolite (1.5%), Mg-

rich chlorite (10.8%), and minor epidote (1%) occur near quartz vein- wall rock contact (Figure 25, D).

SD129-SD69B Marble (352.0m)

SD69 shows common textural and mineralogical features of the marble. Folded argillite laminae consist of white mica, 15% fine-grained carbonate (~15%); recrystallized quartz (~10%); and relict biotite (~10%) strongly replaced by white mica. White mica was classified as illite I (13%), illite II (4%), and phengitic illite (2%) of the second illite branch (Figure 10, C). Carbonate matrix consists of dolomite I (45.6%) and calcite I (25%) medium-grained mixture (Figure 24, C). Quartz (~10%) mostly fine-grained recrystallized evenly distributed within the matrix. Biotite (~10%) within carbonate-rich layers of the marble occurs as subhedral flakes parallel to foliation. Sulphides (~2%) (arsenopyrite > pyrite > pyrrhotite > sphalerite) are mostly restricted to the argillite laminae.

SD129-SD68 Marble (358.3m)

SD68 is a carbonate-dominant marble sample with argillite laminae absent. Dolomite-calcite subhedral medium grained interlocking patches (75%) quartz-feldspar fine-grained equant crystals (~20%), subhedral fine-grained biotite (~3%). Matrix is crosscut by a 1cm wide carbonate vein classified as dolomite II. Dolomite within the vein is coarse-grained showing characteristic of the deposit exsolution textures and sharp sutured boundaries. Minor medium-grained subhedral biotite occurs parallel to the vein near the vein walls. Carbonate assemblages of the sample were classified as dolomite I (20%), dolomite II (71%), dolomite III (5%) (Figure 24, D). The rock is poorly mineralized with only a few grains of pyrite-arsenopyrite spotted in the matrix.

SD129-SD66 Diorite (474.7m)

SD66 is an early diorite sample that undergone almost complete recrystallization and grain size reduction. The sample is crosscut by a folded ~15mm wide carbonate vein. The vein is characterized by a complex carbonate mineralogy manifested petrographically by exsolution patterns, sporadic distribution of fluid inclusions, and polyphase crystal growth. SWIR hyperspectral classification revealed the vein is composed of ferroan dolomites I (5.2%), II (12%), and III (29.4%) that transform into calcite I (1.5%), calcite II (16.9%) and calcite III (11.6%). Additionally,

3% of ankerite occur at the Fe-dolomite-calcite boundary (Figure 24, E). Similar sharp changes in carbonate mineralogy within were also observed in the sample SD119-SD64. Pervasive carbonate alteration was classified as dolomite II (5.3%) and dolomite III (3.7%). Fine-grained arsenopyrite is restricted to vein walls.
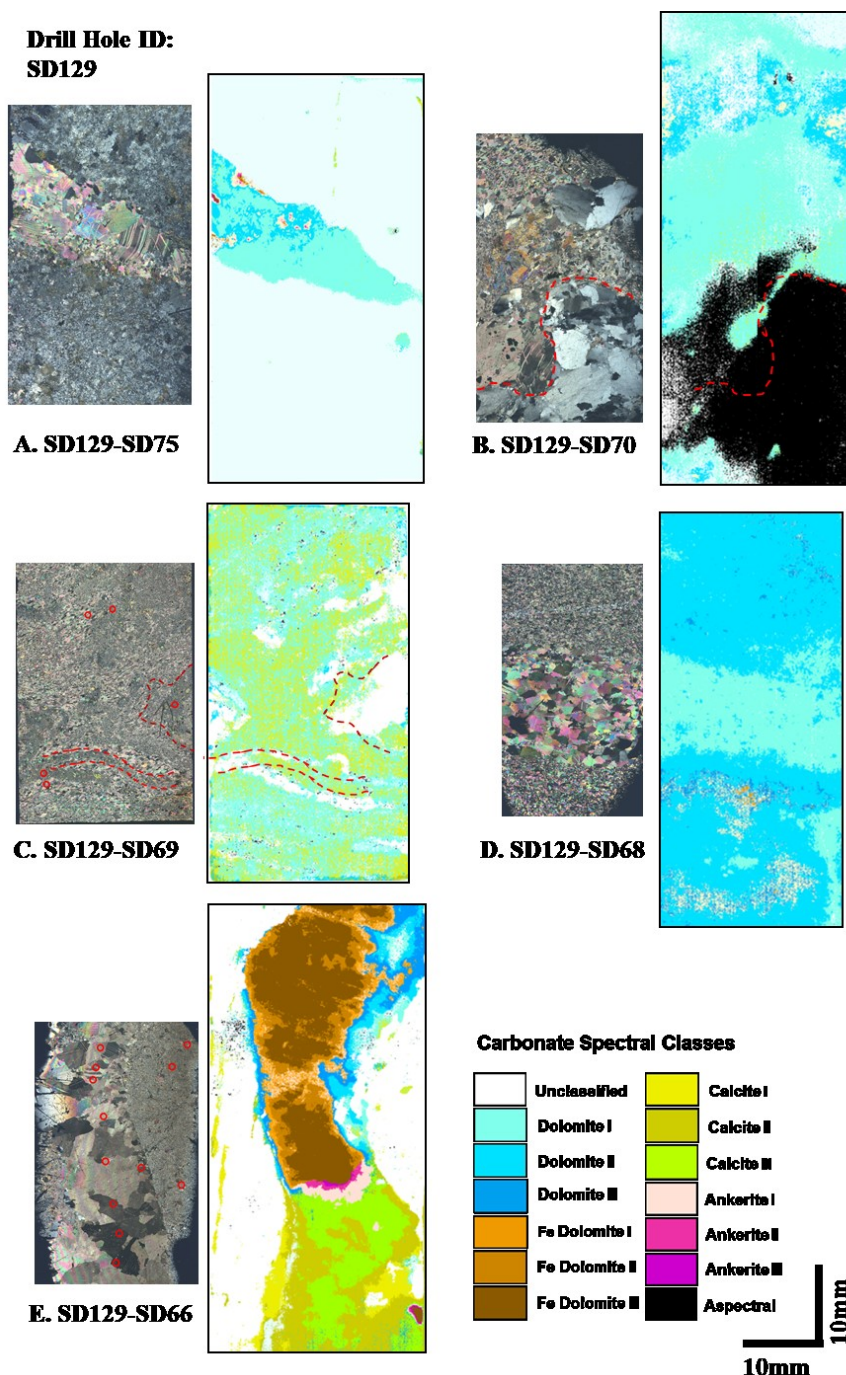
Figure 24. Drill hole SD129. Carbonate mineral maps at 26µm resolution with corresponding thin section scans under crossed polars. Red circles indicate locations of electron microprobe measurements. Dashed lines outline major landmarks used for qualitative analysis of thin section scans with corresponding mineral maps.

A. SD129-SD75

B. SD129-SD74

C. SD129-SD71

D. SD129-SD70

E. SD119-SD57

F. SD042-SD88

Classification of Chlorite, Amphiboles, Epidote, and Tourmaline

- Chlorite Fe
- Chlorite Fe > Mg
- Chlorite Mg > Fe
- Chlorite Mg
- Epidote
- Clinozoisite
- Actinolite
- Tremolite
- Tourmaline
- Carbonate
- White Mica
- Unclassified

10mm

10mm
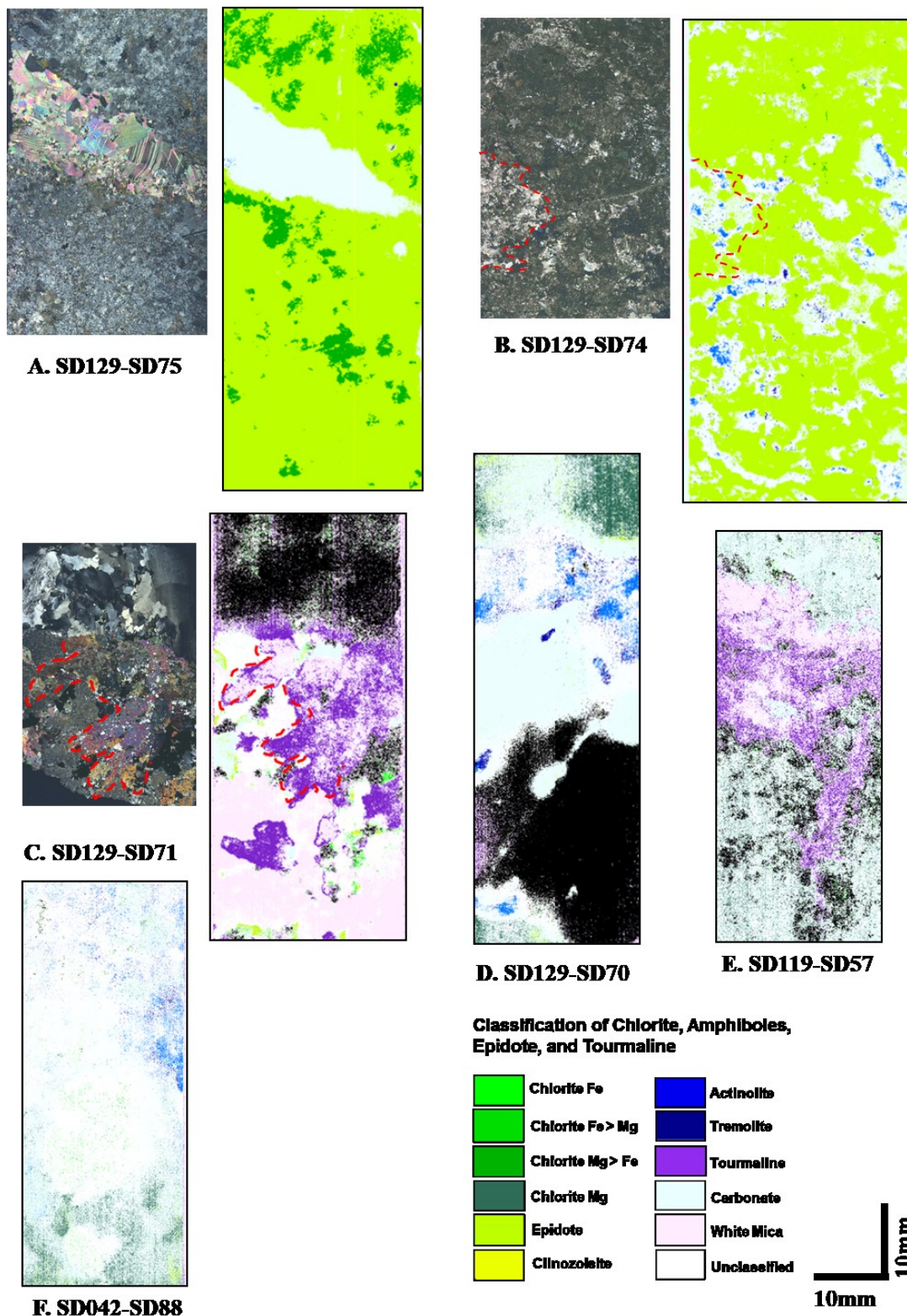
Figure 25. Drill holes SD042, SD119, and SD129. Mineral maps of chlorite, amphiboles, epidote, and tourmaline at 26μm resolution with corresponding thin section scans under crossed polars. Red circles indicate locations of electron microprobe measurements. Dashed lines outline major landmarks used for qualitative analysis of thin section scans with corresponding mineral maps.

4.3.11 Drill Hole SD042

SD042-SD83 Greywacke (102.8m)

SD83 is a biotite-rich (~40%) and carbonate altered greywacke. Dolomite I (5%) is in fine-grained crystals often occurring with fine-grained white mica on crystal margins. White mica occurs as Al-poor illite II (4.1%) zoning veinward into Al-poor muscovite II (3.8%), with Al-OH feature shifted to 2213nm in both instances (Figure 28, A). The white mica assemblages form wide halos to dolomite-muscovite veinlets, with biotite getting completely replaced by the illite in the vein halos.

SD042-SD85 Diorite (163.9m)

SD85 is a partially recrystallized early diorite sample with ~35% of plagioclase and ~4% quartz remaining. Biotite (~30%) intensity and grain size increase towards one side of a carbonate vein, indicating asymmetric reopening of earlier biotite vein followed by carbonate fracture-fill. Ferroan dolomite is restricted to veining and consists of Fe-dolomite I (4.6%), Fe-dolomite II (3.4%), and Fe-dolomite III (1%). These assemblages transition into dolomite III accounting for 5.2%. Pervasive carbonate alteration is dominated by dolomites I (2%) and II (8.5%) (Figure 26, A).

SD042-SD86 Diorite (178.0m)

SD85 is a well-preserved diorite sample with ~45% of primary plagioclase, ~5% K-feldspar, and ~3% of quartz recognizable. All primary ferromagnesian minerals have been consumed and replaced by alteration. Paragonitic illite II (2.8%) and muscovitic illite (1%) occur as a vein-controlled alteration with Al-OH absorption feature positions at 2197nm and 2202nm respectively (Figure 28, B). Vein-controlled carbonate occurs as ferroan dolomite III (8%). Pervasive carbonate alteration evenly disseminated within the meta-igneous matrix in places replacing plagioclase is represented by dolomites I (10%) and II (12.5%) (Figure 26, B).

SD042-SD88 Conglomerate (207.0m)

SD88 is represents a matrix-supported coarse sand to pebble conglomerate with clasts of unknown origin metamorphosed to tremolite-actinolite-chlorite-carbonate aggregates. The sample is heterolithic with primary mineralogy of clasts strongly influencing final alteration assemblages. The calcic amphiboles occur in fine-grained anhedral to subhedral radiating crystals. The amphiboles were classified as

actinolite (8%) and tremolite (10%) with modal abundances derived from petrographic observations. Mg-rich chlorite (10%) occurs in anhedral masses interstitial to actinolite (Figure 25, F). Additionally, 1.5% of epidote occurs in the sample. Relic fine-grained quartz-feldspar and biotite make up the remaining clast volume. Carbonate occurs in the sample in three dolomite spectral classes: dolomite I (17.8%) and dolomite II (18.4%), and dolomite III (1.2%) (Figure 26, C).
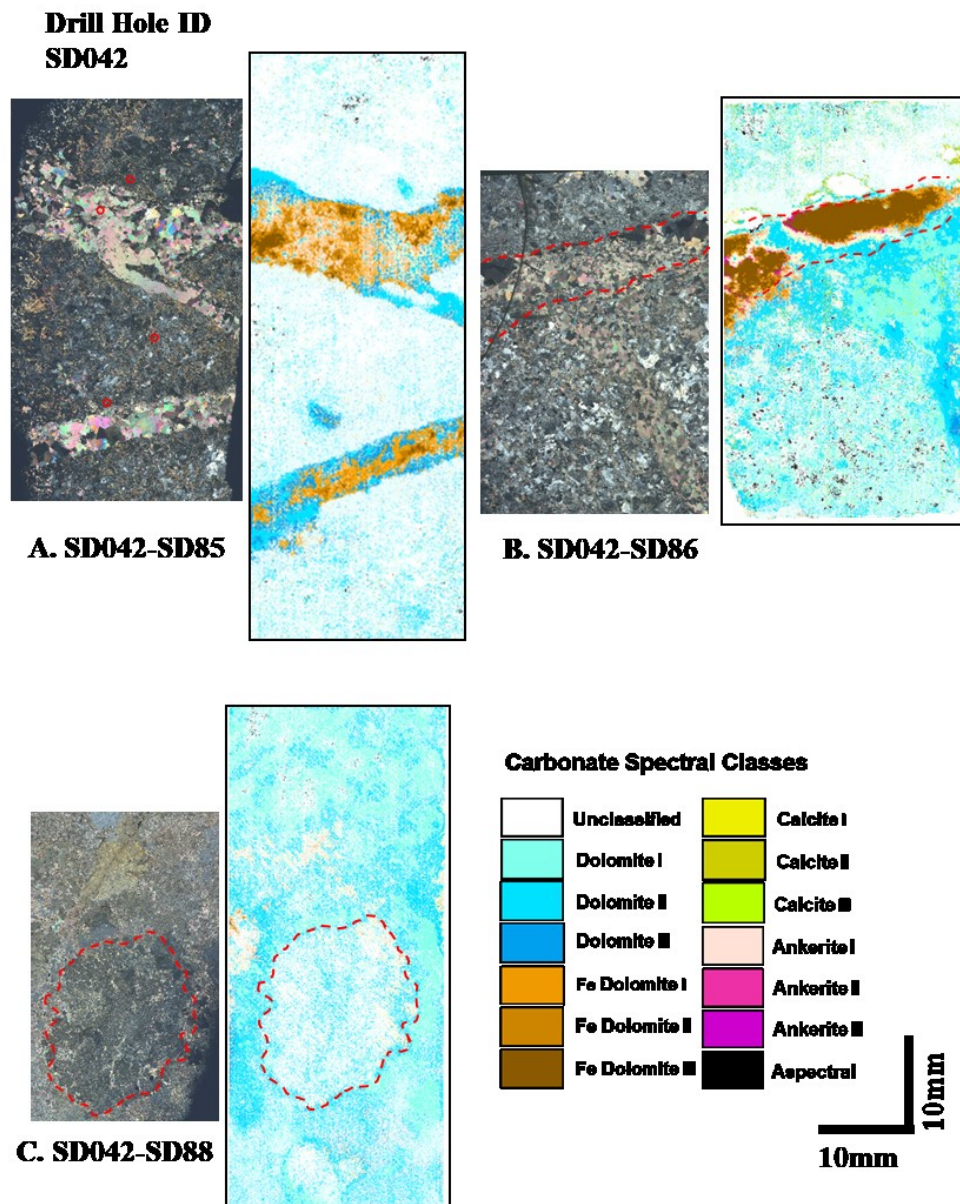
Figure 26. Drill hole SD042. Carbonate mineral maps at 26μm resolution with corresponding thin section scans under crossed polars. Red circles indicate locations of electron microprobe measurements. Dashed lines outline major landmarks used for qualitative analysis of thin section scans with corresponding mineral maps.

4.3.12 Drill Hole SD048

SD048-SD93 Diorite (94.1m)

SD93 was originally logged as greywacke but has been reclassified as strongly recrystallized diorite during this study. The sample with matrix comprised of fine-grained recrystallized quartz (~20%), plagioclase (~15%) often with polysynthetic twinning preserved and minor K-feldspar (~3%). Pervasive dolomite also occurs in the sample as dolomite II (10%) and dolomite III (11%) . White mica veinlets occurring in the sample were classified as Al-poor muscovites (2205-2210nm) occurring over 3 ranges of crystallinities zoned into the vein, with the highest crystallinity (> 4) within the centre of the vein (Figure 28, D). Late calcite vein crosscuts and offsets the Fe-dolomite patches and muscovite veinlets. The calcite has been classified as calcite III (3%) and calcite II (1%).

SD048-SD92_01 Greywacke (119m)

The sample represents an albitized greywacke containing several pebble-size metaigneous clasts in contact with strong carbonate flooding. The carbonate is medium-grained and has been recrystallized based on triple junctions between crystals. It has been classified as dolomite II (14.5%), dolomite III (5.6%), and dolomite I (4.2%) (Figure 27, A). Dolomite and biotite veinlets crosscut the albitized matrix wrapping around the clasts. Biotite in veinlets is euhedral to subhedral, not showing signs of alignment and is reopened by dolomite I in several instances.

SD048_SD92_02 Greywacke (119.1m)

Similar albitized greywacke as SD92_01 crosscut by a multi-generation carbonate vein. Core of the vein composed of Fe-rich carbonate assemblages including: ferroan dolomite II (2%), ferroan dolomite III (4.7%), ferroan dolomite I (1%), intergrown with the three spectrally identified classes of ankerite ranging from 2.5% - 5% in abundance. Fe-bearing carbonate assemblages contain fluid inclusions. Carbonate mineralogy changes towards vein margins to calcite I through III ranging in abundances from 2% to 3.6%. The calcite assemblages are inclusion-free and post-date the Fe-bearing carbonate assemblages evident from fracture-fill emplacement style and local microbreccias. Fe-dolomite-ankerite vein cross-crosscuts and partially reopens irregular biotite veinlets. Minor pervasive carbonate within matrix was

classified as dolomite I (8%), dolomite II (8%), and dolomite III (3.6%) assemblages (Figure 27, B)

SD048-SD91 Greywacke (166.3m)

Greywacke weakly foliated matrix comprised of fine-grained recrystallized quartz-feldspar (~60%), biotite (~30%), and carbonate (~10%), biotite is partially replaced by sericite (3:2 ratio) on crystal margins. The sample is crosscut by a carbonate vein classified as ferroan dolomite III (19%), ferroan dolomite II (8%), and ferroan dolomite I (4%) (Figure 27, C). Fine-grained sericite reopens the Fe-dolomite vein resulting in local micro-brecciation textures. This late sericite is compositionally Mg-rich, approaching ideal phengite composition on both illite branches. Abundances of specific spectral classes were the following: phengitic illite I and phengitic illite II of both crystallinity branches representing 15% based on pixel count. White mica within the matrix and replacing biotite was classified as Al-poor illites I (10%) and II (8%) with crystallinity < 3 (Figure 28, E). Carbonate within greywacke matrix occurs as dolomite I (1.8%) and dolomite II (3.5%)

SD048-SD90 Marble (169.1m)

White mica comprising argillite was classified as Al-poor illite II (2%) and illite I (3%), as well as phengitic illite (1%) of low crystallinity (Figure 28, F). Matrix consists of dolomite I (67%) in medium to coarse-grained beige carbonate with dark (but not opaque) inclusions, partly recrystallized based on sutured crystal boundaries, but has not undergone grain size reduction (Figure 27, D). Biotite (~10%) within the matrix occurs as medium-grained subhedral tabular crystals not showing preferred orientation. The sample is well-mineralized with sulphides in the argillite laminae reaching ~1.5%. The sulphides consist of pyrite replaced by marcasite, arsenopyrite, sphalerite, and chalcopyrite.

Drill Hole ID:
SD048

A. SD048-SD92_01

B. SD048-SD92_02

C. SD048-SD91

D. SD048-SD90

Carbonate Spectral Classes

Unclassified	Calcite I	
Dolomite I	Calcite II	
Dolomite II	Calcite III	
Dolomite III	Ankerite I	
Fe Dolomite I	Ankerite II	
Fe Dolomite II	Ankerite III	
Fe Dolomite III	Aspectral	

10mm

10mm
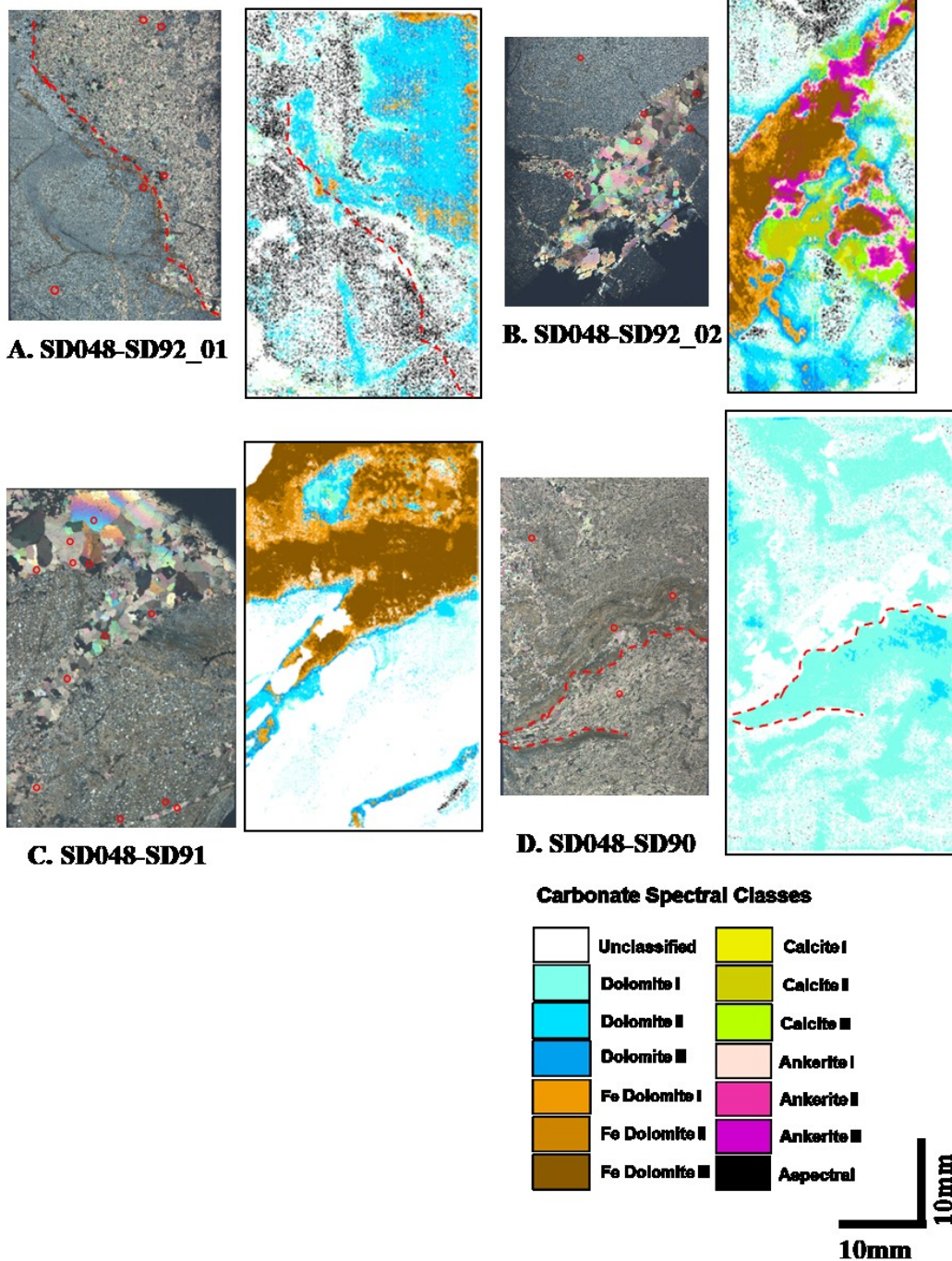
Figure 27. Drill hole SD048. Carbonate mineral maps at 26μm resolution with corresponding thin section scans under crossed polars. Red circles indicate locations of electron microprobe measurements. Dashed lines outline major landmarks used for qualitative analysis of thin section scans with corresponding mineral maps.

Drill Hole ID:
SD042

Drill Hole ID:
SD129

A. SD042-SD83

B. SD042-SD86

C. SD129-SD69

Drill Hole ID:
SD048

D. SD048-SD93

E. SD048-SD91

F. SD048-SD90

White Mica Spectral Classes

Ilx < 1   Ilx < 3   Ilx < 4   Ilx > 4

Me, Prg < 2200nm

Muscovite 2200-2205nm

Al-Poor Ms I 2205-2210nm

Al-Poor Ms II 2210-2215nm

Phengite I 2215-2220nm

Phengite II > 2220nm

Ilx = illite crystallinity   Prg = paragonite
Me = muscovite

10mm
10mm
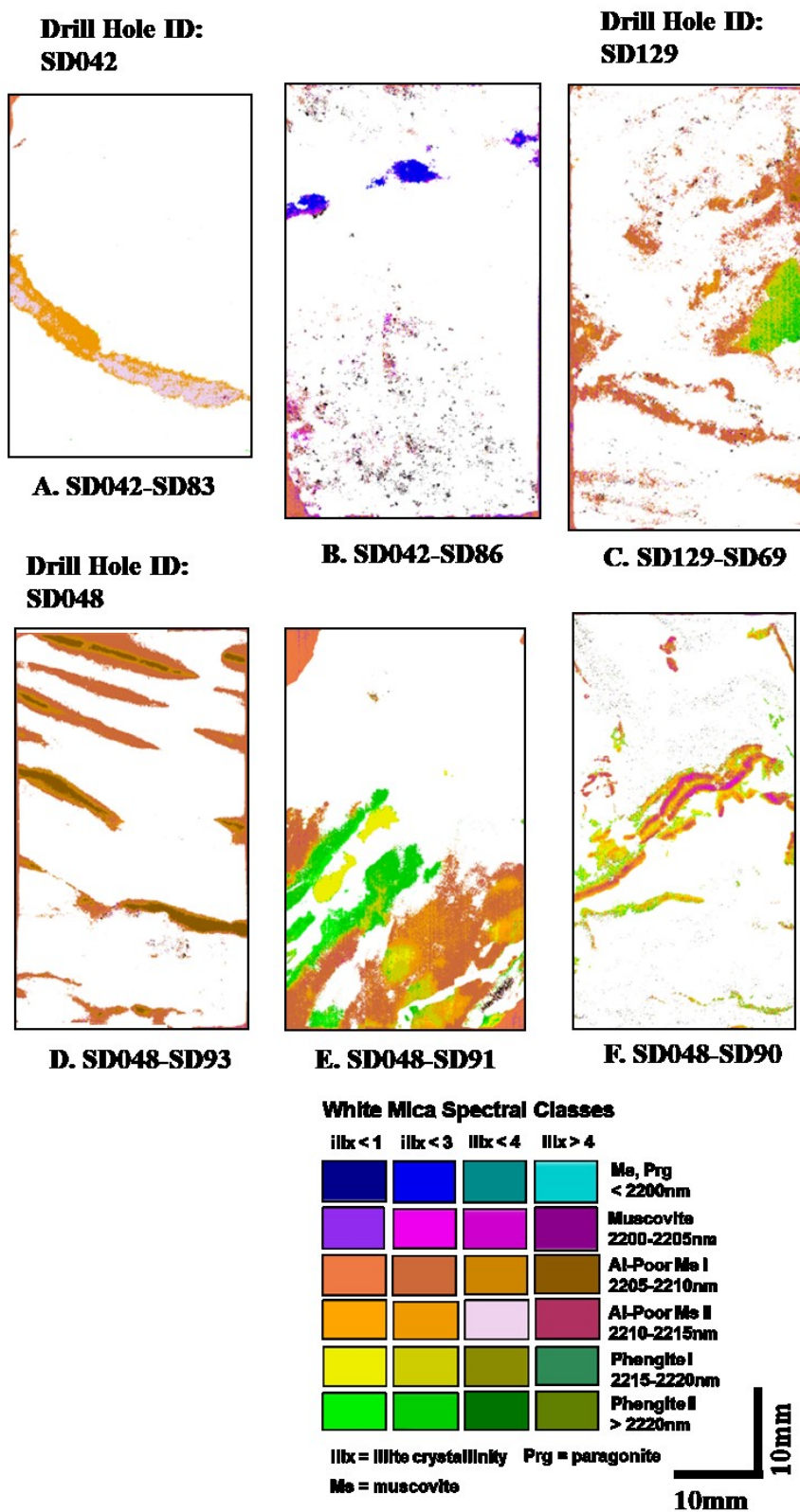
Figure 28. White mica mineral maps at 26µm resolution from drill holes SD042, SD048, and SD129.

4.4   Geochemistry

Geochemical sampling of the Sadiola Hill drill core was conducted to define trace and pathfinder element associated with gold, and to characterize significant host-rocks occurring within the Sadiola goldfield. The data was also used to further evaluate systematic changes in hydrothermal alteration proximal and distal to the ore zone.

4.4.1   Rock Classification

Igneous rocks intersected in drill holes SD119, SD129, and SD22 were classified with Al_2O_3/TiO_2 ratios. Titanium and aluminium have reverse relationship, with the former being progressively depleted with fractional crystallization, and the latter becoming enriched. Both Al and Ti are immobile elements that are generally unaffected by hydrothermal alteration or low to intermediate grade metamorphism (Winchester and Floyd, 1977). Abundances of these elements will change depending on the alteration type causing mass losses or gains. The ratio, on the other hand, will remain unchanged (Large et al., 2001).

Early diorite is characterized by average Al_2O_3/TiO_2 ratios of 26.2. Al_2O_3/TiO_2 ratio in tonalite, based on one sample (SD782-SD21), was 41. Sample SD119-SD57, classified as diorite petrographically based on mineralogical and textural features, has unusually low Al_2O_3/TiO_2 ratio of 13.4. The discrepancy is caused by anomalously high TiO_2 content in the sample, exceeding an average TiO_2 in diorite by 0.68 weight %, while the Al content remained in the range typical for Sadiola diorite. This sudden spike in Ti is attributed to a local increase in tourmaline-biotite expressed as a coarse irregular patch ~10mm wide, that probably concentrated Ti in the sample. Consequently, sample SD119-SD57 can be considered a poor-quality sample, thus not having any statistical significance over the diorite sample population.

When completely recrystallized and strongly biotite altered primary textures of the early diorite and the greywacke are getting obscured. The best way to distinguish these two rock types chemically is by SiO_2/Al_2O_3 weight % ratios. Since the early quartz veins were not sampled, Si content in the rock approximates detrital quartz content in the greywacke or primary igneous quartz in the diorite. The greywacke average SiO_2/Al_2O_3 ratio is 4.8, while the diorite averages 3.2.

Interlayered dolomitic-calcitic marble- argillite has a significantly lower Si content, averaging at 25.1 SiO_2 weight %, compared to 57 SiO_2 weight % in the greywacke. The Si content may vary between samples depending on abundance of argillite laminae. Additionally, the primary calcite-dolomite composition of the marble is consistent with high CO_2. Based on the Si content the marble may be referred to as "siliceous marble", However, for the purpose of maintaining consistent terminology with the previous studies, in this manuscript the country rock is referred to as "dolomitic-calcitic marble" or "impure carbonate unit".

4.4.2   Alteration Assemblages

Current studies determined that K/Al molar and Mg/Al molar ratios are best predictors of gold grade at Sadiola Hill. K/Al ratio in poor-mineralized marble samples amounts for 0.14. Samples collected from the marble containing high gold content attain K/Al values of 0.55-0.76. Mg/Al ratio shows a pattern very similar to the K/Al ratio. The low-grade samples with background Mg/Al values range from 0.28-0.35, regardless of lithology. In well-mineralized marble samples Mg/Al reaches values of ~3. Greywacke and diorite with low to sub-economic gold grades are not significantly enriched in K and Mg beyond barren rock values. This can be explained by lower intensities of white mica alteration, and general lower gold content of these rocks leading to sampling bias. Overall, enrichments in K and Mg relative to immobile Al are consistent with hydrothermal introduction of Al-poor to phengitic muscovite and illite, and Fe-bearing dolomites altering the impure marble.

Addition of CO_2, estimated by total carbon in geochemical data, is a reliable way of estimating carbonate alteration intensities cogenetic to gold mineralization in the greywacke and diorite. It has been determined with reflectance spectroscopy studies and petrographic observations that carbonate alteration is dominated by Fe-bearing dolomites cogenetic to gold. Post-ore calcite is a volumetrically minor mineral phase at Sadiola; hence its contribution to the overall CO_2 addition is negligible. In the diorite, samples with total C > 1.5% correlate well with the gold content. Total carbon exceeding 2% correlates with gold in the greywacke. Although the marble also underwent CO_2-addition during ore-stage hydrothermal alteration, it is difficult to quantify amount of C added by the fluid due to primary carbonate assemblages making

up the rock. Furthermore, the thickness of carbonate-dominant layers within the marble may vary affecting the total C content.

Based on studies and petrographic observations from the current study, early pre-ore alteration assemblages are characterized by addition of Si, expressed as quartz veining. Since silica addition is not directly related to the gold event, samples containing quartz veins were not submitted for geochemical analyses to avoid dilution of pathfinder elements. Pervasive albitization is expected as Na enrichment; it was not assessed due to paragenetic constrains to the pre-ore stage.

Globally the trace element distribution reported in gold deposits by Goldfarb and Groves (2015) was consistent with the observed mineralogical composition of the host rocks (Figure 29). Both barium and strontium are enriched, consistent with pervasive albitization, however these elements do not correlate with gold. Enrichment in rubidium, lithium, and elevated levels of cesium are constituent with K-metasomatism manifested by muscovite-phlogopite and minor K-feldspar. Thallium is generally at background levels reflecting paucity of pyrite and dominance of arsenopyrite and pyrrhotite at Sadiola.
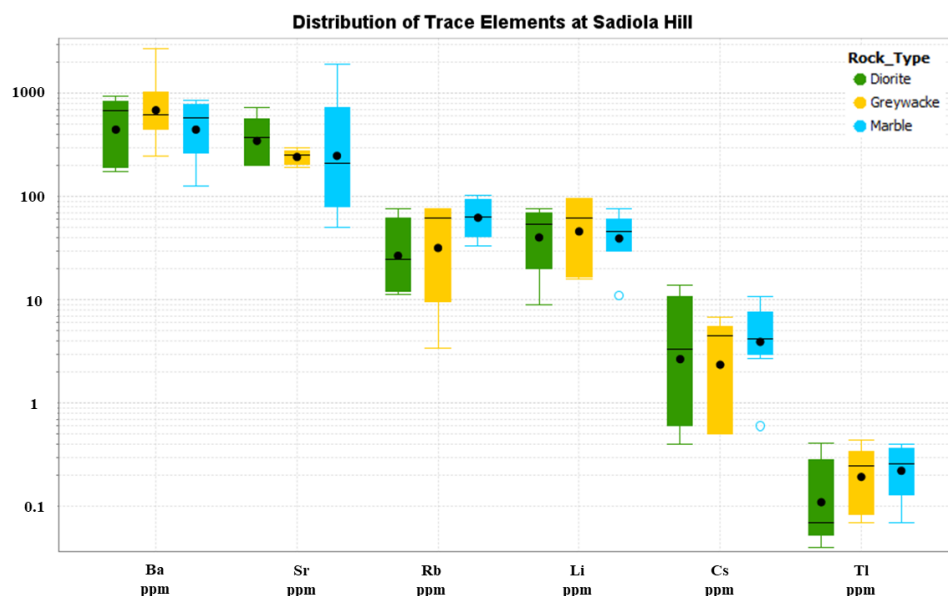
Figure 29. Logarithmic scale box and whisker plot showing distribution of gold-associated trace elements at Sadiola Hill deposit. Box magnitude represents the interquartile range. Whiskers show regular minimum and maximum values with outliers removed (shown as empty circles). Mean value shown as a clack circle in the box. Black line shows median value.

4.4.3 Pathfinder Elements

The distribution of pathfinder elements typical of gold systems, as outlined by Goldfarb and Groves (2015), were evaluated in the geochemical dataset (Figure 30). Arsenic and antimony correlate best with gold, consistent with sulphide-gold paragenetic sequence defined by Masurel et al. (2017). Background As values in the least altered samples is ~30 ppm in the greywacke and diorite, reaching 180 ppm in the marble. In samples with high gold content As values reach 2000-3000 ppm. Sb background value is ~2 ppm regardless of the rock type, reaching 10-15 ppm in well-mineralized samples. Tungsten also correlates well with gold, with background values of ~2 ppm and elevated levels of ~13 ppm in well-mineralized samples.

With exception of zinc with slightly elevated values in the ore zone reaching ~200 ppm, base metals do not show significant enrichment, consistent with low salinity values of the auriferous fluid (Goldfarb and Groves, 2015). Copper content is at the average crustal level of ~50-100 pp, as outlined by Phillips and Powel (2010). Bismuth, tellurium, and molybdenum values are low and generally do not exceed detection limits. Silver and selenium have no association with gold and with exception of a few samples with background values, fall below detection limit.
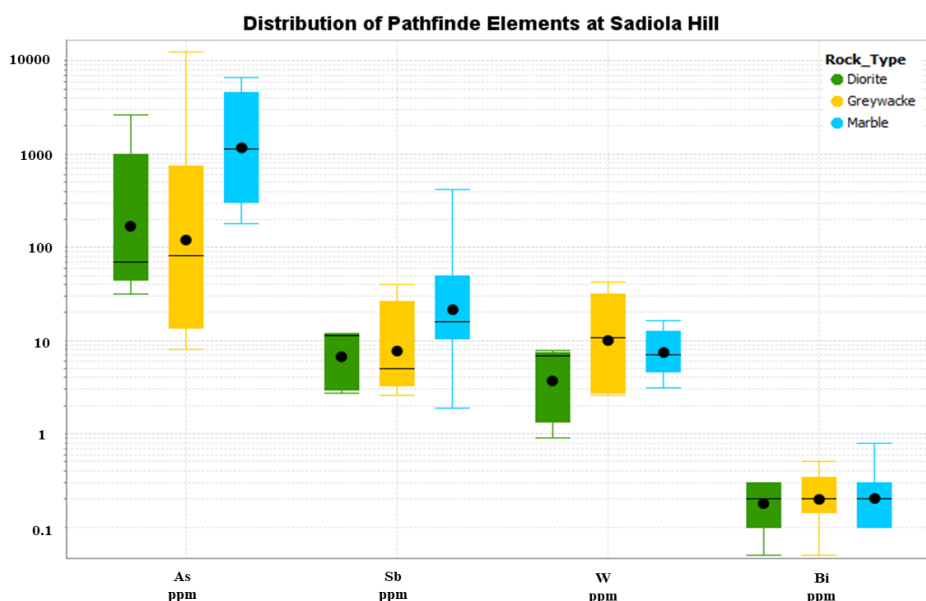
Figure 30. Logarithmic scale box and whisker plot showing distribution of common gold pathfinder elements at Sadiola Hill deposit. Box magnitude represents the interquartile range. Whiskers show regular minimum and maximum values with outliers removed. Mean value shown as a clack circle in the box. Black line shows median value.

5   DISCUSSION

High-resolution SWIR hyperspectral imaging

Several benefits of the high-resolution scanning technique over conventional transmitted light microscopy were identified during this study. Specific chemical properties of spectrally active minerals, such as Mg-Al-content in white mica and changes in illite crystallinity are well established. Vein-controlled muscovite shows a veinward increase in crystallinity likely reflecting higher fluid-rock interaction on vein margins, with ambient temperature of the wall-rock influencing the muscovite's crystallinity properties (Figure 31, A). Fe-content in carbonates and abrupt changes in carbonate mineralogy are well-captured (Figure 31, B and C). As such, coarse carbonate veins at Sadiola often show coexistence of Fe-dolomite and Fe-bearing calcite. Transition towards Fe-rich centres of the vein reflect Fe saturation as crystallization proceeds.
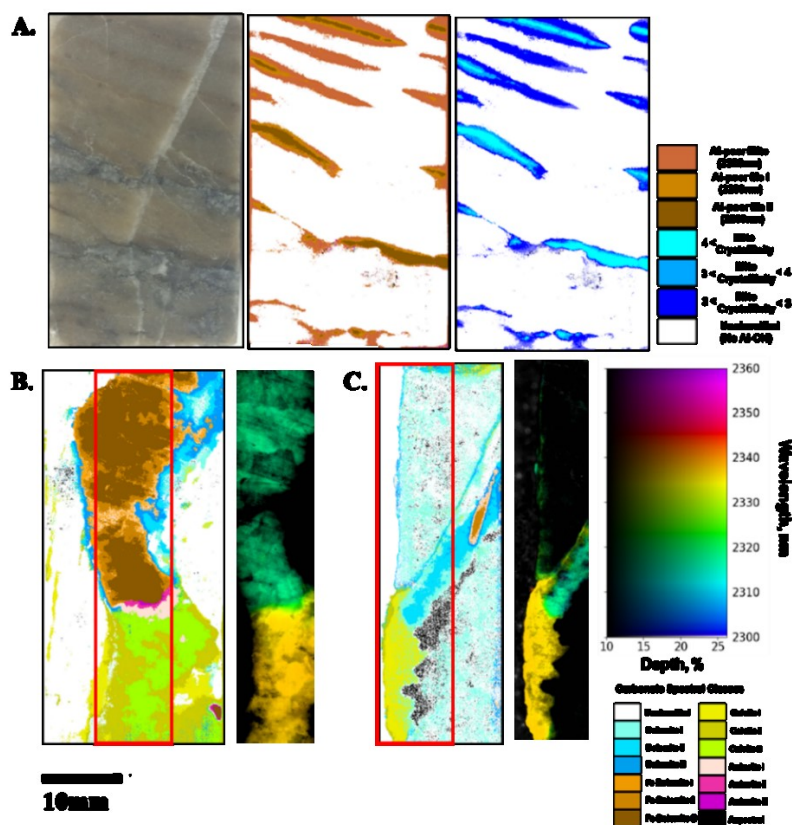
Figure 31. A. Scanned drill core surface (left), white mica mineral map (centre), and illite crystallinity map (right) of sample SD048-SD93 showing veinward increase in illite crystallinity with Al-OH absorption feature remaining at 2208nm. **B.** Vein-controlled carbonate assemblages showing abrupt change from ferroan dolomite-ankerite to calcite and lateral zonation within the vein (sample SD129-SD66). **C.** Vein-controlled carbonate assemblages showing abrupt change from dolomite to calcite and lateral zonation within the vein (sample SD119-SD64). Wavelength maps of 2300-2360nm range (B. and C.) show position of the carbonate feature in the area of the samples outlined by the red rectangle.

Comparison of the 0.2mm and 0.26µm mineral maps (Figure 32) shown that the both scales are compatible for coarser grained alteration minerals, e,g vein-controlled carbonate (Figure 32, A). Classification of fine-grained alteration minerals, e.g. illite-muscovite clusters, is notably more detailed at 26µm resolution (Figure 32, B). Furthermore, abundance of unclassified pixels in white mica mineral maps increased at 0.2mm resolution, likely due to carbonate interference with the muscovite/ illite spectral responses.
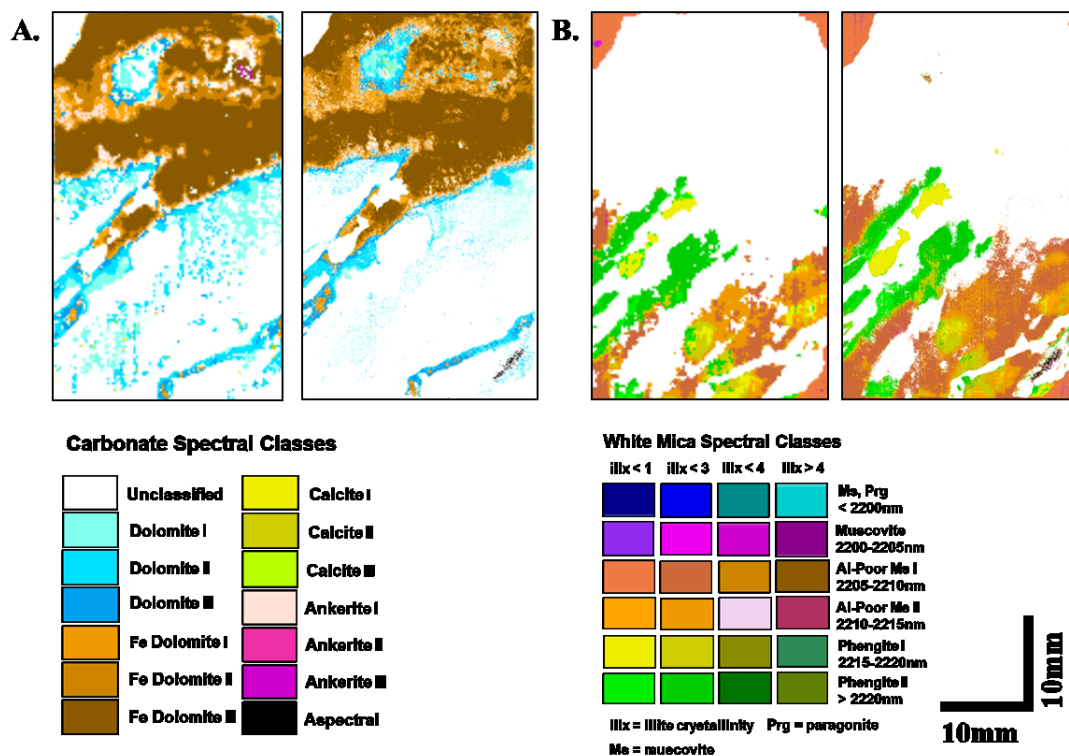
Figure 32. A. Carbonate mineral maps at 0.2mm (left) and 0.26µm (right) pixel-resolutions (sample SD048-SD91) **B.** White mica mineral maps at 0.2mm (left) and 0.26µm (right) pixel-resolutions (sample SD048-SD91)

An estimation of mineral abundances based on distribution of spectral classes is accurate for minerals exceeding 26µm pixel size if not mixed with other spectrally active minerals. However, discrepancies in estimation of fine-grained, sub-pixel size, white mica (e.g. SD22-SD50) occur when white mica flakes are disseminated in the matrix of minerals not active in the SWIR range, such as quartz and feldspars. This resulted in pixel population with spectral parameters of white mica that amount for ~20% of a pixel's area. In these samples, visual estimation abundances from petrographic observations were more reliable. However, relative abundances of different spectral classes of white mica were reliable making it possible to scale back

the abundance and acquiring a representative result. Abundance of epidote in sample SD75 that occur as fine-grained clusters was also overestimated.

Unmatching of spectrally active features was revealed during the qualitative analyses obscuring one-to-one comparison of a mineral map with its corresponding thin section. This discrepancy is explained by workflow in some of the studied samples. Specifically, the thin sections were prepared for another study, and offcut slabs subsequently imaged as part of this study. As a result, there is a 5-7mm difference between a scanned drill core surface and a surface represented by the thin section, which often led to an imperfect match. However, it was possible to correlate spectrally responsive features, such as carbonate veins or muscovite altered argillite, between mineral maps and thin sections indirectly validating a sample's spectral signature.

Finally, spectrally active minerals at Sadiola that commonly occur at sub-pixel scale led to unresolved mineral mixtures and require more scrupulous investigation. Classification of biotite was problematic because depths of absorption features were too shallow. However, when together in mixtures with white mica or carbonate, subtle biotite Fe-OH and Mg-OH absorption features were recognized in the expression of spectral classes, i.e., carbonate absorption feature at 2331nm, weak Al-OH feature at 2214nm, biotite feature at 2247nm.

Updated paragenesis

The previously accepted paragenetic model from Masurel et al. (2017) was improved by hyperspectral imaging combined with petrographic observations. This studies characterized the widespread zone of potassic biotite as early syn-mineral assemblage that is consistently overprinted by the ore-stage muscovite, muscovitic illite, or Al-poor poor muscovites (Figure 33, A and D). Phlogopite, on the other hand, is coeval with the white mica species occurring as Mg-rich phase after sulphidation reactions with Fe-Mg biotite. Syn-mineralization carbonate assemblages consist of ferroan dolomite-ankerite in the greywacke and diorite, and dolomite in the impure marble. Post-ore alteration assemblages consist of phengite (Figure 33, B), calcite (Figure 33, C), and chlorite. Phengite and calcite re-open and microbrecciate syn-mineral Fe-dolomite-ankerite veins or occur as late veins crosscutting syn-ore features.

Intermediate Mg-Fe- and Mg-rich chlorites are present as replacement of biotite and as rare veinlets.
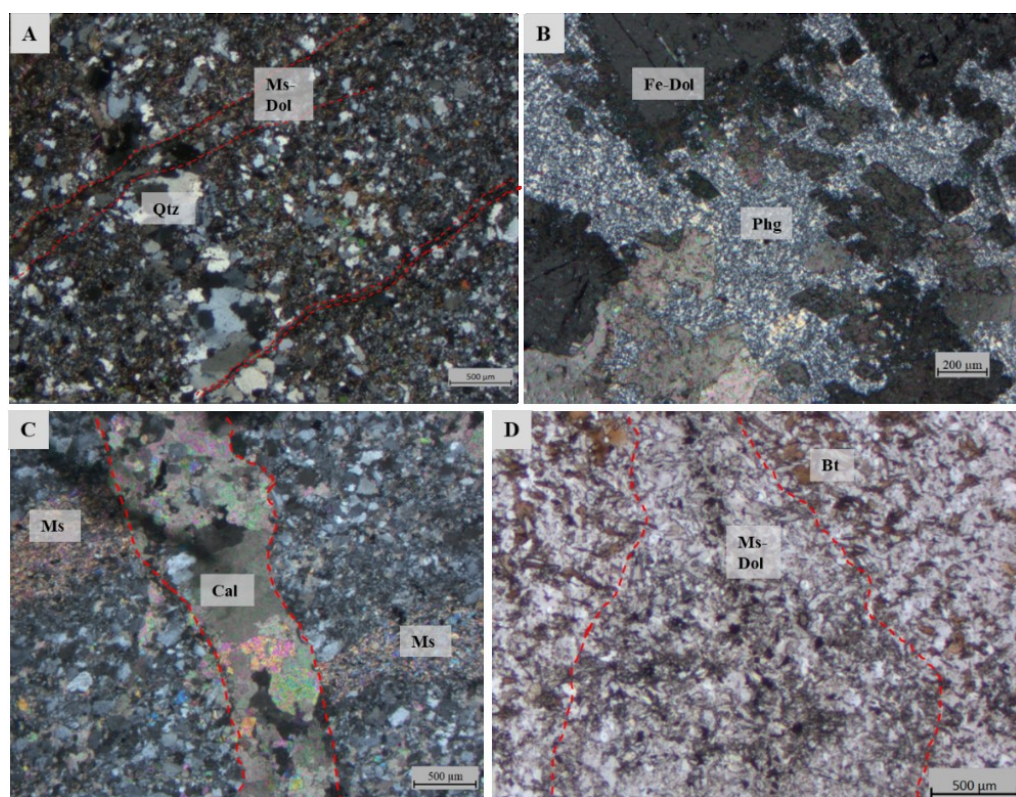
Figure 33. Photomicrographs taken in crossed polarized light highlighting key cross-cutting relationships and replacement textures among Sadiola Hill alteration minerals. **A.** Muscovite-carbonate veinlets crosscutting an early recrystallized quartz vein (sample SD22-SD48). **B.** Late fine-grained phengite reopening and brecciating an ore-stage ferroan dolomite vein (sample SD048-SD91) **C.** Al-poor muscovite vein is cut and offset by a late calcite vein (sample SD048-SD93). **D.** Pervasive biotite alteration is crosscut by Al-poor muscovite-dolomite-pyrite vein with biotite replaced by the muscovite in the vein halo (SD042-SD83).

Genetic Model

The timing of sulphide-gold introduction at the Sadiola Hill deposit post-dated peak regional metamorphism evident, as from sulphides overprinting biotite porphyroblasts. It has been suggested that pervasive albitization in other deposits as Loulo deposit group, is linked to cooling of intrusive bodies (Lawrence et al., 2013). If albitization in the Sadiola goldfield is similar in origin, the magmatic hydrothermal alteration at Sadiola Hill is clearly pre-ore.

White mica- Fe-dolomite/dolomite syn-ore mineral associations documented in this study reflect near neutral pH (Goldfarb et al., 2005). As-Sb-W trace element associations indicate a mesozonal environment for deposit formation (Goldfarb and

Groves, 2015). Furthermore, enrichment in As and Sb indicate a low salinity fluid with $Au(HS)_2^-$ complexes as main ligand (Kerrich, 1983; Goldfarb and Groves, 2015). Pyrrhotite dominance over pyrite and lack of Te enrichment are consistent with poor Te solubility in reduced conditions with sulphur fugacities above pyrrhotite-pyrite buffer (Goldfarb et al., 2005).

Observed changes in iron sulphide speciation from pyrrhotite to pyrite to marcasite record a continuous change in oxygen fugacity. The original auriferous fluid was CO_2-rich, which favoured compositional maintenance due to buffering capacities of the carbonic fluid (Phillips and Powel, 2010). The fluid was introduced into the Sadiola country rocks during sinistral reactivation of the Sadiola fracture zone and the NNE fault splays during the D_3 event (Cameron, 2010). The reactivation of the fault network likely signified a switch from compressional to transpressional regime. Depressurization led to fluid unmixing leading to CO_2 introduction into the country rock causing dolomite alteration in the marble and ferroan dolomite alteration in the greywacke and diorite. Loss of CO_2 drastically changed the fluid's buffering capacity making it susceptible to rapid pH changes controlled by the host rock composition. Carbonate reduction might have occurred if the argillite laminae contained organic matter. However, at Sadiola Hill sulphidation reactions with pre-existing Fe-Mg biotite is the most plausible mechanism for destabilization of the bisulfide complexes and taking gold out of solution. The sulphidation resulted in precipitation of pyrrhotite-arsenopyrite-pyrite leading to reduction of the HS^- activity and precipitation of gold. In light of this, the argillaceous-silty layers in the impure carbonate acted as a chemical trap for auriferous fluids with Fe^{2+} for sulphidation reactions sourced from biotite.

Finally, the footwall carbonate at Sadiola was important for ground preparation prior to introduction of the auriferous fluid. The difference in competency between the footwall impure carbonate and the hanging wall greywacke resulted in the former undergoing far more deformation (Cameron 2010). The rheological differences facilitated shearing and development of the NNE-fault network that later channelized the hydrothermal fluid flow. Although gold mineralization can be found in both hanging wall and footwall host rocks, the impure carbonate is a favourable host for gold mineralization due to its intrinsic properties, such as permeability facilitating the fluid flow, and presence of argillite laminae, i.e., the sites for chemical trapping of gold through sulphidation of biotite.

6   CONCLUSIONS

This section of the manuscript addresses the main objectives of the study and specific research questions that were outlined in the thesis proposal. If an on objective was not achieved recommendations are made to improve any future studies of similar nature.

Number of hydrothermal events and their relative timing

A total of 6 distinct hydrothermal alteration assemblages were established by this study. Although, most of these assemblages were recognized in the past by Hein (2008) and Masurel et al. (2017), classification with high-resolution hyperspectral imaging allowed for refining and emplacement of more rigid paragenetic constraints. The following alteration classes are listed in the order from oldest to youngest, with the stage 5 alteration assemblage associated with gold mineralization.

1) Actinolite-tremolite calc-silicate assemblages related to emplacement of the diorite into the impure carbonate package (Hein, 2008; Masurel et al., 2017)
2) Early quartz occurring as silicification (Cameron, 2010), and barren quartz veins.
3) Pervasive albitization and minor scapolite (Hein, 2008). Defined as pre-ore assemblages in this study, might be cogenetic to the stage 4 alteration.
4) Widespread biotite+/-K-feldspar-tourmaline (late pre-ore stage)
5) Fe-dolomite-dolomite+/-ankerite- muscovite to Al-poor muscovite-phlogopite (syn-ore stage).
6) Phengite-calcite-chlorite (barren post-ore stage).

Alteration assemblages associated with gold

This study determined that gold is associated with ferroan dolomite/dolomite+/-ankerite- muscovite to Al-poor muscovite- phlogopite, cogenetic with sulphide precipitation. The intensity of white mica replacement of biotite, and abundance of Fe-bearing carbonates in association with phlogopite, are good predictors of gold mineralization (Figure 34, A and B). Abundant potassium in the fluid results in high muscovite abundances. Within well-mineralized samples phlogopite occurs as gangue silicate adjacent to, or spatially related to sulphides and the ore-stage Fe-bearing carbonates. The presence of phlogopite as a recrystallized Fe-

depleted, post-sulphidation phase has been well-documented by the microprobe study. As such, the Mg content in biotite at Sadiola can be used as exploration vectoring tool. Geochemical data also supports this statement since K/Al molar, Mg/Al molar, and total C enrichment positively correlated with increasing gold grade.
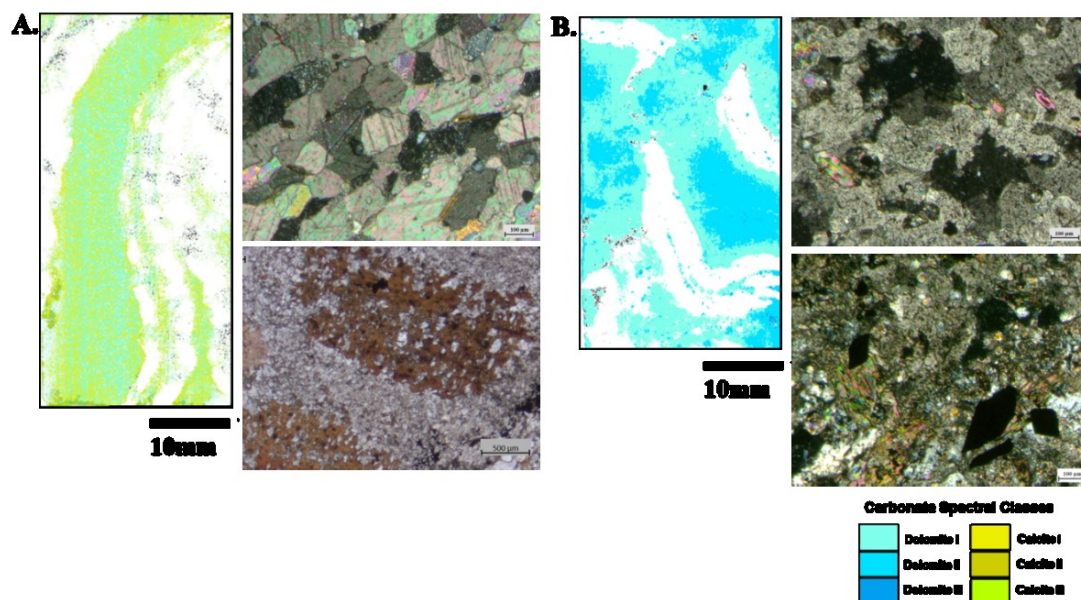
Figure 34. Unmineralized sample SD782-SD28 of the impure calcitic-dolomitic marble (A) and a high-grade equivalent of the same lithology, sample SD782-SD30 (B). Note the differences in carbonate morphology (photomicrographs on the top right): recrystallized metamorphic calcite-dolomite matrix with well-developed triple junctions among crystals (A) vs. patchy hydrothermal dolomite with irregular crystal boundaries. Bottom photomicrographs highlight the differences in biotite species with biotite porphyroblasts well-preserved in (A) and complete replacement of the primary biotite and introduction of muscovite-dolomite-phlogopite-arsenopyrite-pyrite-gold in (B).

Extent of hydrothermal footprint at Sadiola Hill

To reliably evaluate the extent of the hydrothermal footprint of the Sadiola ore system an additional study on drill core away from mineralized zones should be conducted and compared with the results of the current study. Drill holes outside of the Sadiola Hill main pit, or exploration drill holes within the broader goldfield will work best for this purpose. However, the host rocks outside of the deposit must belong to the same metasedimentary units as the diamond core from the Sadiola Hill main pit, or at least be of a same bulk chemical composition to avoid protolith influence on alteration mineralogy.

Protolith control on alteration expression and spatial variation in the chemical composition of alteration minerals

Differences in spectral expression of carbonate alteration in the greywacke, diorite, and impure carbonate were well-constrained during this study. Syn-mineralization carbonate is dolomite in the impure marble unit, but attain ferroan dolomite-ankerite composition in the greywacke and diorite. The differences in the Fe content between the ore-stage carbonates expressed in different rock types can be explained by progressive rock-buffering with the surrounding Fe-rich minerals within the diorite and greywacke. As the impure carbonate unit is Mg-rich, the ore-stage dolomite consistently shows low Fe-content. Furthermore, Fe in biotite was preferentially consumed by sulphidation reactions, leaving no residual iron for the dolomite.

Muscovite and Al-poor muscovite occur in all host rocks and are associated with gold grade in the impure carbonate and the greywacke. Protolith control is well-illustrated in sample SD22-SD50 tonalite in which white mica alteration is consistently more aluminous and attains higher crystallinity values, while the white mica introduced by the same fluid within the greywacke is Al-poor illite. These variational differences are attributed to availability of Al^{3+} and lower Mg^{2+} content in the tonalite to produce muscovite. The increase in crystallinity can be explained by the higher ambient temperatures of the tonalite. Mineral-scale variations were also noted in muscovite. When muscovite replaces biotite, Al-OH feature shifts to longer wavelengths (~2210nm) consistent with incorporation of Mg^{2+} from biotite into the muscovite crystal structure. Phengite occurs in the system as a minor post-mineral alteration phase. Illite crystallinity has a common trend of increasing veinward, which is attributed to lower degree of fluid-rock interaction in the vein centre and higher fluid/rock ratio.

Recognition of primary textures in hydrothermally altered rock

Primary metamorphic textures, such as alternating dolomite-calcite-rich and argillite laminations, are recognized in the impure marble with both medium-resolution and high-resolution hyperspectral imaging. Other textural features at Sadiola are obscured by alteration.

7 ACKNOWLEDGEMENT

8   REFERENCES

Agus, J.L., 2011. Mapping White Mica in Milled Porphyry Copper Pebbles Using Hyperspectral Imagery: An Exploration Study. MSc. Thesis Report. Faculty of Geo-Information Science and Earth Observation. University of Twente.

Bakker, W.H., 2013. HypPy Hyperspectral Python Software Package. ⟨http://www.itc.nl/personal/bakker/hyppy.html⟩

Bakker, W.H., van Ruitenbeek, F.J.A., van der Werff, H.M.A., Zegers, T.E., Oosthoek, J.H.P., Marsh, S.H., van der Meer, F.D., 2014. Processing OMEGA/Mars Express hyperspectral imagery from radiance-at-sensor to surface reflectance, Planetary and Space Science, Vol 90, Pages 1-9,

Bevan, M.J.D., 2018. High-resolution Short-wave Infrared (SWIR) hyperspectral characterisation of alteration at the Cortez Hills Carlin-Type Gold Deposit, Nevada, USA. MSc. Thesis Report. Faculty of Geosciences, Department of Earth Sciences, Utrecht University.

Cameron, G., 2010. A review and investigation into the controls of deep sulfide mineralization at the Sadiola gold deposit in Mali, West Africa: Unpublished report to the Société d'Exploitation des Mines d'Or de Sadiola S.A., 51 p.

Clark, R.N., King, T.V.V., Klejwa, M., Swayze, G.A., 1990. High spectral resolution reflectance spectroscopy of minerals. Journal of Geophysical Research. Vol. 95, pp.12,653-12,680.

Clark, R.N., 1999. Chapter 1: Spectroscopy of Rocks and Minerals, and Principles of Spectroscopy, in Rencz, A.N., ed., Manual of Remote Sensing, Volume 3: Remote Sensing for the Earth Sciences: New York, John Wiley and Sons, pp. 3-58.

Cox, S.F., 2005. Coupling between deformation, fluid pressures, and fluid flow in ore-producing hydrothermal systems at depth in the crust. Economic Geology, 100th Anniversary Volume, pp. 39–75.

Dalm, M., Buxton, M.W.N., van Ruitenbeek, F.J.A., 2017. Discriminating ore and waste in a porphyry copper deposit using short-wave infrared (SWIR) hyperspectral imagery. Mineral Engineering Vol. 105, pp. 10-18.

Deer, W.A., Howie, R.A., and Zussman, J., 1992. Introduction to Rock-Forming Minerals, 2nd ed.: New York, Longman Scientific and Technical, 696 p.

Duke, E.F., 1994, Near infrared spectra of muscovite, Tschermak substitution, and metamorphic reaction progress: implications for remote sensing, Geology, Vol. 22, pp. 621-624.

Gaffey, S. J., 1987. Spectral Reflectance of Carbonate Minerals in the Visible and Near Infrared (0.35-2.55 um): Journal of Geophysical Research, Vol 92, pp. 1429-1440.

Garagan, T., Montano, P., Lytle, W., Jones, K., Hunter, S., Morgan, D., 2015. NI 43-101 Technical report feasibility study on the Fekola gold project in Mali. B2Gold   Corp. www.b2gold.com/_resources/Fekola_Technical_Report_2015.pdf

Grimes, D.J., Stewart, K.C., Wilson, S.A., Kretschmer, E.L., 1996. The characterization of USGS Gold Reference Standard, DGPM-1, USGS open file report 96-058, p. 13.

Goldfarb, R.J., Baker, T., Dube, B., Groves, D.I., Hart, C.J.R., Gosselin, P., 2005. Distribution, Character, and Genesis of Gold Deposits in Metamorphic Terranes. Economic Geology 100th Anniversary Volume, pp. 407-450.

Goldfarb, R.J., Groves, D.I., 2015. Orogenic gold: Common or evolving fluid and metal sources through time. Lithos. Vol. 233, pp. 2-26.

Groves, D.I., Goldfarb, R.J., Gebre-Mariam, M., Hagemann, S.G., Robert, F., 1998. Orogenic gold deposits—a proposed classification in the context of their crustal distribution and relationship to other gold deposit types. Ore Geology Reviews. Vol. 13, pp. 7-27.

Groves, D.I., Goldfarb, R.J., Robert, F., Hart, C.J.R., 2003. Gold Deposits in Metamorphic Belts: Overview of Current Understanding, Outstanding Problems, Future Research, and Exploration Significance. Economic Geology. Vol. 98, pp. 1-29.

Harraden, C.L., Mcnulty, B.A., Gregory, M.J., Lang, J.R., 2013. Shortwave Infrared Spectral Analysis of Hydrothermal Alteration Associated with the Pebble Porphyry Copper-Gold-Molybdenum Deposit, Iliamna, Alaska. Economic Geology. Vol. 108, pp. 483-494.

Hein, K.A.A., Tshibubudze, A., 2007. Sadiola Ore Genesis Model, Sadiola Mine and satellite pits, Mali. Unpublished report to the Société d'Exploitation des Mines d'Or de Sadiola S.A., 15 p.

Hein, K.A.A., 2008. Geology of the Sadiola open cast and ancillary pits, Mali Unpublished report to the Société d'Exploitation des Mines d'Or de Sadiola S.A. School of Geosciences. University of the Witwatersrand Johannesburg. ADD PAGES

Hein, K.A.A., Matsheka, I.R., Bruguier, O., Masurel, Q., Bosch, D., Cady, R., Monie, P., 2015. The Yatela gold deposit: 2 billions in the making. Journal of African Sciences. Vol. 112, pp. 548-569.

Hirdes, W., and Davis, D.W., 2002. U-Pb Geochronology of Paleoproterozoic rocks in the southern part of the Kédougou-Kéniéba inlier, Senegal, West Africa: Evidence for diachronous accretionary development of the Eburnean Province. Precambrian Research. Vol. 118, pp. 83–99.

Houzar, S., Leichmann, J., 2003. Application of cathodoluminescence to the study of metamorphic textures in marbles from the eastern part of the Bohemian Massif. Bulletin of Geosciences, Vol. 78, No. 3, pp. 241-250.

Hunt, G.R., 1977. Spectral signatures of particulate minerals, in the visible and near-infrared, Geophysics Vol 42, pp. 501-513.

Kerrich, R., 1983. Geochemistry of gold deposits in the Abitibi Greenstone Belt. Canadian Institute of Mining and Metallurgy Special. Vol. 27 pp.1-75.

Lampinen, H.M., Laukamp, C., Occhipinti, S.A., Hardy, L., 2018. Mineral footprints of the Paleoproterozoic sediment-hosted Abra Pb-Zn-Cu-Au deposit Capricorn Orogen, Western Australia. Ore Geology Reviews. Accepted Manuscript.

Large, R. R., Gemmell, J. B., Paulick, H., and Huston, D. L., 2001, The alteration box plot: A simple approach to understanding the relationship between alteration mineralogy and lithogeochemistry associated with volcanic-hosted massive sulfide deposits. Economic Geology, Vol. 96, pp. 957-971.

Lawrence, D.M., Treloar, P.J., Rankin, A.H., Harbidge, P., Holliday, J., 2013. The geology and mineralogy of the Loulo Mining District, Mali, West Africa: evidence for two distinct styles of orogenic gold mineralisation. Economic Geology. Vol. 108, pp. 190-227.

Leake, B.E., Woolley, A.R., Birch, W.D., Burke, E.A.J., Ferrari, G., Grice, J.D., Hawthorne, F.C., Kisch, H.J., Krivovichev., V.G., Schumacher, J.C., Stephenson, N.C.N., and Whittaker, E.J.W., 2004, Nomenclature of amphiboles: additions and revisions to the International Mineralogical Association's amphibole nomenclature: American Mineralogist, v. 89, p. 883-887.

Maclean, W.H., and Krandiotis, P., 1987, Immobile elements as monitors of mass transfer in hydrothermal alteration: Phelps Dodge massive sulfide deposit, Matagami, Quebec: Economic Geology, Vol. 82, pp. 951–962.

Markwitz, V., Hein, K.A.A., Miller, J., 2015. Metallogenic portfolio of the West African craton. Ore Geology Reviews. Vol. 78. Article in press.

Markwitz, V., Hein, K.A.A., Miller, J., 2016. Compilation of West African mineral deposits: Spatial distribution and mineral endowment. Precambrian Res.

Masurel, Q., Miller, J., Hein, K.A.A., Hanssen, E., Thebaud, N., Ulrich, S., Kaisin, J., Tessougue, S., 2016. The Yatela gold deposit in Mali, West Africa: The final product of a long-lived history of hydrothermal alteration and weathering. Journal of African Earth Sciences Vol. 113, pp. 73-87.

Masurel, Q., Thebaud, N., Miller, J., Ulrich, S., Hein, K. A. A., Cameron, G., Beziat, D., Bruguier, O., Davis, J., 2017. Sadiola Hill: A World-Class Carbonate-Hosted Gold Deposit in Mali, West Africa. Economic Geology. Vol. 112, pp. 23-47.

Mathieu, M., Roy, R., Launeau, P., Cathelineau, M., Quirt, D., 2017. Alteration mapping on drill cores using a HySpex SWIR-320m hyperspectral camera: Application to the exploration of an unconformity-related uranium deposit (Saskatchewan, Canada). Journal of Geochemical Exploration. Vol. 172, pp. 71-88.

Milési, J.P., Feybesse, J.L., Ledru, P., Dommanget, A., Ouedrago, M., Marcoux, E., Prost, A., Vinchon, C., Sylvain, J.P., Johan, V., Tegyey, M., Calvez, J.Y., and Lagny, P., 1989. West African gold deposits in their Lower Proterozoic lithostructural setting. Chronique de la Recherche Miniere. Vol. 497, pp. 3–98.

Munro, M.A., Ord, A., Hobbs, B.E., 2018. Spatial organization of gold and alteration mineralogy in hydrothermal systems: wavelet analysis of drillcore from Sunrise Dam Gold Mine, Western Australia. Characterization of Ore-Forming Systems from Geological, Geochemical and Geophysical Studies. Geological Society, London, Special Publications. Vol. 453, pp. 165-205.

Ridley, J., 2013. Ore Deposit Geology. Cambridge University Press. pp. 409.

Phillips, G.N., Powell, R., 2010. Formation of gold deposits - a metamorphic devolatilization model. Journal of Metamorphic Geology. Vol. 28, pp. 689–718.

Phillips, G.N., Powell, R., 2015. A practical classification of gold deposits, with a theoretical basis. Ore Geology Reviews. Vol. 65, pp. 568–573.

Roache, T.J., Walshe, J.L., Huntington, J.F., Quigley, M.A., Yang, K., Bil, B.W., Blake, K.L., Hyvarinen, T., 2011. Scripts for automatic extraction of mineral abundance and composition. Australian Journal of Earth Sciences, Vol. 58, pp. 813–822.

Rossman, G.R., 1988. Vibrational Spectroscopy of Hydrous Components. In: Spectroscopic methods in mineralogy and geology. Reviews in mineralogy. No.18. Mineralogical Society of America, Washington, DC, pp. 193-206.

Swayze, G.A., Kokaly, R.F., Higgins, C.T., Clinkenbeard, J.P., Clark, R.N., Lowers, H.A., Sutley, S.J., 2009. Mapping potentially asbestos-bearing rocks using imaging spectroscopy. Geology. Vol 37, pp. 763–766.

van Ruitenbeek, F.J.A., Debba, P., van der Meer, F.D., Cudahy, T., van der Meijde, M., Hale, M., 2006. Mapping white micas and their absorption wavelengths using hyperspectral band ratios. Remote Sens. Environ., Vol. 102, pp. 211-222.

van Ruitenbeek, F.J.A., Bakker, W.H., van der Werff, H.M.A., Zegers, T.E., Jelmer H.P., Oosthoek, J.H.P., Marsh, S.H., van der Meer, F.D., 2014. Mapping the wavelength position of deepest absorption features to explore mineral diversity in hyperspectral images, Planetary and Space Science, Vol.101, pp. 108-117.

Villeneuve, M., 2008. Review of the orogenic belts on the western side of the WestAfrican craton: the Bassarides, Rokelides and Mauritanides. In: Ennih, N., Lié-geois, J.-P. (Eds.), The Boundaries of the West African Craton, Geological SocietySpecial Publication 297. pp. 169–201.

Thompson, A.J.B., Hauff, P.L., and Robitaille, A.J., 1999. Alteration Mapping in Expolation: Application of Short-Wave Infrared (SWIR) Spectroscopy. SEG Newsletter 39, pp. 16-27.

Turner, D., Groat, L.A., Rivard, B., Belley, P.M., 2017. Reflectance spectroscopy and hyperspectral imaging of sapphire-bearing marble from the Beluga occurrence, Baffin Island, Nunavut. The Canadian Mineralogist. Vol. 55, pp. 787-797.

Zaini, N., van der Meer, F., van der Werff, H., 2014. Determination of carbonate rock chemistry using laboratory-based hyperspectral imagery. Remote Sensing, Vol. 6, pp. 4149-4172.

Wang, R., Cuhady, T., Laukamp, C., Walshe, J.L., Bath, A., Mei, Y., Young, C., Roache, T.J., Jenkins, A., Roberts, M., Barker, A., Laird, J., 2017. White Mica as Hyperspectral Tool in Exploration for the Sunrise Dam and Kanowna Belle Gold Deposits, Western Australia. Economic Geology. Vol. 112, pp. 1153-1176.

Williams-Jones, A.E., Bowell, R.J., and Migdisov, A.A., 2009. Gold in solution: Elements. Vol. 5, pp. 281–287.

Winchester, J.A., Floyd, P.A., 1977. Geochemical discrimination of different magma series and their differentiation products using immobile elements. Chemical Geology Vol. 20(4) pp. 325-343

An overview of Sadiola Gold Mine. Mining Data Solutions, 2018 MDO Data Online Inc. 2018. https://miningdataonline.com/property/465/Sadiola-Mine.aspx#Owners

Appendix A

Summary of ME-MS89L analytes with lower and upper detection limits

Analyte	Symbol	Units	Lower Limit	Upper Limit
Silver	Ag	ppm	5	12500
Arsenic	As	ppm	4	25000
Barium	Ba	ppm	2	25000
Beryllium	Be	ppm	0.4	25000
Bismuth	Bi	ppm	0.1	25000
Calcium	Ca	%	0.1	25
Cadmium	Cd	ppm	0.8	25000
Cerium	Ce	ppm	0.2	25000
Cobalt	Co	ppm	0.5	25000
Cesium	Cs	ppm	0.1	25000
Copper	Cu	ppm	20	25000
Dysprosium	Dy	ppm	0.03	25000
Erbium	Er	ppm	0.02	25000
Europium	Eu	ppm	0.03	25000
Iron	Fe	%	0.05	25
Gallium	Ga	ppm	0.5	25000
Gadolinium	Gd	ppm	0.03	25000
Germanium	Ge	ppm	0.5	25000
Holmium	Ho	ppm	0.01	25000
Indium	In	ppm	0.3	25000
Lanthanum	La	ppm	0.08	25000
Lithium	Li	ppm	2	25000
Lutetium	Lu	ppm	0.05	25000
Manganese	Mn	ppm	10	25000
Molybdenum	Mo	ppm	2	25000
Niobium	Nb	ppm	0.8	25000
Neodymium	Nd	ppm	0.07	25000
Nickel	Ni	ppm	10	25000
Lead	Pb	ppm	0.5	25000
Praseodymium	Pr	ppm	0.03	25000
Rubidium	Rb	ppm	0.5	25000
Rhenium	Re	ppm	0.01	25000
Antimony	Sb	ppm	0.3	25000
Selenium	Se	ppm	3	25000
Samarium	Sm	ppm	0.04	25000
Tin	Sn	ppm	3	25000
Strontium	Sr	ppm	20	25000
Tantalum	Ta	ppm	0.04	25000
Terbium	Tb	ppm	0.01	25000
Tellurium	Te	ppm	0.5	25000
Thorium	Th	ppm	0.1	25000
Titanium	Ti	%	1	25
Thallium	Tl	ppm	0.02	25000
Thulium	Tm	ppm	0.01	25000
Uranium	U	ppm	0.2	25000
Vanadium	V	ppm	1	25000
Tungsten	W	ppm	0.3	25000
Yttrium	Y	ppm	0.2	25000
Ytterbium	Yb	ppm	0.02	25000
Zinc	Zn	ppm	10	25000

Appendix B.1

EPMA Standards

Na2O	S	F	MnO	Cl	MgO	K2O	As2O5	CaO	ZnO	Al2O3	FeO	TiO2	SiO2	Total	Standard
4.055	0	0	0.028	0.009	0.07	0.372	0.009	12.383	0.002	29.386	0.439	0.068	54.063	100.892	std-plg-1
0.004	0.014	0	0.104	0.049	19.531	8.563	0.444	0.107	0.161	15.046	9.826	1.492	39.416	95.523	std-biotite
4.121	0.01	0	0.045	0.001	0.103	0.347	0	12.014	0.002	29.366	0.357	0.071	53.83	100.265	std-plg-2
0.121	0.008	0	0.142	0.049	19.731	8.556	0.42	0.136	0.229	15.201	9.556	1.585	39.8	96.252	std-biotite
3.877	0.007	0	0.007	0.013	0.08	0.356	0.003	12.52	0.006	29.877	0.399	0.085	55.485	102.711	std-plg-1
0.056	0.015	0	0.046	0.098	19.855	8.845	0.43	0.023	0.158	15.549	9.693	1.685	39.374	96.476	std-biotite
														Values reported in weight %	

Appendix B.2

Electron microprobe data (chlorite)

Sample_ID	SiO2	TiO2	Al2O3	V2O3	Cr2O3	FeO	MgO	MnO	Na2O	K2O	CaO	NiO	ZnO	F	Cl	Mineral
SD9202_13	0.44867	0.001427	0.206814	0	0	0.393047	0.311777	0.000169	0	0.000658	0	0	0.001966	0	0.001044	Chlorite
SD42_2	0.520053	0.0002	0.197565	0	0	0.333072	0.370009	0	0	0.003291	0.002142	0	0.000553	0	0.000169	Chlorite
SD42_1	0.52924	0.000213	0.18099	0	0	0.318179	0.406407	0.000634	0	0.000839	0.002033	0	0.000369	0	0.000451	Chlorite
SD21_14	0.510965	0.000351	0.160943	0	0	0.315075	0.450844	0.007387	0	0.000403	0.001815	0	0.000332	0	0.000197	Chlorite
SD21_17	0.461735	0	0.219269	0	0	0.295297	0.441689	0.003017	0	0	0.003013	0	0.001327	0	0.000536	Chlorite
SD32A_3	0.514843	0.001327	0.160384	0	0	0.302701	0.470743	0.00031	0	0.010414	0.002849	0	0.000283	0.111684	0.001157	Chlorite
SD21_8	0.483071	0.000613	0.196378	0	0	0.275045	0.49275	0.002227	0.001694	0	0.000944	0	0.002543	0	0.000254	Chlorite
SD85_13	0.499348	0.000376	0.169005	0	0	0.228585	0.495256	0.000804	0.000274	0.00034	0.000653	0	0.001204	0	0.000113	Chlorite
SD85_9	0.453946	0.001139	0.204136	0	0	0.217339	0.495206	0.000959	0.000226	0	0.000272	0	0.000749	0	0.000733	Chlorite
SD62_7	0.513162	0	0.194535	0	0	0.216462	0.526766	0	0.001791	0.000234	0.001906	0	0.001573	0	0.003385	Chlorite
SD42_6	0.564224	0.026277	0.174301	0	0	0.201986	0.521432	0.000564	0.000387	0.022421	0.001343	0	0.00027	0	0.001664	Chlorite
SD48_3	0.556152	0	0.131923	0	0	0.209266	0.570062	0.000381	0	0.00018	0.001633	0	0.000995	0	0	Chlorite
SD48_6	0.55507	0.000325	0.132531	0	0	0.203114	0.560609	0.000395	0.001258	0.000308	0.002287	0	0.000319	0	0	Chlorite
SD50_3	0.526344	0.003192	0.188444	0	0	0.194164	0.56051	0.000578	0.000613	0.008631	0.000526	0	0.000774	0	0.000762	Chlorite
SD93_13	0.49091	0.000351	0.198212	0	0	0.195278	0.591623	0.000254	0.002291	0.000977	0.00069	0	0.000737	0	0.000339	Chlorite
															Elements reported in moles	

Appendix B.3

Electron microprobe data (white mica)

Sample_ID	SiO2	TiO2	Al2O3	V2O3	Cr2O3	FeO	MgO	MnO	Na2O	K2O	CaO	NiO	ZnO	F	Cl	Mineral
SD48_7	1.062557	0.027041	0.249173	0	0	0.00895	0.050267	4.23E-05	0.001049	0.070916	0.000581	0	0	0	0	white mica
SD69_2	0.966442	0.001665	0.282646	0	0	0.016828	0.104976	0.000141	0.001371	0.078591	0.002904	0	0.001155	0	0.000564	white mica
SD91_11	0.966858	7.51E-05	0.280489	0	0	0.015505	0.092645	0	0.001097	0.067699	0.003703	0	0.000283	0.003316	0.000197	white mica
SD48_13	0.889034	0.026528	0.276409	0	0	0.014601	0.08741	0.000141	0.001226	0.087679	0.000944	0	0.00016	0	0.000592	white mica
SD91_7	0.935868	0	0.294592	0	0	0.011177	0.07952	0.000381	0.002743	0.084791	0.002886	0	0.00113	0.002526	0.000762	white mica
SD48_4	0.907508	0.026127	0.305273	0	0	0.011483	0.07684	0.000409	0.001258	0.070417	0	0	0.00043	0	0.000226	white mica
SD48_10	0.917111	0.030033	0.321092	0	0	0.008421	0.055701	4.23E-05	0.000323	0.071139	0.000181	0	0.000197	0	0.000113	white mica
SD69_5	0.922887	0.001252	0.322083	0	0	0.007989	0.054609	0	0.012343	0.085035	0.001579	0	0.000528	0	0.000141	white mica
SD36_5	0.852635	0.016062	0.317189	0	0	0.032375	0.094059	0	0.003566	0.074536	0.002559	0	0.000799	0.011842	0.000818	white mica
SD21_9	0.892496	0.005646	0.32374	0	0	0.023508	0.071456	0	0.003082	0.067859	0.000672	0	0.000504	0.026053	0.000254	white mica
SD21_13	0.872341	0.00984	0.321681	0	0	0.030927	0.060068	0.000507	0.002678	0.079175	0.001071	0	0.000319	0.006263	0	white mica
SD48_1	0.902682	0.01968	0.329301	0	0	0.007057	0.049052	0	0.000581	0.065969	0.000309	0	0.00113	0	8.46E-05	white mica
SD21_15	0.893345	0.001778	0.328654	0	0	0.025123	0.062475	4.23E-05	0.002001	0.070226	0.000871	0	0.001192	0.019789	0.000141	white mica
SD50_1	0.871709	0.00343	0.3217	0	0	0.012095	0.057339	0	0.007648	0.084982	0.000744	0	0.000553	0	0.009027	white mica
SD21_16	0.873256	0.002692	0.324662	0	0	0.028004	0.063616	0.000268	0.001388	0.074589	0.000799	0	0.000934	0.024053	0.000677	white mica
SD21_6	0.885339	0.006209	0.329968	0	0	0.025875	0.061432	0	0.002146	0.071648	0.001107	0	0.000725	0.021632	5.64E-05	white mica
SD93_7	0.87532	0.002842	0.328183	0	0	0.012221	0.052327	0.000959	0.00405	0.076065	0	0	0.001388	0	0.000169	white mica
SD93_10	0.878116	0.002178	0.334195	0	0	0.011664	0.061011	8.46E-05	0.008067	0.079823	0.0002	0	0	0	0.000254	white mica
SD93_6	0.859376	0.00348	0.329929	0	0	0.013042	0.046322	0.000155	0.004582	0.07787	0.000109	0	0.000246	0	5.64E-05	white mica
SD32A_14	0.888618	0.004294	0.343258	0	0	0.014086	0.046943	0	0.003808	0.086681	0.000272	0	0	0.007684	0	white mica
SD50_15	0.854633	0.020418	0.339492	0	0	0.015644	0.04667	4.23E-05	0.001468	0.081373	0.000127	0	0.000221	0	0.000169	white mica
SD50_5	0.895442	0.011981	0.351447	0	0	0.013724	0.050491	0.000141	0.004566	0.075513	0.000327	0	0.000455	0	0.000197	white mica
SD66_12	0.840086	0.010729	0.336481	0	0	0.026501	0.04801	0.000367	0.002114	0.092	1.81E-05	0	0.000209	0.001632	0.000987	white mica
SD93_1	0.86144	0.005133	0.337893	0	0	0.008894	0.055081	0	0.004453	0.075216	0.000345	0	0	0	0.000367	white mica
SD32A_21	0.850089	0.011004	0.338668	0	0	0.015143	0.048506	0	0.00334	0.073411	0.000599	0	0	0.005842	0.000197	white mica
SD50_8	0.854866	0.012794	0.341669	0	0	0.015324	0.047315	0.000268	0.006712	0.077339	0.000163	0	0.000111	0	0.000254	white mica
SD93_4	0.84478	0.00676	0.335363	0	0	0.009367	0.044338	0.000211	0.00547	0.078867	0.006026	0	8.6E-05	0	0.000423	white mica
SD93_8	0.851837	0.005859	0.337765	0	0	0.012944	0.043618	0.000761	0.006696	0.073379	0	0	0	0	0	white mica
SD93_14	0.841401	0.013445	0.33955	0	0	0.019375	0.048555	0	0.004066	0.075428	0.002196	0	0.000577	0	0	white mica
SD21_3	0.875753	0.005984	0.349093	0	0	0.018707	0.053096	0	0.003017	0.065926	0.000708	0	0.000135	0.012105	0.000169	white mica
SD90_6	0.896907	0.000501	0.356704	0	0	0.010342	0.024588	0.000691	0.003372	0.080375	0.001234	0	0.000995	0	0.000226	white mica
SD50_6	0.870577	0.002404	0.356459	0	0	0.01428	0.042303	0.000211	0.004308	0.077073	0.000635	0	0.000848	0	0.000226	white mica
SD50_4	0.824625	0.000538	0.351123	0	0	0.010884	0.029525	0	0.00768	0.101013	0	0	0	0	0	white mica
													All values reported in moles			

Appendix B.4

Electron microprobe data (biotite).

Sample_ID	SiO2	TiO2	Al2O3	V2O3	Cr2O3	FeO	MgO	MnO	Na2O	K2O	CaO	NiO	ZnO	F	Cl	Mineral
SD69_1	0.70213	0.014059	0.154078	0	0	0.073073	0.554431	0	0.003324	0.10424	7.26E-05	0	0.00102	0.069526	0.00079	Biotite
SD44_12	0.702779	0.004882	0.157982	0	0	0.07722	0.569888	0.000169	0.002323	0.086256	0.00127	0	0.000762	0	0.00268	Biotite
SD69_4	0.687018	0.009539	0.167544	0	0	0.081229	0.536666	0	0.000581	0.1039	0	0	0.00027	0.052737	0.00141	Biotite
SD44_9	0.675384	0.005997	0.1693	0	0	0.088007	0.547955	0.000409	0.005034	0.090482	0.001307	0	0.001868	0	0.003385	Biotite
SD30_3	0.696255	0.008513	0.152882	0	0	0.090861	0.514187	0.000592	0.001355	0.10683	0.001162	0	0	0.138316	0.001693	Biotite
SD32A_16	0.690264	0.009652	0.155353	0	0	0.119352	0.45861	0.000211	0.000758	0.091235	0.000436	0	0.001094	0.126789	0.000987	Biotite
SD32A_18	0.676416	0.014334	0.152891	0	0	0.138225	0.472628	0.001085	0.001952	0.104856	0	0	0.000983	0.118368	0.001157	Biotite
SD43_6	0.675884	0.035454	0.160973	0	0	0.1343	0.447594	0.000268	0.00142	0.088273	0.000163	0	0.000934	0	8.46E-05	Biotite
SD43_11	0.670691	0.034302	0.159825	0	0	0.137766	0.450646	0.000479	0.002469	0.087636	0	0	0.001438	0	5.64E-05	Biotite
SD50_12	0.663651	0.021307	0.178833	0	0	0.136486	0.411196	0.000959	0.001646	0.104123	0	0	0.000983	0	0.000367	Biotite
SD90_1	0.66192	0.016212	0.180461	0	0	0.149778	0.450844	0.000127	0.001484	0.086394	0.000744	0	0.001438	0	0.007024	Biotite
SD21_11	0.698802	0.013796	0.138288	0	0	0.159618	0.453945	0.001579	0	0.095312	0.004755	0	2.46E-05	0.128842	0.00615	Biotite
SD90_3	0.662586	0.02132	0.190808	0	0	0.158254	0.449529	0.000197	0.000194	0.084791	0.001053	0	7.37E-05	0	0.00598	Biotite
SD90_5	0.656877	0.01665	0.196427	0	0	0.153592	0.432682	0.000663	0.002856	0.095142	0	0	0.001487	0	0.00615	Biotite
SD50_14	0.653565	0.021107	0.178999	0	0	0.14904	0.418242	0.00172	0.00021	0.101066	0.00049	0	0.000786	0	0.000874	Biotite
SD21_10	0.692926	0.01322	0.146026	0	0	0.161456	0.452854	0.001311	0	0.101331	0.000218	0	0	0.117211	0.005303	Biotite
SD50_2	0.666497	0.014597	0.183413	0	0	0.149945	0.415662	0	0.001178	0.098645	0.000345	0	0.00086	0.016368	0.000536	Biotite
SD50_9	0.670558	0.020318	0.183736	0	0	0.156097	0.429333	0.001522	0.001404	0.091363	3.63E-05	0	0.000565	0.000526	0.000931	Biotite
SD50_7	0.653415	0.020656	0.181177	0	0	0.156918	0.424172	0.000423	0.001065	0.095875	0.000454	0	0.001118	0.006684	0.000874	Biotite
SD43_2	0.656328	0.036931	0.169731	0	0	0.155624	0.403306	0.000409	0.001323	0.081861	0	0	0.001216	0.001737	0.000282	Biotite
SD21_7	0.674219	0.022709	0.161434	0	0	0.181721	0.406184	0.001438	0.000662	0.100832	0.000163	0	0.000725	0.082053	0.002059	Biotite
SD57_6	0.660089	0.021733	0.148086	0	0	0.212843	0.385913	0.002058	0.004937	0.093422	0.001379	0	4.91E-05	0.010421	0.003893	Biotite
SD57_4	0.652067	0.022785	0.147115	0	0	0.215738	0.375964	0.001776	0	0.096957	0	0	8.6E-05	0.003474	0.003554	Biotite
SD57_1	0.657609	0.029708	0.147968	0	0	0.22228	0.370902	0.002636	0.00071	0.09373	0.000218	0	0.000528	0.007316	0.001382	Biotite
SD28_2	0.649504	0.021933	0.172379	0	0	0.219914	0.344503	0.000592	0.001726	0.10028	0.000472	0	0.001352	0.058	0.00409	Biotite
															All values reported in moles	

Appendix B.5

Electron microprobe data (carbonates)

Sample_ID	SiO2	TiO2	Al2O3	FeO	MgO	MnO	Na2O	K2O	CaO	ZnO	F	Cl
SD21_12	0	0.000134	5.74E-05	0.010611	0.005104	0.005209	0.000503	0.000476	0.974219	0.000587	0	8.25E-05
SD28_5	0	0	0	0.018963	0.016103	0.001872	0	0.000139	0.960408	0.000495	0	0.000454
SD28_6	0	0	0.018015	0.017006	0.000802	0	0.000291		0.961867	0.00059	0	0.000172
SD30_2	0	0.000278	0	0.010266	0.521664	0.001783	0.000498	0.00082	0.541241	0.000664	0	0.003105
SD30_6	0	1.3E-05	0	0.005566	0.559109	0.000382	0.000521	0	0.519789	0.000665	0	8.81E-05
SD32A_10	0	9.73E-05	2.18E-05	0.005766	0.006117	0.002865	0.000591	0	0.981593	0.001201	0.000117	3.13E-05
SD32A_17	0	0	0	0.015092	0.022252	0.003083	0	0.000295	0.957538	0.000995	0	0.000326
SD32A_22	0	0.000198	3.11E-05	0.007996	0.016508	0.003067	0	0	0.971872	0	0	0.000298
SD36_1	0	0.000106	7.37E-05	0.001804	0.522612	0.000927	0.00153	0.000219	0.553441	0	0	0
SD36_2	0	9.72E-05	0	0.010027	0.54056	0.00256	0.000392	0	0.528379	0.000107	0	0.000219
SD36_6	0	0	0	0.007005	0.546903	0.001405	0	0.000108	0.526873	0.001212	0	0.000287
SD36_7	0	0	0	0.123811	0.408196	0.000722	0.001784	2.86E-05	0.508843	0.000265	0	0.000357
SD36C_3	0	0	0	0.156773	0.388077	0.000443	0	0.000248	0.489378	0.000398	0	0
SD42_3	0	0	0	0.057463	0.472179	0.005483	0.0096	4.86E-05	0.526693	0.000394	0	0.000542
SD43_5	0	0	0	0.005833	0.008733	0.002352	0	0.00014	0.981964	0	0	0.000287
SD43_8	0	0.000152	0	0.00243	0.00562	0.002555	0	0	0.986637	0.001385	0	0.000404
SD43_9	0	0.000577	4.31E-05	0	0.004384	0.001795	0.000939	3.5E-05	0.990374	0.00062	0	0.000186
SD44_10	0	0.000499	0	0.002806	0.012914	0.002505	0	0.000459	0.979429	0.000924	0	9.64E-05
SD44_13	0	9.32E-05	0	0	0.005354	0.002383	0.000377	9.03E-05	0.989986	0	0.003581	3E-05
SD44_5	0	8.45E-05	0	0.058921	0.468438	0.002745	0.000311	0	0.532621	0	0	0.000109
SD44_6	0	0.000677	0	0.00335	0.012523	0.00302	0.000325	0.000113	0.979065	0.000339	0	0.000179
SD44_7	0	0.000179	0	0.005757	0.025888	0.003281	0.000836	4.68E-05	0.964907	0.000556	0	3.11E-05
SD50_10	0	0	6.74E-05	0.051655	0.466537	0.001897	0.000412	0.000177	0.543239	0	0	0.000111
SD50_11	0	0	0	0.062548	0.465185	0.001809	0	0.000225	0.532425	0	0	5.21E-05
SD62_10	0	9.7E-05	0	0.047358	0.490108	0.00448	0.001344	0.000123	0.523361	0.000714	0	0.000547
SD62_2	0	8.6E-05	0	0.03873	0.507959	0.003636	0	0	0.521538	0	0	0.001051
SD62_3	0	0.000162	0	0.002862	0.005422	0.0056	0.000504	0	0.982012	0.00082	0.00289	0
SD62_4	0	5.05E-05	9.89E-06	0.039089	0.503392	0.003383	0.000114	3.21E-05	0.525385	0	0	0.00054
SD62_5	0	0	0	0.04711	0.47377	0.004516	0.002321	0.000159	0.536839	0.00062	0	0.005702
SD62_8	0	5.26E-05	7.21E-05	0.005583	0.017507	0.00934	0.00061	0	0.96601	0.000206	0	0.000314
SD66_1	0	0	0	0.01878	0.539782	0.003317	0	0.000232	0.516832	0.001159	0	0.000504
SD66_2	0	0	5.24E-05	0.017707	0.547373	0.003403	0	0	0.512804	0.000433	0	0.000271
SD66_4	0	0.000247	0	0.00472	0.006711	0.003124	0.001578	0.000364	0.981816	0	0	0
SD66_7	0	3.04E-05	0	0.00147	0.017655	0.0038	0	6.45E-05	0.97714	0.000656	0	0.000137
SD66_8	0	0	0	0.004628	0.003046	0.002806	0	0	0.987486	0.000381	0	0
SD66_9	0	0.000126	0	0.005053	0.002162	0.001716	0.001568	0	0.98679	0.000631	0	3.15E-05

Sample_ID	SiO2	TiO2	Al2O3	FeO	MgO	MnO	Na2O	K2O	CaO	ZnO	F	Cl
SD69_3	0	5.19E-05	0	0.006942	0.026317	0.001769	0.002275	3.3E-05	0.964259	0	0	0.000146
SD69_6	0	0.000304	0	0.004693	0.010641	0.000925	0.001044	0.000134	0.981321	0.000342	0	0.000203
SD85_10	0	0	0	0.008437	0.569248	0.001374	0.001524	0.000183	0.505846	0.000349	0	0.000172
SD85_11	0	0.000148	7.12E-05	0.06437	0.429375	0.006733	0	0	0.554084	0.000279	0	0.00064
SD85_3	0	0	0	0.026354	0.491012	0.001877	0	0.000107	0.552408	0.000102	0	0.000285
SD85_5	0	0.000173	0	0.007508	0.014023	0.007331	0.000282	0	0.968999	0.000136	0.001066	0.000156
SD85_6	0	0	9.24E-06	0.083384	0.438297	0.002578	0.00149	0	0.527569	0.00095	0	0.000106
SD90_7	0	0.000279	3.64E-05	0.006462	0.511253	0.000969	0	0.000227	0.558675	0.00024	0	0
SD91_1	0	0	8.11E-05	0.065511	0.469326	0.001166	0.0004	0	0.52597	0	0	0
SD91_10	0	0	4.97E-05	0.010754	0.54276	0.000843	0	4.31E-05	0.527717	0.000386	0	0.0002
SD91_14	0	0.000105	0	0.048775	0.488839	0.001128	0.001682	0	0.52736	0.000194	0	0
SD91_2	0	0	4.78E-05	0.016402	0.514665	0.001649	0	1.03E-05	0.543208	0.000934	0	0.000357
SD91_3	0	0	0	0.104832	0.423739	0.001186	0.000418	0.000196	0.518734	0	0	0
SD9201_2	0	0	8.91E-06	0.218142	0.289898	0.004008	0.000337	0	0.495178	0.001786	0	0
SD9201_4	0	1.27E-05	0	0.182559	0.312984	0.003421	0.00041	6.47E-05	0.518757	0.000724	0	0
SD9201_5	0	0	0	0.180667	0.344981	0.004363	0.001342	0.000256	0.491189	0.000956	0	0.000404
SD9201_7	0	0.000253	0	0.188233	0.343774	0.003353	0.000779	0.000121	0.486365	0	0	0
SD9201_9	0	0	6.94E-05	0.206855	0.288501	0.003266	0	0.000107	0.510726	0.001342	0	0.000342
SD9202_1	0	0.000301	0	0.150866	0.351422	0.005724	0	0	0.520976	0.000308	0	0
SD9202_10	0	8.59E-05	9.25E-05	0.041182	0.027441	0.002441	0	0.000282	0.924769	0	0	0
SD9202_14	0	0	0	0.004469	0.003045	0.001838	0.000318	0.000221	0.987918	0.000485	0	0.000185
SD9202_15	0	0	0	0.162347	0.335122	0.006778	0.001394	2.16E-05	0.51939	5E-05	0	0.000287
SD9202_16	0	3.36E-05	1.75E-05	0.159882	0.366748	0.003201	0	0.000133	0.500222	0.000681	0	0.000126
SD9202_17	0	0.000128	0	0.168582	0.349232	0.004044	0	0	0.504703	0	0	0
SD9202_18	0	2.25E-05	0	0.190192	0.326245	0.003843	0.001147	0.000143	0.498129	0	0	0.000279
SD9202_19	0	0	8.43E-05	0.227149	0.268577	0.003971	0.001849	0.000193	0.502394	0.000422	0	5.39E-05
SD9202_2	0	0.000127	4.97E-05	0.171408	0.32499	0.003243	0	0.000161	0.522082	0.000411	0	0.000114
SD9202_3	0	0.0001	0	0.140532	0.36904	0.004663	0.000954	0.000192	0.517412	0.001047	0	8.48E-05
SD9202_6	0	0	0	0.232667	0.261995	0.005727	0.000927	0.000421	0.49813	0	0	0.005702
SD9202_7	0	0	0	0.166582	0.336838	0.005078	0	3.22E-05	0.516504	0	0	0.000314
SD9202_8	0	0	0	0.016782	0.009128	0.002424	0	0.000273	0.968832	0	0	0
SD9202_9	0	0	7.23E-05	0.034438	0.027802	0.00365	0.00165	4.89E-05	0.928061	0.000827	0	0.001118
SD93_16	0	0	0	0.112583	0.419166	0.002555	0.001066	0	0.511337	0.00023	0	0
SD93_3	0	0	7.95E-05	0.002114	0.004925	0.005282	0	0	0.986218	0	0	8.57E-05
SD93_5	0	3.47E-05	0	0.0868	0.420276	0.002967	4.47E-05	0.000118	0.540298	0.000499	0	0
SD93_9	0	0	2.98E-05	0.00069	0.001708	0.002012	0	8.6E-05	0.994371	0	0	0

All values reported in moles

Appendix C.1

Appendix C.2

Decision Tree for Carbonate Group Minerals Classification

Appendix C.3